Engineering Materials

Kapil Gupta *Editor*

Surface Engineering of Modern Materials

Springer

Engineering Materials

This series provides topical information on innovative, structural and functional materials and composites with applications in optical, electrical, mechanical, civil, aeronautical, medical, bio- and nano-engineering. The individual volumes are complete, comprehensive monographs covering the structure, properties, manufacturing process and applications of these materials. This multidisciplinary series is devoted to professionals, students and all those interested in the latest developments in the Materials Science field.

More information about this series at http://www.springer.com/series/4288

Kapil Gupta
Editor

Surface Engineering of Modern Materials

Springer

Editor
Kapil Gupta
Department of Mechanical and Industrial
Engineering Technology
University of Johannesburg, Doornfontein
Campus
Johannesburg, Gauteng, South Africa

ISSN 1612-1317 ISSN 1868-1212 (electronic)
Engineering Materials
ISBN 978-3-030-43231-7 ISBN 978-3-030-43232-4 (eBook)
https://doi.org/10.1007/978-3-030-43232-4

This Springer imprint is published by the registered company Springer Nature Switzerland AG
The registered company address is: Gewerbestrasse 11, 6330 Cham, Switzerland

Preface

Surface engineering and modification play a very important role in the performance of the parts and components made from various engineering materials. To obtain the desired properties and performance and to enhance service life, surfaces are required to be engineered using various processing and fabrication techniques. This book is focused on surface engineering of various modern materials such as novel composite, polymer, and hard and light metals, and study on roughness, wear, and subsurface properties such as micro-hardness and microstructure. It is aimed to provide fundamental knowledge, latest development, and research results. This book is intended to facilitate researchers, engineers, scholars, technical experts, and specialists working in the area of advanced manufacturing, materials, and surface engineering.

This book consists of seven chapters on various surface engineering and modification techniques for a wide range of modern engineering materials. Chapter "Friction Stir Processing: An Emerging Surface Engineering Technique" highlights special features of this technique which has been replacing other surface engineering methods rapidly. Chapter "Development and Surface Engineering of TiNi Shape Memory Alloy" presents the development of titanium-nickel alloy and engineering of its surface by wire EDM process. Chapter "Wear of Rubbers and Its Control in Conveyer Belt System" sheds light on an interesting study on surface wear of different types of rubber while use in conveyer belt for the mining industry. Chapter "Surface Characteristics When Solid State Welding of Aluminium Alloys to Magnesium Alloys" reports surface properties of Al-Mg weld made by various modern joining techniques. Chapter "Analytical Modelling for Laser Heating for Materials Processing and Surface Engineering" is followed by chapter "Surface Roughness and Morphology Studies on Machining Hybrid Composite Material Using Abrasive Water Jet Cutting Process". This book ends with chapter "Surface Engineering of Tungsten Carbide Tool Material by Nano and Microcrystalline Diamond Coatings" where the effect of coatings on the surface quality of tungsten carbide-type substrate material is reported.

I sincerely acknowledge Springer for this opportunity and their professional support. Finally, I would like to thank all the chapter contributors for their availability and valuable contributions.

Johannesburg, South Africa Kapil Gupta
January 2020

Contents

Friction Stir Processing: An Emerging Surface Engineering Technique

Padmakumar A. Bajakke, Sudhakar C. Jambagi, Vinayak R. Malik, and Anand S. Deshpande

Abstract Surface modification technologies impart improved surface properties without affecting the bulk properties of the material. The properties could be mechanical, electrical or thermal properties. Until recent past, thermal spray techniques, namely, plasma spraying, high-velocity oxy-fuel coatings and many others widely used for these applications. Friction stir processing (FSP) is a relatively newer technique that uses friction (between two surfaces) as a heat source to form a surface composite on the base alloy. This solid-state process not only refines the given structure but also disperses the reinforcements well within matrix alloy to enhance the surface properties. FSP was earlier employed to low melting point alloys such as aluminum and magnesium-base alloys, but now, with the recent development in tool geometry and tool materials, it can even be effectively used for high melting point alloys like steel and titanium-based alloys. Several process parameters seem to affect temperature and dispersion of reinforcements at the surface. They include rotational speed and traverse speed of the tool, number of passes, cooling medium and the tool geometry. Among these, rotation speed and traversing speed of tool seem to greatly affect the temperature distribution in the plasticized zone formed at the surface. This temperature, in turn, affects the grain refinement and dispersion of reinforcement particles. The present chapter summarizes the effect of these parameters. This chapter also reviews the latest developments in the tool material and its design. Further, their role in augmenting the base alloy properties is also discussed. High hardness, high fracture toughness, chemical inertness and high-temperature strength are few desirable properties of a tool to be used for FSP. In the end, the applicability of FSP as a surface modification technique has been assessed.

P. A. Bajakke · V. R. Malik (✉) · A. S. Deshpande
Department of Mechanical Engineering, KLS Gogte Institute of Technology, Belagavi, Karnataka, India
e-mail: vinayakmalik008@gmail.com; vrm@git.edu

S. C. Jambagi
Department of Mechanical Engineering, National Institute of Technology Karnataka Surathkal, Mangaluru, Karnataka, India

A. S. Deshpande
Visvesvaraya Technological University, Belagavi, Karnataka, India

K. Gupta (ed.), *Surface Engineering of Modern Materials*, Engineering Materials,
https://doi.org/10.1007/978-3-030-43232-4_1

Keywords Thermal spray coatings · Friction stir processing · Ceramics · Surface

1 Introduction

This section introduces the need for surface engineering that tailors the properties of surfaces intended for some specific applications. Various surface modification techniques and their broad classification are discussed. Surface engineering can be defined as "modifications of the surface and near-surface material properties in order to allow the modified surface to perform its intended function distinct from those expected from the bulk of the material" [1]. The general idea behind engineer or modify a surface is to compliment the surface of a component with superior properties that require for various purposes and may not be present in base material. For example, in machining, to alleviate tool wear problems, surface modification in the form of thin coating of various substrates such as aluminium oxide, titanium nitride is deposited using chemical vapor deposition processes. The hard coating layer provides wear resistance and improves fracture toughness. The technological value addition justifies the increase in cost [2, 3].

Surface modification can be categorized into following three categories [2, 3]:

(a) A technique without altering the chemical composition of the base material, i.e., by changing metallurgy or surface texture.
(b) A technology that changes surface chemistry, wherein a known element is diffused in the surface layers of the parent body.
(c) A technology wherein a new material deposited onto the surface as a coating. In these processes, the material is added to the substrate in layers.

Sometimes the coatings were subjected to post-processing as well in order to homogenize and densify them. For example, a thermally sprayed alumina coating on a metallic substrate can be re-melted using a laser beam [4].

A surface without chemical changes in the base material can be obtained through the thermal process, wherein heat sources of flame, induction heating, laser or electron beam is used to the desired phase transformation at the surface. For example, martensitic transformation in high carbon steel. It is possible to obtain the required change at the surface by mechanical means. In other words, cold working processes, such as shot peening, grit blasting, explosive hardening, etc. enable to increase surface hardness through work hardening mechanism and they can even increase the fatigue life of the components [2, 3].

The processes where surface modification of the component is allowed by altering the surface chemistry include thermochemical diffusion process, Electrochemical and ion implantation processes. In these processes, either atoms or ions are made to impinge on the reactive surfaces forming a layer of desired properties. Surface modification can be achieved by depositing a new material onto the surface (coating or cladding). Figure 1 shows the broad classification of surface modification techniques falling under this category. In such processes, the base material is coated with another layer with a complementary property.

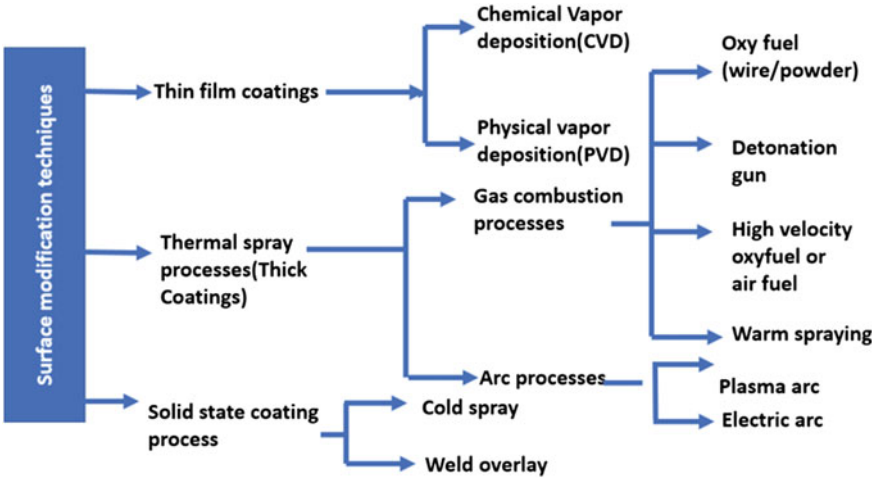

Fig. 1 Broad classification of surface modification techniques [5]

Depending upon the applications, the coating thickness can vary from few micrometres (thin film) to an order of hundreds of a micrometer, even as high as a millimeter-thick coating are also possible. Thin-film coatings can be achieved using chemical vapour deposition (CVD) and physical vapour deposition (PVD) techniques. In CVD, metal chlorides, fluorides, bromides, iodides etc. are made to react with gases, decompose and deposit the coatings in the form of gas or vapour, on to the substrate in a vacuum chamber. The temperature and pressure are respectively maintained ~800–1100 °C and 13–100 kPa. Even plasma can be used for the decomposition process. In that case, the process could be known as either Plasma-assisted (PACVD) or plasma-enhanced (PECVD) process. Typically, coatings below 50 μm are achieved using this process. With this process, metals, alloys, intermetallic, boron, silicates carbides, oxides and sulfides can also be deposited [6]. The PVD process comprises of three steps: Evaporation, sputtering and ion plating. It is known for its lower deposition rate (coating thickness < 1 μm) and is carried out in a lower pressure ~1.3×10^{-6} to 13 Pa. During evaporation, the vapours of any solid materials are formed by heating and then condensing onto a substrate material. This may yield lower adhesion strength as the vapour particles possess lower kinetic energy. In sputtering, the same process is carried out at pressures between 0.13 and 13 Pa. In this way, the particles gain more kinetic energy and hence enable them to form dense and more adherent coating [6]. During ion plating process, the nascent surface of substrate surface is formed by Argon ion bombardment, while the coating material is evaporated by plasma and deposited on to the substrate. The bombardment of ions takes place in cold chamber at a pressure of 1 Pa. This process catalyzes the nucle-

ation and forms a coating of high adhesion strength. The coating thickness typically lies below 5 μm [5, 6].

2 Thermal Spray Processes

It is a material processing technology of the generic category that generally uses powdered consumables. Sometimes consumable in wire form is also used. The consumables are melted using a heat source. A high-velocity impinging jet is used to carry these particles or molten droplets produced from the tip of the consumable rod onto the substrate to form a coating of desired thickness.

The coating is constituted by deformed individual particles known as a splat. The splat could be either fingered or disc-shaped, depending on the preheating conditions. The higher preheating temperature of the order of 200 °C yields disc-shaped splat, which is desirable for better splat as well as better coatings. Thermal spray process is an effective method of applying thick coating for variety of applications like boiler components, automotive systems, chemical process equipment, power generation equipment, pulp and paper processing equipment, aircraft engines, bridges, rollers and electric arc furnace (EAF) electrodes in steel mills, orthopedics and dental prostheses, concrete reinforcements, land-based and marine turbines, ships, etc. A general working principle of this process is shown in Fig. 2.

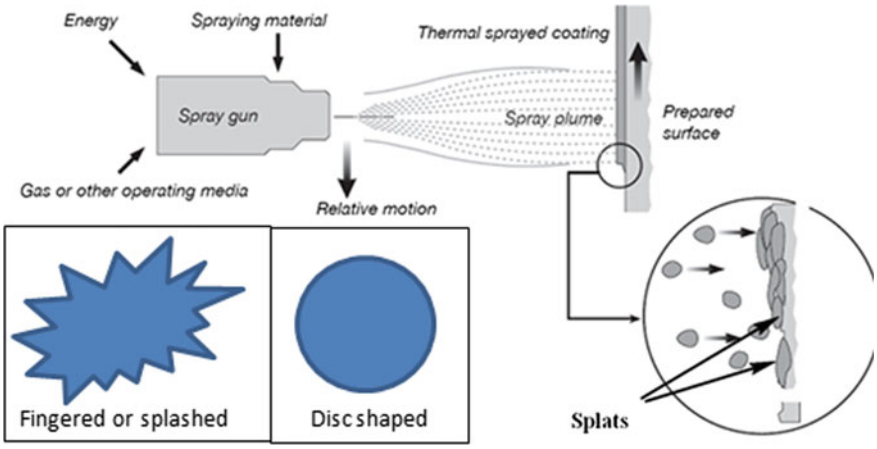

Fig. 2 Principle of thermal spray process [2, 3, 7]

2.1 Classification of Thermal Spray

The gas combustion process typically includes the following processes to name a few:

(a) Oxy-fuel (Wire or powder).
(b) Detonation gun.
(c) High-velocity oxy-fuel or high-velocity air fuel.
(d) Warm spraying.
(a) **Oxy-Fuel (Wire or Powder) Method**

The schematic arrangement for oxy-fuel process shown in Fig. 3, consist of the following units:

i. Spraying gun.
ii. Wire feeding arrangement.
iii. Oxygen and acetylene gas cylinders.
iv. Air compressor.

An oxygen and acetylene mixture taken in a proportionate measure is released inside the combustion chamber of the gun. The flame flares through the nozzle of the gun when the mixture is ignited. The powder melts into droplets and is carried through a compressed air jet from the gun onto the substrate, kept at a specified distance [8].

Advantages:

- Low capital cost.
- Consumable in wire form is cheaper than powder.
- High deposition efficiency.
- Portable equipment.
- Possible to use this system in areas without electricity supply.

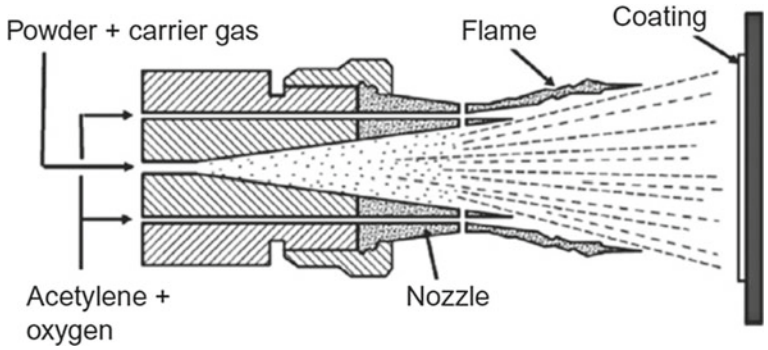

Fig. 3 Flame spraying with a powder [9]

Limitations:

- Limited to spraying materials supplied in wire or rod form.
- Production rate, density, adhesion strength and oxide content are lower as compared to HVOF or plasma spraying.

Flame Spraying with Powder (FS-Powder)

The working principle of this process is similar to that of the flames spray (powder) process. However, in this case powder feedstock in the form of wire is fed into the flame through a roller mechanism that rotates at a controlled speed into the combustion flame.

Advantage: A wide range of metallic and ceramic material is available in powder form

Limitation: Production rate, density and adhesion strength lower as compared to HVOF or plasma spraying [2, 3].

(b) **Detonation Gun Spray Method**

The schematic arrangement of the Detonation gun or D gun process is shown in Fig. 4. In this method the gun is preloaded with consumables in powder form using small gas pressure. For combustion, a proportionate mixture of oxygen and acetylene is used. The mixture is ignited using spark plugs and an instant explosion occurs producing a temperature of around 3200 °C, which is sufficient to melt most of the materials available. After detonation the hot particles are accelerated towards the target with high velocity. This is a very important factor for having a dense coating and good bond strength. The nitrogen gas is used for flushing the combustible products at the end of every cycle. Since the process produces loud noise, the installation is kept inside a soundproof room. It is also required in this case to install an elaborate arrangement for fuel and purge gas control, powder feeding, gun cooling and spark plug operation [10].

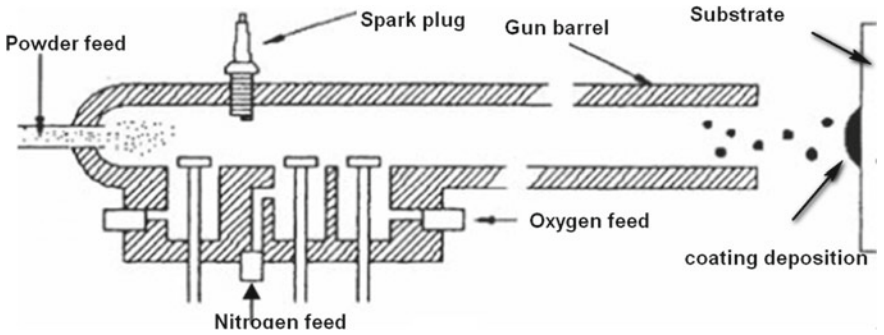

Fig. 4 Schematic of the D-gun™ process [8]

Advantages [10]:

- It can deposit metals, alloys, and ceramics.
- Produces dense coating with good bond strength.

Limitations [10]:

- The process involves a very elaborate arrangement.
- The process makes a loud noise.

(c) **High-Velocity Oxy-Fuel Spraying (HVOF)**

In the schematic arrangement shown in Fig. 5, a mixture of oxygen and fuel (kerosene, acetylene, propylene or hydrogen) is introduced in the combustion chamber of the gun. When ignited, the burnt gas attains a very high temperature and pressure. This gas expands and escapes through its small confinement with high velocity. The carrier gas is used to supply the powder at the center of the flame. The melted particles are deposited onto the substrate at a very high velocity by the hot gas through the nozzle [11].

Advantages [10]:

- Better adhesion between substrate and coating.
- Dense coating.

Limitations [10]:

- Fuel gas consumption is more.
- It is still not popular for ceramics.
- The process involves the generation of high pressure and therefore adequate safety measures are required for the safe operation of the unit.

Another variant of this process is the High velocity of the air-fuel (HVAF) process, which is similar to the HVOF process wherein the required combustion is achieved with compressed air, gaining popularity these days owing to its higher deposition efficiency and oxidation resistance.

(d) **Warm Spraying**

This is a modification of the HVOF process where nitrogen is introduced to control the temperature and particle velocity between 800–1900 K and 900–1600 m/s, respectively. The schematic of the process is shown in Fig. 6. This process is partic-

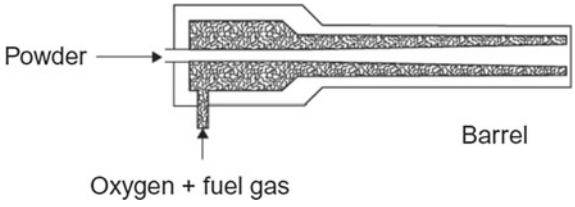

Fig. 5 Schematic diagram of the HVOF process [9]

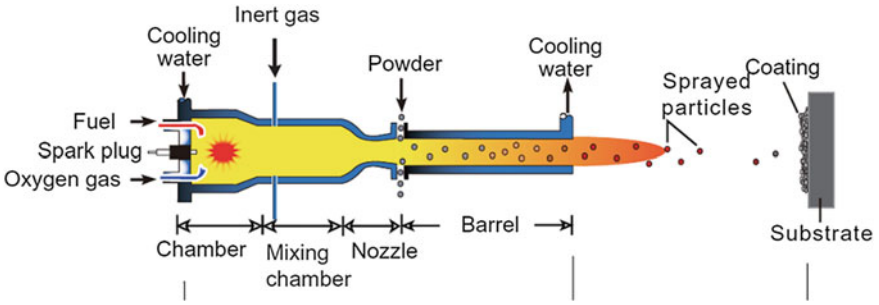

Fig. 6 Schematic of Warm spray process [12]

ularly suitable for highly oxidation prone materials like titanium. With addition of a suitable amount of nitrogen both the particle velocity and temperature are controlled so that the particles melt but do not oxidize substantially. Thus, this process is an attempt to combine the advantages of cold spray and HVOF [12].

Advantages [12]:

- Undesirable processes like oxidation or decarburization are minimised.
- High coating density.

Limitations [12]:

- The hot gas used in warm spraying is not as clean as cold gas processes. It contains water vapour, unreacted hydrocarbon and oxygen.

In addition to these processes, there few thermal spray processes which use an electric arc to melt the powder feedstock especially meant for high melting point materials.

Electric Arc Processes

Figure 7 shows the schematic diagram for the electric arc wire spray method. In this process, an electric arc is set up between the tips of two conducting wires rolled out from wire feeders. The heat generated melts the tips of the wires. The molten droplets are then directed towards the target through a compressed air jet. Electric power is supplied by a welding power supply [10].

Advantages [10]:

- High deposition rate.
- Simple and low-cost equipment.

Limitations [10]:

- Only electrically conducting materials can be sprayed.

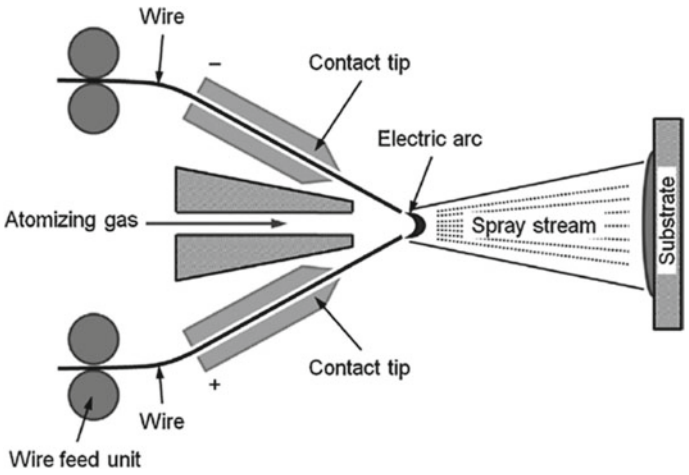

Fig. 7 Schematic diagram of the electric arc wire spray process [13]

Plasma Spraying

Plasma spraying is a very versatile thermal spraying process. Figure 8 shows the schematic arrangement of the plasma spraying method. An arc is struck between tungsten tipped copper cathode and an annular copper anode. Both the electrodes are water-cooled as it is necessary to protect the plasmatron/gun (i.e., the plasma generator) from excessive heating. Plasma gas, which is introduced through the annular space between the electrodes undergoes ionization in the high temperature environment producing plasma. The ionization is accomplished by collisions of electrons of the arc with the neutral molecules of the gas. The plasma spreads out of the electrode encasement in the form of a flame. The consumable in powdered form is fed into the flame in measured quantity. The powders melt immediately, gaining momentum from the expanding gas and rush towards the substrate to form a thin deposited layer [8, 10, 14–16]. It is also possible to use consumable in the form of wire. The temperature in the plasma arc can be as high as 10,000 °C, and it is capable of melting possibly all materials. Plasma spraying can be conducted either in atmosphere or in a chamber filled with an inert gas like argon in low pressure. The processes are known as atmospheric plasma spraying (APS) or low-pressure plasma spraying (LPPS).

2.2 Advantages and Disadvantages of the Thermal Spray Process

Advantages

- It is a versatile technique employed to cater the needs of various industrial applications [17].

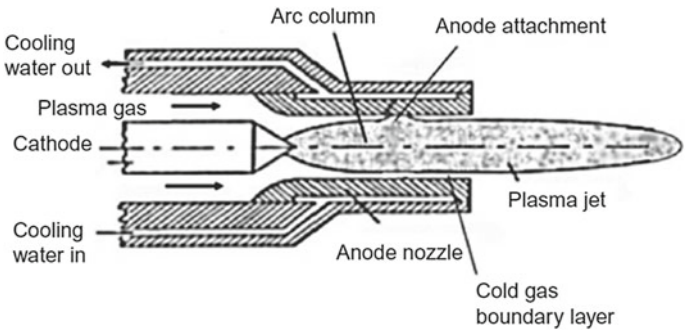

Fig. 8 Schematic of Plasma spray process [9]

- Economical, improved coating properties and hence improved life of a component [17].

Disadvantages

Thermal spray processing, however, suffers from several microstructural deficiencies as explained below:

- During coating deposition, inhomogeneities like fully or partially melted particles along with porosities result in a lack of cohesiveness of the coating. These anomalies further exacerbate the coating properties like corrosion and wear [5].
- During the deposition of metals, owing to high temperature, the powder particles tend to undergo severe oxidation. This entrapped oxide layer between the layers of the coating can lower the cohesion strength of the coatings that could even deteriorate the properties of the coatings like toughness, strength and machinability [5].
- During thermal spray, the coatings tend to fail by forming tensile cracks under the action of mechanical load. These cracks set up during cooling and solidification of the coatings. However, the substrates develop compressive stresses at their surface. These residual stresses have to be controlled by proper pre and post-heating conditions [5].

Surface modification technologies impart improved surface properties without affecting the bulk properties of the material. The properties could be mechanical, electrical or thermal properties. So far, thermal spray techniques, namely, plasma spraying, high-velocity oxy-fuel coatings and many others were widely used for these applications. Friction stir processing (FSP) is a relatively newer technique that uses friction as a heat source to form a surface composite on the base alloy. This solid-state process not only refines the given structure but also disperses the reinforcements well within matrix alloy to enhance the surface properties. FSP was earlier employed to low melting point alloys such as aluminum and magnesium-base alloys, but now, with the recent development in tool geometry and tool materials, it can even be effectively used for high melting point alloys like steel and titanium-based alloys.

3 Solid-State Coating Process

Until now, the coatings were produced either by fully melting or by partially melting with intense heat. This heat, at times, exacerbate the coating properties, i.e., it may give rise to the phase transformation that may entail into the formation of detrimental phases in the coatings for example, in medical prosthesis made of hydroxyapatite, Plasma spray is not preferred due to the drastic phase changes that cause slump in biocompatibility and strength of the coatings. Hence, there is another class of coating process emerging called the solid-state coatings, wherein the coatings are obtained utilizing minimal amount of heat derived by rubbing action between the two mechanical components or by plastic deformation of the powder particles when fed in a supersonic speed. In either of these cases, oxide free, dense coatings are ensured. Though there are few other solid-state coating processes (like cold spray and weld overlay), the discussion is restricted to FSP in this chapter.

3.1 Friction Stir Process

The Friction Stir Process (FSP) primarily evolved from friction stir welding (FSW) [18]. FSW is used for joining plates and sheets whereas FSP is carried on monolithic plates with the principal objective of refining the microstructure. A schematic depiction of the FSP on monolithic plates is shown in Fig. 9. Both processes work on the same principle. The substrate material is worked under thermomechanical conditions by a specially designed tool consisting of a pin and shoulder. The rotating tool with desired axial force is plunged into the substrate so that a full-length pin and surface of the shoulder are interacting. This encounters large frictional heat at the tool-substrate interface and material undergoes intense plastic deformation. As the tool traverses forward visco-plastic material flows around the pin and gets forged in the stir zone due to the backward tilt of the tool. The temperatures reported during the process are nearly 0.5–0.9 of melting temperature (T_m) and no traces of melting are observed. Hence it is termed as a solid-state process [19, 20].

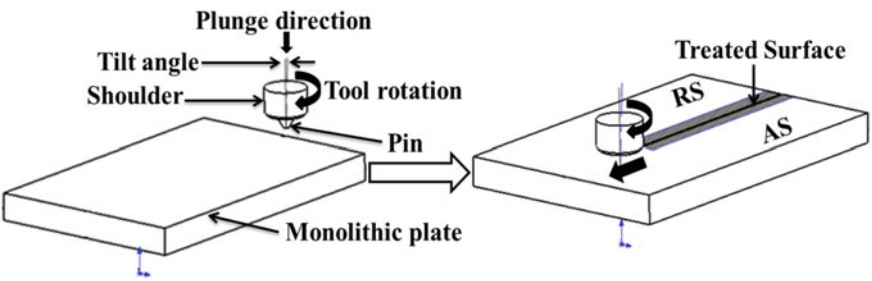

Fig. 9 Pictorial view of FSP [AS: Advancing Side, RS: Retreating Side]

Mishra et al. were the pioneers to process aluminum alloys via FSP and reported superplastic behavior of the processed material [18]. However, the authors find a sufficient amount of work carried on a variety of materials like aluminum, magnesium, copper, iron and titanium and their alloys [21]. Since the temperatures prevailing during the process are above recrystallization, hard to deform materials (possessing hexagonal closed pack structure) and alloys with relatively poor ductility can be processed [22]. The process has proved to be an effective tool for grain refinement, microstructure homogenization, surface/bulk composite and crack repair. Over the period, different variants of the process have emerged and few of them will be deliberated under Sect. 3.1.1.

3.1.1 Methods of FSP

FSP methods important from surface engineering perspective are discussed in this section. A schematic showing different variants is depicted in Fig. 10.

Manufacturing industries are emphasizing on surface engineering to obtain selective functionalization of surfaces and advanced component design. This phenomenon includes tailoring of structural and chemical properties of the substrate by coating the surface with a thin layer aimed for corrosion and wear resistance. Liquid state surface treatments encounter severe defects like inadequate solidification, porosity and cracks. However, Friction stir surfacing and cladding are an improved version of FSP, which overcome the aforementioned drawbacks. These processing techniques use a consumable tool as a depositing material. Thermally sensitive materials can also be processed due to its ease of material transfer from a consumable tool to the surface with better bonding and partial dilution [23]. A hybrid method is also found in the literature. The surface coating (compositional modification) is done by conventional surface engineering techniques and microstructural modification via FSP.

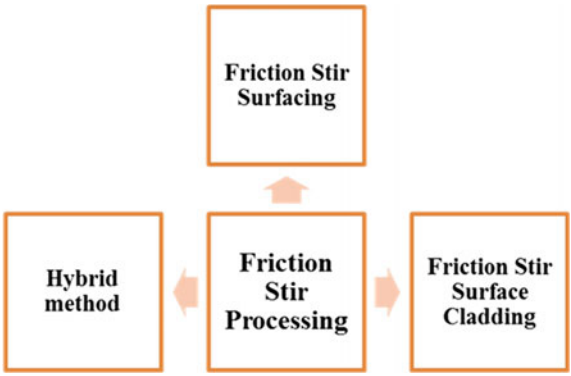

Fig. 10 Friction stir based processing variants in the context of surface engineering

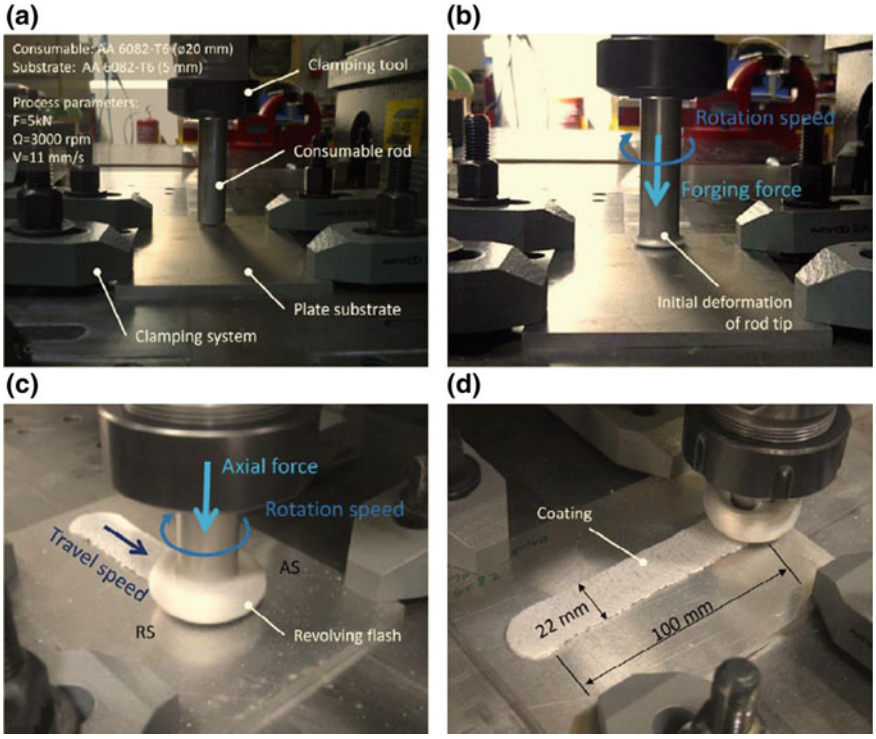

Fig. 11 Friction stir surfacing demonstrating plasticization phase and deposition phase **a** experimental setup and substrate-consumable rod contact, **b** initial deformation of rod tip, **c** viscoplastic material deposition on the substrate and **d** coating [24]

Friction Stir Surfacing

Friction stir surfacing (FSS) is a solid-state surface engineering technique that effectively deposits similar or dissimilar material on the desired substrate to produce coating in critical applications. During the process, a rotating consumable tool is rubbed against the substrate under axial force. Under high axial force, torque and temperature, the process takes place in two phases termed as plasticization phase and deposition phase. The rotating consumable tool is pressed against the substrate (Fig. 11a) and frictional heat encountered causes material softening at the tool-substrate interface. This is the reason for initial deformation and viscoplastic material at the tooltip (Fig. 11b). Further, as the tool is traversed on the substrate, the viscoplastic material gets deposited (Fig. 11c). An interdiffusion process contributes to achieving better metallic bonding between the substrate and the viscoplastic layer (Fig. 11d). The latest attempted work in FSS is critically reviewed below.

Aluminum alloy 6061 was coated on the surface of carbon steel Q235 by FSS. The crux of the process lies in Continuous Dynamic Recrystallization (CDRX) which resulted in highly refined, equiaxed grains and uniform distribution of precipitates.

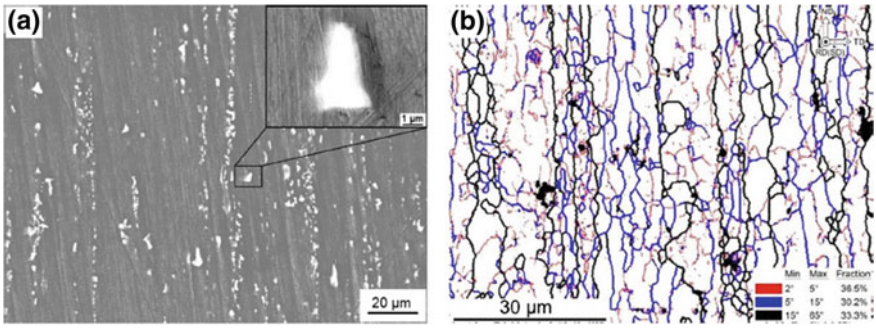

Fig. 12 SEM of AA6061 consumable tool showing distribution of precipitates at the grain boundaries (**a**) and elongated grains (**b**) [25]

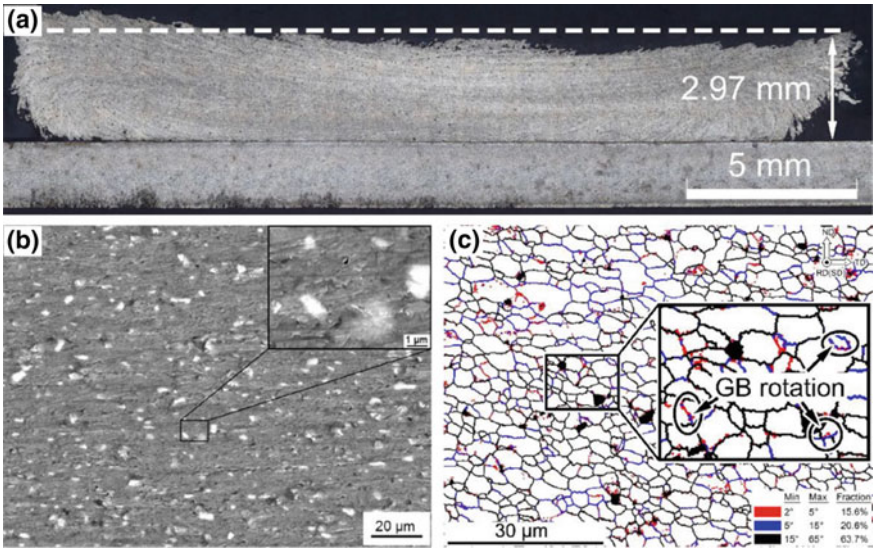

Fig. 13 **a** AA6061 coated to an average thickness of 2.97 mm on carbon steel Q235 surface, **b** SEM of coated surface depicting the uniform distribution of precipitates and **c** EBSD analysis showing highly refined and equiaxed grains [25]

The consumable tool AA6061 was fabricated by extrusion followed by precipitation hardening. Scanning electron microscopy (SEM) depicts the precipitates aligned along the grain boundaries (Fig. 12a). Further, elongated grains were also observed with 66.7% of low angle grain boundaries (Fig. 12b). The coating of material on substrate (Fig. 13a) enabled homogeneous distribution of precipitates along with reduced size of precipitates; this was attributed to higher deformation involved during the process (Fig. 13b). In addition to this, electron backscatter diffraction (EBSD) analysis shown in Fig. 13c revealed that the coated surface grains were extremely

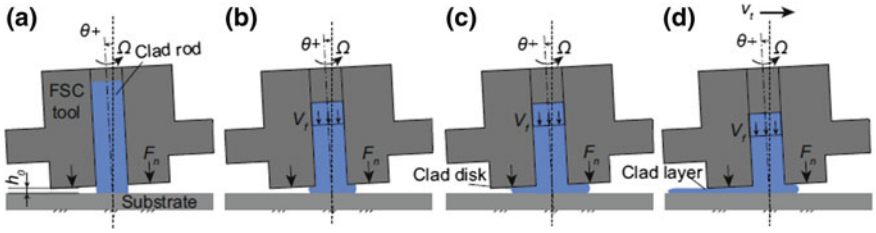

Fig. 14 Pictorial representation of FSSC: **a** located at height h_o with normal force F_n and tool rotating at rotation rate of Ω, **b** consumable clad rod being extruded out with a volumetric flow rate of V_f [mm^3/s], **c** frictional preheating and deformation of clad material and **d** cladding phase: the rotating tool is traversed along the substrate at traverse speed V_t. The backward tool tilt θ° is provided to forge back the viscoplastic clad material on the substrate [26]

refined and equiaxed due to CDRX. The grain boundary rotation was attributed to higher strain rates and the CDRX, which resulted in a decline of low angle grain boundaries to 36.2% [25].

Friction Stir Surface Cladding

Friction stir surface cladding (FSSC) is one of the variants of FSP, developed to use as an alternative technique to conventional cladding processes. Thermo-mechanical conditions involved in the process disrupt the oxide layer and helps in forming the metallic bond between the substrate and the cladding material. A special-purpose hollow tool is designed to extrude the consumable clad material. The tool and substrate interaction exists in two versions, (i) the tool is lowered to touch the substrate material at a constant axial tool force and (ii) the tool is positioned at required height without touching the substrate material (Fig. 14a–d).

Van der Stelt et al. were the pioneers to develop FSSC, a novel cladding process which is similar to FSS. The advantage of FSSC over FSS is that the cladding material is deposited in a controlled manner. In one of his experiments, AA2024–T351 was cladded with relatively softer AA1050 material. Two sets of trials were carried out with changing axial tool force of 4 and 15 kN to understand the effect on cladding and mixing, respectively. With lower axial tool force of 4 kN, the cladding material established a good metallurgical bonding with the substrate. However, along with good metallurgical bonding even the cladding material was mixed with the surface region of substrate at higher axial tool force of 15 kN. The hardness distribution was found to be better for the case of the surface with mixed regions [27]. The authors envisage that FSSC can be an effective technique for cladding as well as mixing the clad material with the substrate to form beneficial secondary phases. This may contribute to the enhanced properties.

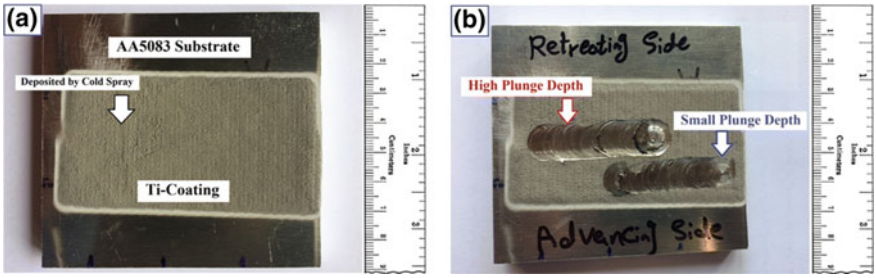

Fig. 15 Illustrating the hybrid method **a** AA5083 substrate coated with pure titanium via cold-spray and **b** FSP used as post modification technique on the cold-sprayed titanium layer [28]

Hybrid Method (Surface Engineering and FSP)

In the present context, a hybrid method refers to the use of FSP as a secondary process followed by a usual surface treatment technique. Surface metal matrix composites can be obtained by coating/deposition techniques. Further, enhanced properties can be attained by grain refinement of the coated surface and elimination of undesirable microstructural features. In this regard, FSP has the potential to modify the microstructure and help in grain refinement. Figure 15 represents the hybrid method.

FSP successfully modified the structural integrity and reduced porosity in the cold sprayed layer. Pure titanium was deposited to a thickness of 800–850 μm on AA5083 substrate via cold spray technique (Fig. 15). The calculated porosity in the coated structure was ~30% and grain size was <25 μm. Here the effect of plunge depth (0.3 mm and 0.5 mm) during FSP was demonstrated. Complete densification was achieved with increased plunge depth of 0.5 mm along with effective grain refinement (<1 μm). The higher plunge depth helped in severe plastic deformation, effective forging of material and thermal exposure resulting substantial densification and grain refinement by capping the pores [28].

Generally, thermal spray coatings are used in practice to address erosion problems, which are encounter in fluid machinery parts. The performance level of the coated surface deteriorates due to the presence of elemental segregation, splat boundaries and non-homogeneous microstructure. Rani et al. [29] demonstrated that FSP is a promising post-processing path in eliminating the inherent non-homogeneities associated with thermal spray coatings. Mane and Hosmani [30] attempted to enhance the surface hardness of Al 6061 alloy with a combined approach of thermal spray, friction stir surface processing (FSSP) followed by heat treatment. A slit groove (width 3, 5, and depth 1 mm) was cut on the substrate and filled with copper powder (average particle size 65 μm) by thermal-spray technique. The hardness of the base material without surface alloying with Cu and after aging was $115HV_{0.1}$. Whereas, maximum hardness was reported in the case of the substrate surface alloyed with Cu and aged was $156HV_{0.1}$. The increased hardness was attributed to the formation of Al_2Cu precipitates due to FSSP and age hardening. X-ray diffraction (Fig. 16) revealed the presence of Al_2Cu phases in Al6061 surface alloyed with Cu via FSSP followed by

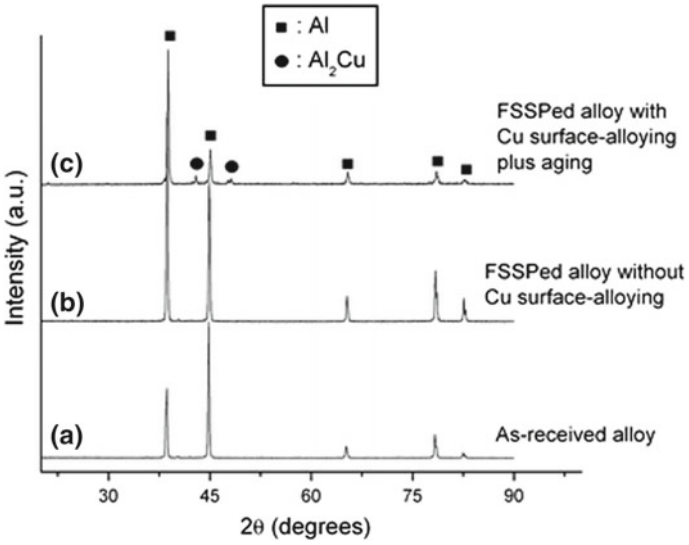

Fig. 16 X-ray diffraction pattern recorded from the surface of **a** as-received Al 6061 alloy, **b** stir zone of the FSSPed sample without Cu surface-alloying and **c** FSSPed alloy with Cu surface alloying followed by aging [30]

aging (Fig. 16c). However, only aluminum peaks were recorded in FSSPed alloy without Cu surface-alloying (Fig. 16b) and as-received alloy (Fig. 16a). Here the authors infer that conditions in thermal-spraying didn't favor the formation of Al_2Cu phases, but FSP assisted in the formation of in-situ Al_2Cu phases as well as its uniform distribution.

3.1.2 Alloys Coated Using FSP

The surface engineering approach finds application in the reduction of wear and corrosion properties. Some of the applications include repair of critical parts at nuclear power plants wherein the failure is triggered by stress corrosion cracking and retrieval of worn railway trails. Generally, thermal spray coatings are done at elevated temperature and there exists a high possibility of formation of undesired brittle phases. These brittle phases produce sharp interfaces that nucleate to cause failure of the material. It is also associated with other inherent non-homogeneities like porosity, splat boundaries, elemental segregation, and non-uniform microstructure. Further, coating of hybrid powders is a challenge due to agglomeration and deteriorates the material properties by non-homogeneous microstructure. Therefore, to overcome all these problems coating of any material is preferred to be achieved without melting. Hence, FSP and its variants are the favourable prominent methods to produce coating on variety of substrates with better metallurgical bonding and minimal dilution. The problems associated with thermal spray coating are eliminated by FSP and is mainly

attributed to its solid-state processing nature with its capability to impart large strains and strain rates.

Coating of non-ferrous materials encounter some problems due to their high temperature instability and high thermal conductivity. Rao et al. [31] conducted a feasibility study to develop friction surfacing coatings of low carbon steel, copper, aluminum alloy AA6063 and Commercially Pure (CP) titanium on non-ferrous alloy substrates like CP aluminum, CP copper, Inconel 800, magnesium alloy ZM21 and titanium alloy Ti–6Al–4V respectively. Table 1 represents detailed summary of reported work on various substrates and consumable rod combinations used.

Table 1 A Summary of coating feasibility with respect to different non-ferrous substrates and consumable rod combinations

Substrates	Consumable rods			
	Low carbon steel	Copper	Aluminum alloy AA6063	CP Titanium
CP Aluminium	The deposition was not possible The hard steel rod caused the drilling effect	The deposition was not possible The heat generated was not adequate to deform copper	The deposition was possible The contact interface enabled enough heat	The deposition was not possible as both the materials were softer
CP Copper	The deposition was possible Heat concentration on the steel side was attributed to higher thermal conductivity of copper	Intermittent deposition Insufficient heat at the contact surfaces	Very thin deposition Limited heat concentration at the interface	The deposition was not possible Huge difference in material deformation characteristics
Inconel 800	The deposition was possible Materials have comparable mechanical and thermal properties	The deposition was not possible At elevated temperature, copper softened very fast due to its high ductility	The deposition was not possible Aluminum softened due to its higher thermal conductivity	Discontinuous deposition Titanium found to be highly unstable at elevated temperatures
Magnesium alloy ZM21	The deposition was not possible Steel rod ploughed through the substrate	The deposition was not possible Developed friction was sufficient to cause heat	The deposition was not possible Large difference in material deformation behaviour	The deposition was not possible Titanium rod slips over Magnesium substrate
Titanium alloy Ti–6Al–4V	The deposition was not possible Friction insufficiency and oxide formation	The deposition was not possible Friction insufficiency and oxide formation	Very thin deposition Faster softening resulted in flash instead of coating	Intermittent deposition Instability of Titanium at elevated temperature

Among ferrous materials, stainless steel has been at the forefront as a coating material due to its corrosion resistance. Nixon et al. attempted to coat stainless steel AISI316 on mild steel and medium-carbon steel EN24, respectively, by friction surfacing. For stainless steel AISI316 over mild steel, bond strength of the coating was reported to be at a maximum of 502 MPa tested under ram tensile test. The coated surface was investigated for corrosion resistance and was found to be better than the substrate [32]. On the other hand, medium-carbon steel EN24 coated with stainless steel AISI316 exhibited fine-grain martensitic microstructure without the presence of carbide particles. This confirmed the presence of good bonding interface between the coating and the substrate [33].

3.1.3 Reinforcements Used with FSP

FSP has the flexibility to embed reinforcement particles either ex-situ or to generate it in-situ to modify the surface/bulk texture of the substrate. In the ex-situ approach, the reinforcement particles are prepared externally and added, which do not form secondary intermetallic phases during the process. Such reinforcement particles include ceramics (SiC, TiC, B_4C, WC, ZrC, BN, TiN, TiB_2, TiO_2, Al_2O_3, ZrO_2 and SiO_2) and well-known forms of Carbon like: Fullerene, Graphene, Carbon Nano Tubes (CNTs), Single-Walled Carbon Nano Tubes (SWCNTs) and Multi-Walled Carbon Nano Tubes (MWCNTs). In the in-situ approach, the reinforcement particles are free to react with the substrate material to form secondary intermetallic phases, which are thermodynamically more stable. Here the reinforcement particles may be pure metallic material (Cu, Al, Ti, Ni and Fe) and reaction with the substrate material yields intermetallic phases. For example, FSP of Al/Cu (substrate/reinforcement) results in the formation of Al_2Cu intermetallic phases. Further, hybrid type of reinforcement is also attempted. The hybrid reinforcement may be a combination of ceramic–ceramic (SiO_2–Al_2O_3, Al_2O_3–TiO_2, TiC–B_4C, TiB_2–Al_2O_3), pure metal-pure metal (Ni–Ti: shape memory alloy), ceramic-transition metal dichalcogenide (SiC–MoS_2) and ceramic-non-metal (SiC–Graphite, αAl_2O_3–Graphite) and so on. Various combinations of the reinforcements and the base materials attempted are discussed in Table 2. The basic FSP involves pre-placing of reinforcement particles into grooves or holes on the substrate surface. Whereas, variants of FSP involve feeding of reinforcement in the form of consumable rod (as discussed in the section "Friction Stir Surfacing"), consumable rod/powder feedstock passed through non-consumable hollow cylindrical tool (as deliberated in the section "Friction Stir Surface Cladding"). The reinforcement material is also coated/deposited via surface engineering techniques and FSP is used as a post-processing method (as highlighted in section "Hybrid Method (Surface Engineering and FSP)").

Table 2 Tabulation for largely experimented reinforcement-base material combinations with their reported outcomes

Reinforcement type	Most experimented	Base materials attempted	Remarks
Ceramics	SiC	Aluminum alloys (5052) Magnesium alloys (AZ91) CP-copper Iron alloys (Stainless steel 316L) CP-titanium	• Self-hardness of SiC (2480 HK) made it to selected as an effective reinforcement material among the ceramics family • Reinforcing AA5052 surface with SiC impedes direct load transfer of aluminum surface with disk and sustain wear load. The increased hardness of the reinforced region has a positive effect in reducing wear behaviour [34] • Incorporation of nano-sized SiC in magnesium alloy AZ91 enhanced strength and elongation Higher-strength was attributed to smaller grain size and increased elongation was ascribed to lower particle cluster size [35] • Among the copper substrate embedded with micro and nano-sized SiC, the higher hardness and superior wear resistance were observed for the combination of Cu/nano-SiC [36] • Higher rotational speed 1000 rpm and lower traverse speed 14 mm/min assisted in superior properties of Stainless Steel 316L/SiC surface [37] • Addition of nano-sized β-SiC into CP-titanium transferred the prior β-Ti grains into α′-Ti martensite sub-structure, which reflected dynamically restored microstructure at the processed region [38]

(continued)

Table 2 (continued)

Reinforcement type	Most experimented	Base materials attempted	Remarks
	Al_2O_3	Aluminum alloys (6061) Magnesium alloys (AZ91) CP-copper Iron alloys (Mild Steel) CP-titanium	• The strong ionic interatomic bonding being an inherent property of Al_2O_3 is responsible for its desirable material properties. Has a self-hardness of 2100 HK • With single FS pass, nano-Al_2O_3 was successfully embedded into AA6061 surface. The enhanced material properties due to effective mixing, material flow and refined microstructure were ascribed to the use of taper threaded cylindrical tool with concave shoulders [39] • The poor formability and ductility of AZ91 are due to the presence of precipitation of brittle $Mg_{17}Al_{12}$ β-phase. After FS, lower fraction and disappearance of β-phase was found in thermo-mechanical affected zone and stir zone, respectively [35] • Increased vol% of Al_2O_3 in the copper matrix extended the recrystallization temperature by pinning grain boundaries of the copper substrate and hindering the movement of dislocations [40] • Four FS passes drastically reduced the grain size of mild steel from ~15 to 2 μm and was mainly ascribed to uniformly dispersed nanoparticles and dynamic recrystallization [41] • Among 80 and 20 nm Al_2O_3, better mechanical properties were reported for 20 nm particles and corresponding 3.9–5.7 volume fraction particles [42]
Forms of carbon	CNTs	Aluminum alloys (1016) Magnesium alloys (AZ31) T2-copper	• High elastic modulus of CNTs as high as 1 TPa and tensile strength as high as 50 GPa is due to the presence of strong sp2 bonding between C–C bonds • MWCNT reinforced in AA1016 substrate exhibited a strong interface and acted as the load-bearing element [43] • The combination of AZ31B/CNT demonstrated the highest hardness value of 69 HV for 2 wt% of CNT and 3 FS passes [44] • The reinforcement of CNT in T2–copper matrix revealed a negligible reduction in conductivity compared to parent substrate [45]
Pure metals	Copper	Aluminum alloys (1050)	• In-situ intermetallic phases possess high specific modulus, high specific strength and excellent wear properties at both ambient and elevated temperatures • AA1050–H24 was reinforced with pure Copper powder of 5 μm. The tool rotation speed of 750 rpm and traverse speed of 0.83 mm/s led to the formation of Al_2Cu intermetallic phases and distribution at the nano-level [46]

(continued)

Table 2 (continued)

Reinforcement type	Most experimented	Base materials attempted	Remarks
	Aluminum	CP-magnesium Titanium alloys (Ti–6Al–4V)	• Pure magnesium reinforced with Aluminium powder formed $Mg_{17}Al_{12}$ intermetallic phases during FSP. The crystalline size of intermetallic reached $\leq$50 nm and was attributed to severe plastic deformation and high material flow during the process [47] • Pure Aluminium powder was embedded in Ti–6Al–4V alloy. The reaction kinetics during the FSP formed Ti_3Al intermetallic phases, which contributed to surface hardening and anti-wear performance [48]
Hybrid	SiO_2–Al_2O_3	Aluminum alloys (As-Cast A356)	• Combinations of two or more different particles are reinforced into the matrix material to combine the properties of the individuals • A–Si–Mg alloy like A356 is a potential material for piston components in automobiles. The mixture combination of 80% SiO_2 and 20% Al_2O_3 helped in achieving the best wear properties of piston aluminium alloy [49]
	Ni–Ti	Aluminum alloys (1100)	• Nitinol (Ni–Ti) particles were successfully embedded and dispersed in AA1100 matrix to induce residual tensile and compressive stresses in the parent matrix [50]
	SiC–MoS_2	Aluminum alloys (As-Cast A413)	• The addition of MoS_2 solid lubricant particles decreased the metal-to-metal adhesive mechanism and improved the tribological properties [51]
	αAl_2O_3–graphite	Aluminum alloys (6061)	• Graphite is used as a dry lubricant due to its inherent property of lack of carbon–carbon bonding between adjacent planes, which make it soft and slippery. AA6061–6% αAl_2O_3–0.5% graphite combination exhibited higher hardness and lower wear rate [52]

3.1.4 Tool Geometry and Tool Materials

For FS tool, pin and shoulder are the most important, which determine the plastic flow and forging pattern of the viscoplastic material. Pin profile and tool shoulder surface features significantly influence mixing of reinforcement particles and distribution in substrate. Following to the statement made, increasing trend of mixing and distribution can be seen in the given ascending order: plain cylindrical pin (with or without taper angle and changing pin diameter) < pin with multiple faces (triangular, square and hexagonal) [53] < pin with threads or flutes (Fig. 17). The maximum level of mixing and distribution for pins with threads and flutes is attributed to the material flow in vertical direction as well as lateral directions. This observation is

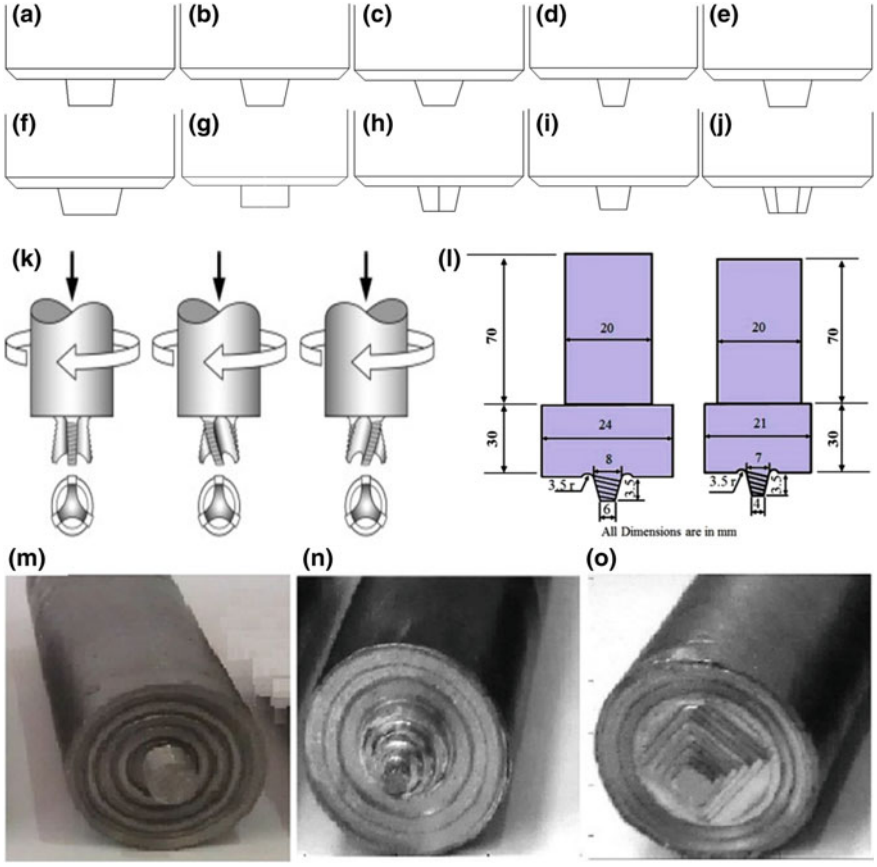

Fig. 17 Pictorial representation of tool geometries: **a–c** plain cylindrical pins with changing taper angle, **d–f** plain tapered cylindrical pins with varying pin diameters, **g** straight cylindrical pin, **h–j** tapered pins with multiple faces like triangular, square and hexagonal respectively, **k** Flared-Triflute™ type pin profiles with neutral, left hand and right hand flutes [54], **l** tapered threaded pins with concave shoulder [39] and **m–o** stepped pins with patterned shoulder [55]

evident for soft matrix materials like Aluminum and Magnesium. However, threaded and fluted pins are susceptible to excessive wear while working on high-strength and high-temperature matrices like Stainless steel, Titanium and Nickel. In such cases, tool geometry with stepped pin profile is preferred to avoid the tool damage without impeding mixing. The authors infer that to achieve acceptable mixing with minimum number of FS passes, the tool should be designed in view of the matrix material to be processed. The shoulder portion, too, can possess different designs features like concave, convex, flat, spheres, spiral and so on. These patterns help in restricting the plasticized material within the stir zone, reduce the amount of flash and produce a better depth of processed zone.

The tool material should be much harder than the matrix material to be processed to facilitate heat generation, plasticization and forging back the substrate material below the tool. Softer matrix materials such as aluminium, magnesium, copper and their alloys are mostly processed with the tool manufactured by hot work tool steels like: High-Carbon High-Chromium (HCHCr) [52], H13 [36, 49, 56, 57], SKD61 [58, 59] and 2344 [60–62]. The harder substrates like iron, titanium and their alloys are treated with the tool fabricated by Tungsten carbide material [41, 42].

3.1.5 Process Parameters Affecting the Performance of FSP

The two major dominating process parameters are tool rotation rate (ω, rpm) and tool traverse speed (v, mm/min). Higher tool rotation rate and lower traverse speed cause greater temperature due to increased frictional heating. It results in increased material stirring and reinforcement distribution. However, lower tool rotation rate and higher traverse speed tend to increase axial load and cause adverse effects. In addition to these two, tool tilt angle (°) with respect to the substrate surface is also an important process parameter. Tool tilt in the backward direction ensures effective forging back of the stirred material below the shoulder under pressure. Further, plunge depth (mm) of the pin and some portion of the shoulder into the substrate assist in formation of void-free processed region. Insufficient plunge depth may also result in surface groove due to incomplete flow of material around the tool. On the contrary, excessive plunge depth will result in sheet thinning and substantial loss of material in the form of flash. The number of FS passes with successive change in the direction of tool rotation changes the advancing side to retreating side and vice-versa. This helps in fragmentation and uniform distribution of secondary particles, reduced time for reaction kinetics to form in-situ intermetallics, greater reduction of grain size and thus contributes to enhanced material properties. The tool design is also one of the important factors affecting performance of FSP (as dealt in Sect. 3.1.4). Few of the studies highlighting the effect of process parameters are discussed in the ensuing paragraph.

Agrawal et al. [63] studied the effect of tool rotation rates on end forming behaviour of FSPed Al6063–T6 tubes. It was depicted that, the tool rotation rate was responsible for yielding initial hardness of the processed region and which in

turn governs the maximum load required during forming operations. Mehta and Badheka successfully joined dissimilar metals: AA6061–T651 with electrolytic tough pitch copper. In this study, tool rotation speed, traverse speed, tool pin offset, the position of work material were kept constant while the tool tilt angle was varied from 0 to 4°. The defect-free welding was achieved for tool tilt angles of 2°, 3° and 4°. The authors infer that increased tilt angle tends to increase the axial plunge load and due backward pressure of the tool shoulder, the stirred material gets forged and reduces the formation of flash [64]. Asadi et al. [60] correlated tool tilt angle and plunge depth to produce a sound surface layer. They reported that for the optimum values of plunge depth 0.22, 0.30 and 0.40 mm the tool tilt angles were 2.5°, 3° and 3.5° respectively. The study also revealed the drastic reduction in stir zone grain size from 150 to 7.17 μm and increased stir zone hardness of 96 HV as compared to average base material hardness of 63 HV. A major drawback in Aluminium-based composites is clustering of particles. Madhu et al. [65] eliminated this problem in fabricating CP-Al/TiO_2 nanocomposite using multiple-pass FSP. The TiO_2 particles of 1 μm were embedded into the CP-Al substrate by six passes. The results revealed that multiple passes fragmented the reinforcement particles to nano-scale and distributed uniformly. In between four to six passes, the progress in reaction kinetic of the Al–TiO_2 to form Al_3Ti and Al_2O_3 was observed in X-ray diffraction as shown in Fig. 18. The enhanced mechanical properties were ascribed to particle refinement and homogeneous distribution in the matrix. Nadammal et al. conducted various experiments on AA2024–T3 varying: (i) plunge depth, (ii) tool rotational speed and (iii) tool traverse speed. In each set of experiments only one process parameter was varied while the others were kept constant. The optimized results are tabulated in

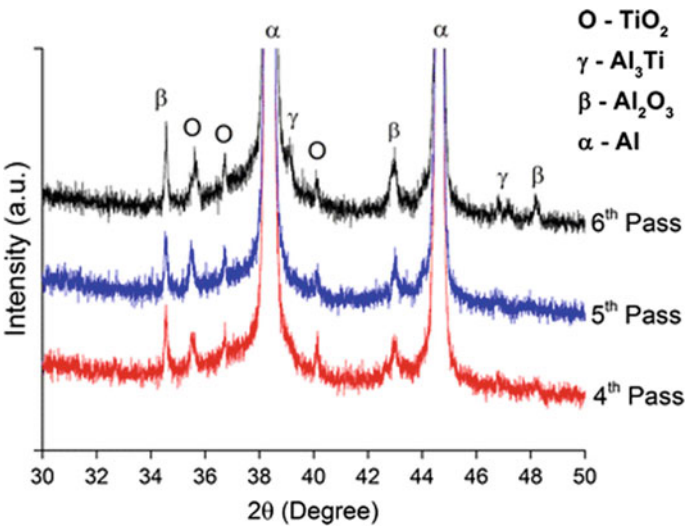

Fig. 18 X-ray diffraction analysis depicting the reduction of TiO_2 intensity with increasing the number of FSP passes and revealed the formation of Al_3Ti and Al_2O_3 intermetallics [65]

Table 3 Representing different sets of experiments. Set 1: varying plunge depth (mm), Set 2: varying tool rotation rate (rpm) and Set 3: Varying tool traverse speed (mm/min)

Set 1		Set 2		Set 3	
Varying plunge depth (mm)	5.00–5.8	Varying tool rotation rate (rpm)	200–1600 (varied in two steps: 200–900 and 900–1600)	Varying tool traverse speed (mm/min)	10–170 (varied in two steps: 10–90 and 90–170)
Constant tool rotation rate (rpm)	500	Constant plunge depth (mm)	5.63	Constant plunge depth (mm)	5.63
Constant tool traverse speed (mm/min)	25	Constant tool traverse speed (mm/min)	25	Constant tool rotation rate (rpm)	350
Remarks	Optimum plunge depth obtained was 5.63 mm	Remarks	Optimum tool rotation rate observes was 350 rpm	Remarks	Optimum tool traverse speed attained was 95 mm/min

Table 3. The defect-free and better mechanical properties were attributed to proper combination process parameters [66].

3.1.6 FSP and Its Potential in Surface Engineering Field

FSP has proved to be a potential candidate to compete with conventional surface engineering techniques. It can change the microstructure of the substrate to shallower as well as greater depths, deposit a coating layer using consumable tool or powdered reinforcement. Therefore, it offers an advantage of altering the texture of material as per the requirement of application. Further, it is possible to embed different kinds of reinforcement particulate to acquire wear resistance, corrosion resistance, magnetic effect, shape memory effect and lubrication effect in metallic materials. In recent years, a novel technological advancement was reported, wherein in-situ polymer derived nano-ceramic was developed in CP-Cu matrix via FSP. This simple technique finds a promising application in producing metallic foams and porous metallic structures to serve automotive, aeronautical, aerospace and biomedical industries [67–70].

4 Summary

The thermal spray classification is quite a wider one and caters to various applications in surface engineering field. It also, however, suffers from serious drawbacks. In addition to the bottlenecks aforementioned, one major drawback is change of phase while interacting with intense heat. This results in undesirable effects on the coating properties. Hence, at times, coatings deposited, with the least interaction with heat and the coatings which are solely obtained by severe plastic deformation, are preferred. Friction stir is a process that uses such frictional heat to soften and mix the material homogeneously in the vicinity of rubbing counterparts, forming a coating of tailored mechanical properties. Hence FSP and its variants due to their solid-state processing capability eliminate the drawbacks associated with thermal spray technique. The compatibility between the matrix and the coating material is found to be an important parameter in resolving any surface engineering problems. Further, reinforcements of ceramics, forms of carbon, pure metals and hybrids improve process effectiveness. The ceramics are used to increase surface hardness and acquire wear resistance, CNTs are embedded to combine its inherent property of high elastic modulus and tensile strength with the matrix material, pure metals are tried to form in-situ intermetallics which act as load-bearing elements and hybrid type is also experimented to combine the effect of two or more reinforcements to enhance the matrix material properties. The better material properties are achieved only if the reinforcement particles are distributed homogeneously into the matrix. The magnitude of mixing and distribution descends in the following order of tool geometry: pin with threads or flutes > pin with multiple faces > plain cylindrical pin. Further, a relatively higher tool rotation rate and lower tool traverse speed, 0–3° tilt angle and sufficient plunge depth are recommended to obtain a void-free sound processed region. Proper tool design and optimized process parameters would help in reducing the number of passes to acquire the desired sub-surface microstructure and congruently reduce the cycle time of the process from industrial perspective.

Acknowledgements Authors are thankful to KLS Gogte Institute of Technology, Belagavi, Karnataka, India, for setting up the Center of Excellence for Industrial Microwave Application in association with an industry partner—Enerzi Microwave Systems Private Limited, Belagavi, Karnataka, India. We are also thankful to the Minority Welfare Department, Directorate of Minorities, Government of Karnataka, India, for granting fellowship vide registration No. DOM/FELLOWSHIP/CR-15/2018-19 for pursuing Ph.D.

References

1. ASM Handbook Volume 5: Surface Engineering. ASM International (1994)
2. Jambagi, S.C.: Property Improvement of Thermally Sprayed Coatings Using Carbon Nanotube Reinforcement. Indian Institute of Technology, Kharagpur (2017)
3. Jambagi, S.C.: Scratch adhesion strength of plasma sprayed carbon nanotube reinforced ceramic coatings. J. Alloys Compd. **728**, 126–137 (2017)

4. Jambagi, S.C., Kar, S., Brodard, P., Bandyopadhyay, P.P.: Characteristics of plasma sprayed coatings produced from carbon nanotube doped ceramic powder feedstock. Mater. Des. **112**, 392–401 (2016)
5. Majumdar, J.D.: thermal and cold spraying technology in manufacturing. In: Handbook of Manufacturing Engineering and Technology, pp. 2805–2850. Springer, London (2014)
6. Fauchais, P.L., Heberlein, J.V.R., Boulos, M.I.: Industrial applications of thermal spraying technology. In: Thermal Spray Fundamentals: From Powder to Part, pp. 1401–1566. Springer (2014)
7. Jambagi, S.C., Bandyopadhyay, P.P.: Plasma sprayed carbon nanotube reinforced splats and coatings. J. Eur. Ceram. Soc. **37**(5), 2235–2244 (2017)
8. Pawlowski, L.: The Science and Engineering of Thermal Spray Coatings, 2nd edn. Wiley (2008)
9. Fauchais, P.: Current status and future directions of thermal spray coatings and techniques. In: Future Development of Thermal Spray Coatings, Woodhead Publishing, pp. 17–49 (2015)
10. Budinski, K.G.: Surface Engineering for Wear Resistance. Prentice-Hall, Inc, Englewood Cliffs, New Jersey, United States (1988)
11. Verdon, C., Karimi, A., Martin, J.-L.: A study of high velocity oxy-fuel thermally sprayed tungsten carbide based coatings. Part 1: Microstructures. Mater. Sci. Eng., A **246**(1–2), 11–24 (1998)
12. Kuroda, S., Kawakita, J., Watanabe, M., Katanoda, H.: Warm spraying—a novel coating process based on high-velocity impact of solid particles. Sci. Technol. Adv. Mater. **9**(3), 33002 (2008)
13. Ann Gan, J., Berndt, C.C.: Thermal spray forming of titanium and its alloys. In: Titanium Powder Metallurgy, pp. 425–446. Butterworth-Heinemann (2015)
14. Heimann, R.B.: Applications of plasma-sprayed ceramic coatings. Key Eng. Mater. **122–124**, 399–442 (1996)
15. Jambagi, S.C., Sarkar, N., Bandyopadhyay, P.P.: Preparation of carbon nanotube doped ceramic powders for plasma spraying using heterocoagulation method. J. Eur. Ceram. Soc. **35**(3), 989–1000 (2015)
16. Jambagi, S.C., Agarwal, A., Sarkar, N., Bandyopadhyay, P.P.: Plasma-sprayed titania and alumina coatings obtained from feedstocks prepared by heterocoagulation with 1 wt.% carbon nanotube. J. Mater. Eng. Perform. **27**(5), 2364–2372 (2018)
17. Dorfman, M.R.: Thermal spray coatings. Handb. Environ. Degrad. Mater., 469–488 (2018)
18. Mishra, R.S., Mahoney, M.W., McFadden, S.X., Mara, N.A., Mukherjee, A.K.: High strain rate superplasticity in a friction stir processed 7075 Al alloy. Scr. Mater. **42**(2), 163–168 (1999)
19. Mishra, R.S., Ma, Z.Y.: Friction stir welding and processing. Mater. Sci. Eng. R Reports **50**(1–2), 1–78 (2005)
20. Ma, Z.Y.: Friction stir processing technology: a review. Metall. Mater. Trans. A **39**(3), 642–658 (2008)
21. Bajakke, P.A., Malik, V.R., Deshpande, A.S.: Particulate metal matrix composites and their fabrication via friction stir processing–a review. Mater. Manuf. Process. **34**(8), 833–881 (2019)
22. Farias, A., Batalha, G.F., Prados, E.F., Magnabosco, R., Delijaicov, S.: Tool wear evaluations in friction stir processing of commercial titanium Ti–6Al–4V. Wear **302**(1–2), 1327–1333 (2013)
23. Padhy, G.K., Wu, C.S., Gao, S.: Friction stir based welding and processing technologies—processes, parameters, microstructures and applications: a review. J. Mater. Sci. Technol. **34**, 1–38 (2017)
24. Gandra, J., Pereira, D., Miranda, R.M., Vilaça, P.: Influence of process parameters in the friction surfacing of AA 6082–T6 over AA 2024–T3. Procedia CIRP **7**, 341–346 (2013)
25. Yu, M., Zhang, Z., Zhao, H., Zhou, L., Song, X.: Microstructure and corrosion behavior of the ultra-fine grained aluminum coating fabricated by friction surfacing. Mater. Lett. **250**, 174–177 (2019)
26. Liu, S., Bor, T.C., Van Der Stelt, A.A., Geijselaers, H.J.M., Kwakernaak, C., Kooijman, A.M., Mol, J.M.C., Akkerman, R., Van Den Boogaard, A.H.: Friction surface cladding: an exploratory study of a new solid state cladding process. J. Mater. Process. Tech. **229**, 769–784 (2016)

27. Van Der Stelt, A.A., Bor, T.C., Geijselaers, H.J.M., Akkerman, R., Van Den Boogaard, A.H.: Cladding of Advanced Al Alloys Employing Friction Stir Welding, vol. 554–557, pp. 1014–1021 (2013)
28. Khodabakhshi, F., Marzbanrad, B., Shah, L.H., Jahed, H., Gerlich, A.P.: Surface modification of a cold gas dynamic spray-deposited titanium coating on aluminum alloy by using friction-stir processing. J. Therm. Spray Technol. **28**(6), 1185–1198 (2019)
29. Rani, M., Perumal, G., Roy, M., Grewal, H.S., Singh, H., Arora, H.S.: Post-processing of Ni–Cr–Al_2O_3 Thermal spray coatings through friction stir processing for enhanced erosion–corrosion performance. J. Therm. Spray Technol., pp. 1–12 (2019)
30. Mane, K.M., Hosmani, S.S.: Friction stir surface processing of Al 6061 alloy: role of surface alloying with copper and heat-treatment. Trans. Indian Inst. Met. **71**(6), 1411–1425 (2018)
31. Rao, K.P., Sankar, A., Rafi, H.K., Ram, G.D.J., Reddy, G.M.: Friction surfacing on nonferrous substrates: a feasibility study. Int. J. Adv. Manuf. Technol. **65**(5–8), 755–762 (2013)
32. George Sahaya Nixon, R., Mohanty, B.S., Sathish, R.: Friction surfacing of AISI 316 over mild steel: a characterisation study. Def. Technol. **14**(4), 306–312 (2018)
33. Nixon, R.G.S., Mohanty, B.S., Bhaskar, G.B.: Effect of process parameters on physical measurements of AISI316 stainless steel coating on EN24 in friction surfacing. Mater. Manuf. Process. **33**(7), 778–785 (2018)
34. Dolatkhah, A., Golbabaei, P., Besharati Givi, M.K., Molaiekiya, F.: Investigating effects of process parameters on microstructural and mechanical properties of Al5052/SiC metal matrix composite fabricated via friction stir processing. Mater. Des. **37**, 458–464 (2012)
35. Asadi, P., Faraji, G., Masoumi, A., Givi, M.K.B.: Experimental investigation of magnesium-base nanocomposite produced by friction stir processing: effects of particle types and number of friction stir processing passes. Metall. Mater. Trans. A Phys. Metall. Mater. Sci. **42**(9), 2820–2832 (2011)
36. Cartigueyen, S., Mahadevan, K.: Wear characteristics of copper-based surface-level micro-composites and nanocomposites prepared by friction stir processing. Friction **4**(1), 39–49 (2016)
37. Salekrostam, R., Besharati Givi, M.K., Asadi, P., Bahemmat, P.: Influence of friction stir processing parameters on the fabrication of SiC/316L surface composite. Defect Diffus. Forum **297–301**, 221–226 (2010)
38. Shamsipur, A., Kashani-Bozorg, S.F., Zarei-Hanzaki, A.: The effects of friction-stir process parameters on the fabrication of Ti/SiC nano-composite surface layer. Surf. Coatings Technol. **206**(6), 1372–1381 (2011)
39. Parumandla, N., Adepu, K.: Effect of tool shoulder geometry on fabrication of Al/Al_2O_3 surface nano composite by friction stir processing. Part. Sci. Technol., 1–10 (2018)
40. Suvarna Raju, L., Kumar, A.: Influence of Al_2O_3 particles on the microstructure and mechanical properties of copper surface composites fabricated by friction stir processing. Def. Technol. **10**(4), 375–383 (2014)
41. Ghasemi-Kahrizsangi, A., Kashani-Bozorg, S.F., Moshref-Javadi, M., Sharififar, M.: Friction stir processing of mild steel/Al_2O_3 nanocomposite: modeling and experimental studies. Metallogr. Microstruct. Anal. **4**(2), 122–130 (2015)
42. Shafiei-Zarghani, A., Kashani-Bozorg, S.F., Gerlich, A.P.: Strengthening analyses and mechanical assessment of Ti/Al_2O_3 nano-composites produced by friction stir processing. Mater. Sci. Eng., A **631**, 75–85 (2015)
43. Liu, Q., Ke, L., Liu, F., Huang, C., Xing, L.: Microstructure and mechanical property of multi-walled carbon nanotubes reinforced aluminum matrix composites fabricated by friction stir processing. Mater. Des. **45**, 343–348 (2013)
44. Soltani, M., Shamanian, M., Niroumand, B.: Surface characteristics improvement of AZ31B magnesium by surface compositing with carbon nano-tubes through friction stir processing. Int. J. Adv. Des. Manuf. Technol. **8**(1), 85–95 (2015)
45. Chen, W.L., Huang, C.P., Ke, L.M.: A novel way to fabricate carbon nanotubes reinforced copper matrix composites by friction stir processing. Adv. Mater. Res. **391–392**, 524–529 (2011)

46. Mahmoud, E.R.I., Al-qozaim, A.M.A.: Fabrication of in-situ Al–Cu intermetallics on aluminum surface by friction stir processing. Arab. J. Sci. Eng. **41**(5), 1757–1769 (2016)
47. Azizieh, M., Mazaheri, M., Balak, Z., Kafashan, H., Kim, H.S.: Fabrication of $Mg/Al_{12}Mg_{17}$ in-situ surface nanocomposite via friction stir processing. Mater. Sci. Eng., A **712**, 655–662 (2018)
48. Li, B., Shen, Y., Lei, L., Hu, W.: Fabrication and evaluation of Ti3Alp/Ti–6Al–4V surface layer via additive friction-stir processing. Mater. Manuf. Process. **29**(4), 412–417 (2014)
49. Akbari, M., Shojaeefard, M.H., Asadi, P., Khalkhali, A.: Wear and mechanical properties of surface hybrid metal matrix composites on Al–Si aluminum alloys fabricated by friction stir processing. Proc. Inst. Mech. Eng. Part L J. Mater. Des. Appl., 1–10 (2017)
50. Dixit, M., Newkirk, J.W., Mishra, R.S.: Properties of friction stir-processed Al 1100-NiTi composite. Scr. Mater. **56**(6), 541–544 (2007)
51. Janbozorgi, M., Shamanian, M., Sadeghian, M., Sepehrinia, P.: Improving tribological behavior of friction stir processed A413/SiCp surface composite using MoS2 lubricant particles. Trans. Nonferrous Met. Soc. China **27**(2), 298–304 (2017
52. Prakash, T., Sivasankaran, S., Sasikumar, P.: Mechanical and tribological behaviour of friction-stir-processed al 6061 aluminium sheet metal reinforced with Al_2O_3/0.5 Gr hybrid surface nanocomposite. Arab. J. Sci. Eng. **40**(2), 559–569 (2014)
53. Malik, V., Kailas, S.V.: Plasticine modeling of material mixing in friction stir welding. J. Mater. Process. Technol. **258**, 80–88 (2018)
54. Thomas, W.M., Johnson, K.I., Wiesner, C.S.: Friction stir welding-recent developments in tool and process technologies. Adv. Eng. Mater. **5**(7), 485–490 (2003)
55. Arab, S.M., Zebarjad, S.M., Jahromi, S.A.J.: Fabrication of AZ31/MWCNTs surface metal matrix composites by friction stir processing: investigation of microstructure and mechanical properties. J. Mater. Eng. Perform. **26**(11), 5366–5374 (2017)
56. Ahmadifard, S., Kazemi, S., Momeni, A.: $A356/TiO_2$ nanocomposite fabricated by friction stir processing: microstructure, mechanical properties and tribologic behavior. JOM (2018)
57. Faraji, G., Dastani, O., Akbari Mousavi, S.A.A.: Microstructures and mechanical properties of Al_2O_3/AZ91 surface nanocomposite layer produced by friction stir processing. Proc. Inst. Mech. Eng. Part B J. Eng. Manuf. **225**(8), 1331–1345 (2011)
58. Mahmoud, E.R.I., Takahashi, M., Shibayanagi, T., Ikeuchi, K.: Effect of friction stir processing tool probe on fabrication of SiC particle reinforced composite on aluminium surface. Sci. Technol. Weld. Join. **14**(5), 413–425 (2009)
59. Morisada, Y., Fujii, H., Nagaoka, T., Fukusumi, M.: Nanocrystallized magnesium alloy—uniform dispersion of C60 molecules. Scr. Mater. **55**(11), 1067–1070 (2006)
60. Asadi, P., Faraji, G., Besharati, M.K.: Producing of AZ91/SiC composite by friction stir processing (FSP). Int. J. Adv. Manuf. Technol. **51**(1–4), 247–260 (2010)
61. Asadi, P., Givi, M.K.B., Abrinia, K., Taherishargh, M., Salekrostam, R.: Effects of SiC particle size and process parameters on the microstructure and hardness of AZ91/SiC composite layer fabricated by FSP. J. Mater. Eng. Perform. **20**(9), 1554–1562 (2011)
62. Barmouz, M., Asadi, P., Besharati Givi, M.K., Taherishargh, M.: Investigation of mechanical properties of Cu/SiC composite fabricated by FSP: effect of SiC particles' size and volume fraction. Mater. Sci. Eng. A **528**(3), 1740–1749 (2011)
63. Agrawal, A.K., Narayanan, R.G., Kailas, S.V.: End forming behaviour of friction stir processed Al 6063-T6 tubes at different tool rotational speeds. J. Strain Anal. Eng. Des. **52**(7), 434–449 (2017)
64. Mehta, K.P., Badheka, V.J.: Effects of tilt angle on the properties of dissimilar friction stir welding copper to aluminum. Mater. Manuf. Process. **31**(3), 255–263 (2016)
65. Madhu, H.C., Ajay Kumar, P., Perugu, C.S., Kailas, S.V.: Microstructure and mechanical properties of friction stir process derived Al-TiO_2 nanocomposite. J. Mater. Eng. Perform. **27**(3), 1318–1326 (2018)
66. Nadammal, N., Kailas, S.V., Suwas, S.: A bottom-up approach for optimization of friction stir processing parameters; a study on aluminium 2024-T3 alloy. Mater. Des. **65**, 127–138 (2015)

67. Ajay Kumar, P., Raj, R., Kailas, S.V.: A novel in-situ polymer derived nano ceramic MMC by friction stir processing. Mater. Des. **85**, 626–634 (2015)
68. Ajay Kumar, P., Yadav, D., Perugu, C.S., Kailas, S.V.: Influence of particulate reinforcement on microstructure evolution and tensile properties of in-situ polymer derived MMC by friction stir processing. Mater. Des. **113**, 99–108 (2017)
69. Ajay Kumar, P.: Evolution of in-situ nano-pores during friction stir processing of polymer derived ceramic reinforced metal matrix composites. Res. Reports Met. (2017)
70. Pathak, S., Saha, G. C.: Sustainable development of cold spray coatings and 3D additive manufacturing components for repair/manufacturing applications: a critical review. Coatings **7**(8), 122–149 (2017). https://doi.org/10.3390/coatings7080122

Development and Surface Engineering of TiNi Shape Memory Alloy

Hargovind Soni, S. Narendranath, P. M. Mashninini, Abhinaba Roy, T. Sebin Binoy, K. Jyothi, J. Rojina, and Abhilash Krishnan

Abstract Shape memory alloys are currently replacing many conventional materials due to their various useful properties. Besides shape recovery above austenitic temperature and pseudo-elasticity, high strength and good corrosion properties are one of the many mentionable properties of these alloys. Due to their intriguing properties, aerospace, biomedical and automotive industries are leading the research frontier for these smart materials. This chapter presents the results of an experimental investigation conducted on development of Ti rich shape memory alloy by arc melting and hot rolling, and its surface study when machined by wire-EDM. The developed and machined specimens of TiNi alloys were also tested. Tensile study of the specimens showed that material rigidity has decreased due to intensive rolling process. Scan electron microscopic analysis of the fractured surface confirmed that the mode of failure of the rolled specimen was ductile in nature. Characteristic properties like necking, dimple formation, cracks which are related to ductile failure of metallic materials are clearly visible in the SEM micrographs. Micro hardness test revealed that micro hardness of the rolled specimens are much higher than as cast TiNi alloy and less along the edge of the fracture surface compared to bulk rolled material.

Keywords Shape memory alloy · Rolling · Wire-EDM · Surface

1 Introduction

Shape-memory alloys 'SMA' are smart materials and have extensive applications in biomedical, scientific, and industrial fields. This material consists of two very exclusive characteristics named shape memory effect and pseudo-elasticity [1, 2]. The utmost active and popularly utilized alloys include CuZnAl, CuAlNi and NiTi

H. Soni (✉) · P. M. Mashninini
Department of Mechanical and Industrial Engineering Technology, University of Johannesburg, Johannesburg, South Africa
e-mail: hargovindsoni2002@gmail.com

S. Narendranath · A. Roy · T. Sebin Binoy · K. Jyothi · J. Rojina · A. Krishnan
Department of Mechanical Engineering, National Institute of Technology, Mangalore, Karnataka, India

K. Gupta (ed.), *Surface Engineering of Modern Materials*, Engineering Materials,
https://doi.org/10.1007/978-3-030-43232-4_2

(Nickel–Titanium). Titaniumrich, titanium-nickel shape memory alloy's characteristics are resulting from an alterable solid-state phase transformation commonly called as a martensitic transformation, in between two diverse martensite crystal stages. At greater temperatures, TiNi pertained as an interpenetrating simple cubic structure known as austenite (also termed the parent phase). At lower temperatures, TiNi instantly transforms into a further complex monoclinic crystal structure termed as martensite (daughter phase). Four transition temperatures are linked to the martensite-to-austenite and austenite-to-martensite transformations. Initially from complete austenite, martensite starts to formulate as an alloy, which is cooled at a temperature known as martensite start temperature (M_s). The transformation is completed at a temperature known as martensite finish temperature (M_f). Austenite begin to form when the alloy is fully martensite and is exposed to heating, at a temperature termed as austenite start temperature (A_s), and complete at the austenite finish temperature (A_f) [1]. The application areas of TiNi alloys are manifolds [3–7]:

1. Thermal and electrical actuators.
2. Biomedicaland Bio compatible applications.
3. Damping systems in structural engineering.

Modern research and development have shown that TiNi processing can ameliorate the thermomechanical proficiencies, and allow multiple shape memories to be integrated within a monolithic structure. Investigation is in progress on multi-memory technology and promise to deliver ameliorated shape memory devices as well as application via new materials and materials structures in the upcoming days [3, 4]. Kauffman et al. [5] investigated that TiNi eyeglass frames are more flexible because it can be bent completely out of shape and then regain its shape. TiNi needle wire localizers is used to point out the breast tumors, so that further surgery can be accurate and less offensive because of the property of the metal's shape memory. Further applications in the field of medical using TiNi is as a companion for catheters through blood.

There are numerous benefits of SMAs which will be utilized in safety devices in upcoming days to save lives. Fire-sprinklers and anti-scalding devices using TiNi alloys are already in the market. Shower heads and water faucets are utilizing anti-scalding valves where the flow of water is automatically shut off beyond a certain temperature due to the use of TiNi alloy type shape memory alloys.

TiNi is being utilized to simulate motion of human muscle in micromanipulators and robotics actuators. Wei et al. [7] reported that TiNi torsion springs can yield the persistent moment of forces. TiNi torsion spring having persistent elasticity can be utilized to open the satellite's door or to release the antenna effectively to decrease the influence and vibration so as to enhance the security of the complete system. Li et al. [8] studied that TiNi-based Shape Memory Alloy (SMA) structure having Negative Poisson's Ratio (NPR), creates a multi-functional structure that can be utilized as a reusable armor [9–12]. The study evaluates the impact of selective laser melting onto the micro-structural and structural integrity progress in a TiNi alloy.

Literature review on machining of shape memory alloys including TiNi indicates the occurrence of major problems with conventional machining techniques [13]. Titanium and its alloys are well-thought-out as problematic to-cut materials because of high hardness, low thermal conductivity, and low elastic modulus. It consequently results in high thermal stresses, frequent tool wear, deterioration in work surface quality, low material removal rate, defects in microstructure etc. Certain special machining methods (like the utilization of rotary tools and edge tools and other non-conventional machining techniques) may be believed as an alternative technique to enhance the material removal rate and other machinability indicators on condition that the component geometry integrity allows this. Extra care must be taken to evade loss of surface integrity in the machining of titanium and its alloys, particularly grinding, or an intense loss in mechanical behavior like fatigue can result. Normally, the crack-free subsurface structure and compressive residual stress ormed during machining ensure outstanding fatigue characteristics, at the same time as surface damage and a tensile residual-stress pattern will outcome in an intense loss in performance [14]. Similarly, drilling, milling, broaching and other machining of titanium and its alloys i.e. TiNi are also challenging [15].

Furthermore, some nonconventional or advanced machining of TiNi alloys has also been explored. Where electric discharge machining processes most importantly wire-EDM (WEDM) has been extensively explored to machine TiNi or NiTi alloys [16]. Previous research shows that optimum WEDM process has the potential to generate favourable surface integrity properties on the machined specimen. Irrespective of the material properties, except electrical conductivity, WEDM has been found superior among other advanced processes to obtain better surface finish, fatigue strength, microstructure, residual stresses, and micro-geometry characteristics [17–19].

As known that TiNi alloys are smart materials of significant importance, and their machining is challenging; therefore, wire-EDM has been selected in this work to machine TiNi. Firstly, TiNi alloys were developed by vacuum arc melting, followed by rolling, and then cut by wire-EDM to prepare the specimen for testing and characterization. Surface characterization has been done and effect of wire-EDM has been investigated on the properties of the developed TiNi alloy. Further sections of this chapter present the various aspects of investigation in detail.

2 Experimental Details

2.1 Vacuum Arc Melting

Both Titanium and Nickel are highly reactive in nature and form oxides easily when cast using traditional techniques. Due to high reactivity of the corresponding elements with the atmosphere, inert environment is preferred over oxygen clad atmosphere. This characteristic of TiNi SMA is exhibited due to its unique crystal structure which

is easily disrupted if any impurities are present. So to avoid this from happening, they should be developed in an environment free of oxygen, nitrogen, carbon and any other potential contaminations. Therefore, Vacuum Arc Melting (VAM) apparatus was selected to be used for melting the high purity ingots of Titanium and Nickel. Ingots of pure Titanium and Nickel were procured from commercial sources. After cutting the pure metals into small pieces, they were cleaned with acetone and weighed as required in an electronic balance with accuracy of 0.0001 g. After performing proper measurement, they were placed in the copper crucible of the vacuum melting furnace for melting operation. After proper vacuum (10^{-5} mbar) is reached, argon gas was filled in the vacuum chamber to create an inert atmosphere so as to avoid contamination in the chamber during melting operation. Figure 1 exhibits setup of vacuum arc melting furnace for TiNi alloy development.

The vacuum arc menting procedure has made a breakthrough in the metallurgical techniques industries, which were utilizing the traditional methods specifically used in the aviation, biomedical and aerospace fields. The unit as depicted in Fig. 1 is utilized especially for TiNi alloys. Benefits of using this method over conventional methods are manifolds:

- It is easy to regulate the solidification rate of molten material. Therefore, a high degree of control over the microstructure and the capability to minimize segregation can be easily achieved.
- The gases liquefied in liquid metal throughout melting metals in open furnaces, like oxygen, nitrogen and hydrogen are termed to be damaging to the majority of alloys and steels. These gases outflow from liquid metal under vacuum circumstances into the vacuum chamber.
- Elements with greater vapor pressure like sulfur, carbon and magnesium (normally contaminants) are lowered in concentration.

Fig. 1 Vacuum arc melting unit

2.2 Materials

In the current investigation, titanium nickel binary alloy has been developed using Vacuum Arc melting technique. Titanium and nickel were procured from commercial sources bearing purity of 99.97% and 99.83% respectively. Each sample with specification as in Table 1 was re-melted 6 times to maintain homogeneity.

2.3 Rolling

The developed TiNi alloy was processed further by cold rolling and then hot rolling in which work thickness was reduced by compressive forces exerted by two opposing rolls and to make the thickness uniform. The Rolling machine shown in Fig. 2 was used for the rolling operation of the TiNi alloy specimens along with the furnace as shown in Fig. 3.

2.4 Wire Electric Discharge Machining

Since TiNi shape memory alloys are difficult to machine using conventional techniques, therefore wire-EDM that found effective to handle a wide range of engineering materials, is explored in the present work. Hence, in the present work, the rolled specimens of the developed TiNi alloy were cut using wire-EDM to obtain samples for the mechanical properties testing and surface characterization. Wire electro discharge machine by Electronica Ecocut ELPULS15 shown in Fig. 4 was used to cut

Table 1 Specification of the TiNi sample

Alloy	Weight	Density
$Ti_{50}Ni_{50}$	8 g	6.45 g/cm^3

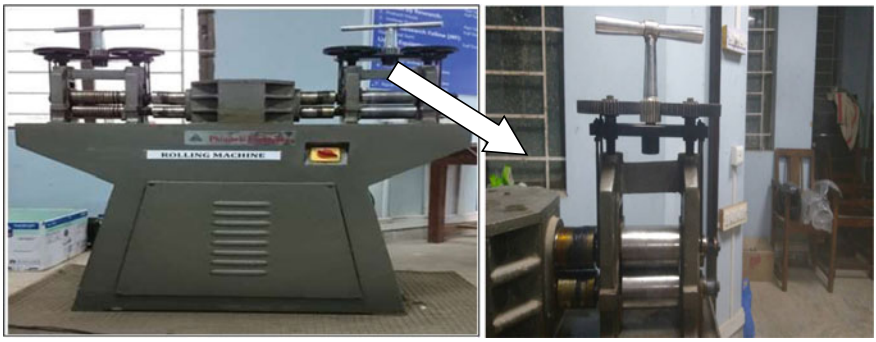

Fig. 2 Rollingmachine

Fig. 3 Furnace used while hot rolling of TiNi alloy

Fig. 4 Wire-EDM machine tool

the specimens of the size as recommended by ASTM E8 standard (see Fig. 5). Four important wire-EDM process parameters i.e. pulse-on time, pulse-off time, wire feed rate and servo voltage were kept fixed at their optimum values (Table 2). Figure 6 shows the wire-EDM machine chamber and Fig. 7 depicts the cut specimen.

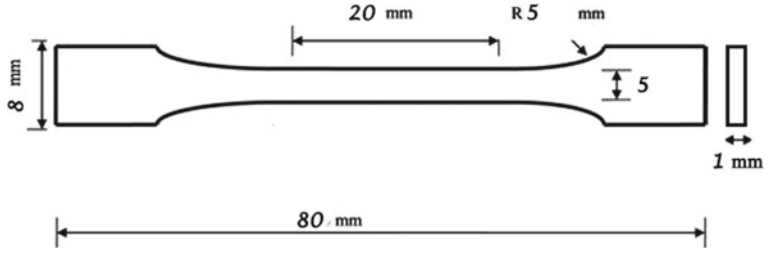

Fig. 5 Dimensions of cut specimen of TiNi alloy

Table 2 Optimum wire-EDM parameters used to cut TiNi alloy

Pulse off duration/time (T_{off})	Pulse on duration/time (T_{on})	Wire feed rate	Servo voltage
40 μs	120 μs	4 m/min	30 V

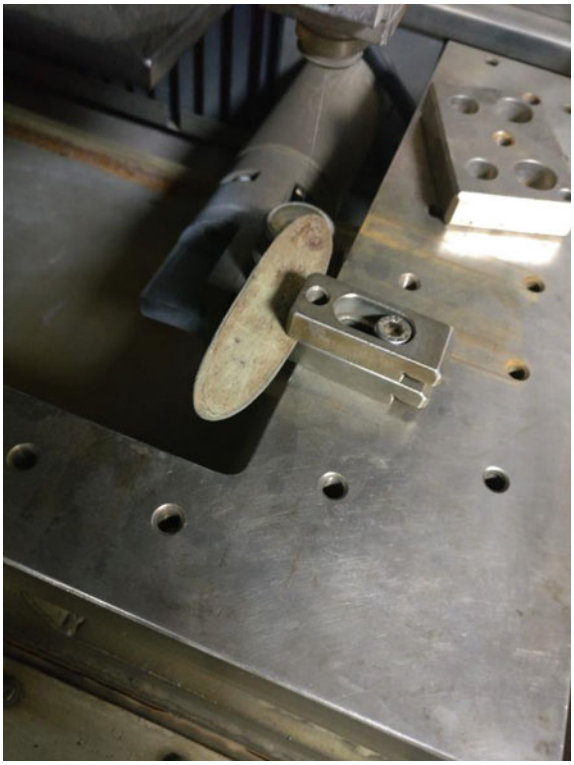

Fig. 6 Test specimens prepared using wire EDM

Fig. 7 Actual TiNi specimen cut by wire-EDM

2.5 Testing and Measurement

The tensile testing of the TiNi specimens was done on a universal testing machine (UTM) (Fig. 8). The TiNi alloy specimens were tested based on the ASTM standards. Based on the application and the characteristics to be determined, the ASTM standard is selected and thus the specimens were machined to the required dimensions. The strain rate used was 2 mm/min.

TiNi shape memory alloys developed through vacuum arc melting furnace without passing through rolling and TiNi rolled specimen both were exposed to micro-hardness test to study the change in their microhardness. Further, the micro-hardness testing of wire-EDM cut TiNi alloy is also done. Micro-hardness tester MVH-S-AUTO by Omni Tech as shown in Fig. 9 was used in the current investigation where 100 mg load was realistic for a dwell time of 10 s. The indentation was captured using an image analyzer integrated into the microhardness setup to measure the diagonals. Thereafter, the microhardness value was estimated using the built in software 'Quantimet'.

Scan electron microscope (SEM) was used for surface characterization.

Fig. 8 UTM used in present work

3 Results and Discussion

3.1 Effect of Rolling

Vacuum arc melted $Ti_{50}Ni_{50}$ shape memory alloys were subjected to cold and hot rolling using a rolling machine. It has been observed that during cold rolling, the sample suffered failure due to severe crack formation. Figure 10a illustrates the button shape of TiNi alloy directly from vacuum arc melting and Fig. 10b shows the cold rolled specimen of TiNi alloy. The thickness of the sample was measured after each 50 passes. For the initial 100 passes, the change in thickness observed is approximately 0.5 mm. On further continuation, after 150 passes a crack formation is observed along the edge of the specimen. On further rolling, after 200 passes crack propagation was observed along the width of specimen. So, after 250 passes the rolling process was stopped due to severe crack propagation. A total reduction of 1 mm in thickness is measured after 250 passes. Since cold rolling of the specimen lead to crack formation, which is not desired, it was decided that this method was not suitable for rolling specimen into sheets. To avoid crack formation and propagation, hot rolling is carried out above recrystallization temperature of the TiNi shape memory alloy at 800 °C.

A total of 5 samples are prepared using vacuum arc melting and out of which 4 samples are hot rolled into sheets as illustrated in Fig. 11.

Fig. 9 Microhardness testing machine

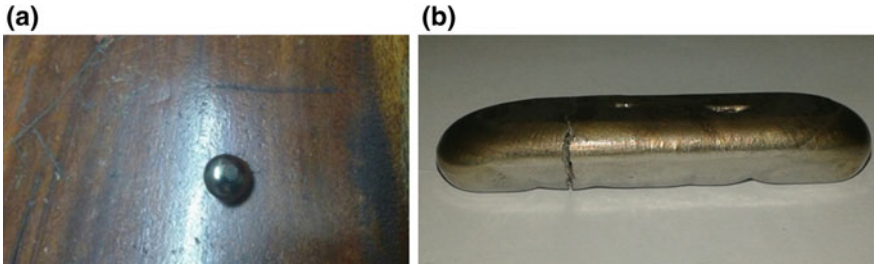

Fig. 10 **a** Button shape TiNi specimen produced by vacuum arc melting, **b** cold rolled TiNi specimen

In hot rolling, the manufactured button cells were heated in the furnace to above re-crystallisation temperature of 800 °C and left for some time. When it became red-hot, hot rolling was done for 2 passes and then the workpiece was left in the furnace again for 5 min.

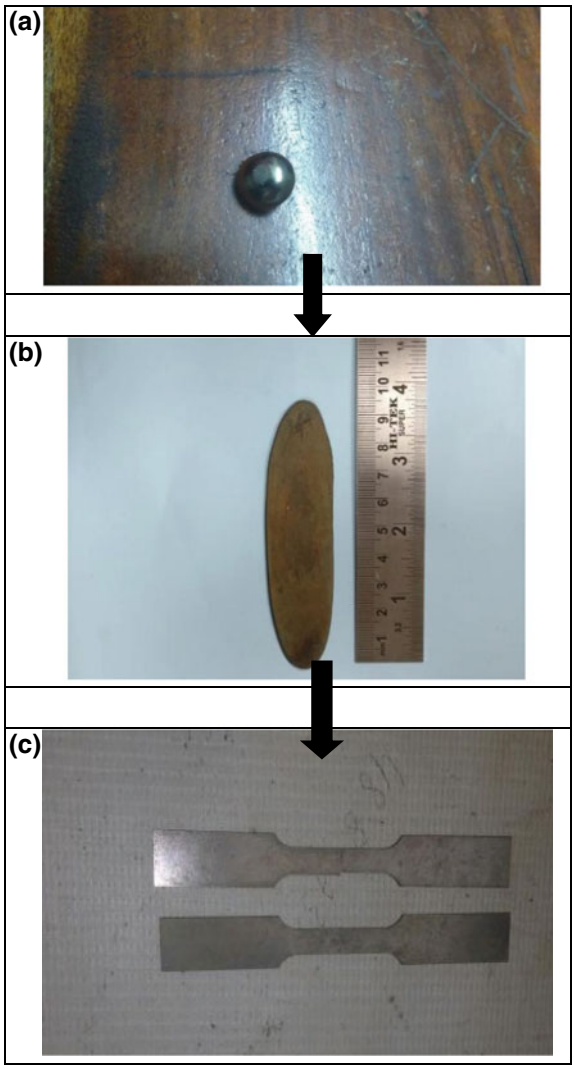

Fig. 11 Process sequence from obtaining button shape TiNi specimen after vacuum arc melting (**a**), their hot rolling (**b**), rolled TiNi specimen cut by wire-EDM (**c**)

Specimen dimensions before rolling were as follows:

Width between adjacent surfaces = 18.85
Thickness = 11.97 mm

Specimen dimensions after hot rolling are as follows:

Thickness = 1.2 mm
Length of rolled plate = 95–110 mm
Width = 18–24 mm

3.2 *Results of Tensile Testing*

Four specimens of TiNi alloy cut by wire-EDM were subjected to the tensile test. The stress strain curve of sample/specimen 1 depicts a very high Young's modulus and low ductility as seen from Fig. 12. This is because the sample underwent a very slow rolling process followed by an indentation on the surface during the rolling process by the tongs. The indentation caused by the tongs may have reduced the ductility of the sample. But the reason for the high Young's modulus which is a measure of rigidity of the material is unknown. The other samples 2, 3, and 4 showed striking uniformity in the results as given in Table 3. The Young's modulus of the sample has comparatively decreased significantly during the process of hot rolling. The Young's modulus for TiNi specimen from literature was found in the range of 28–41 GPa.

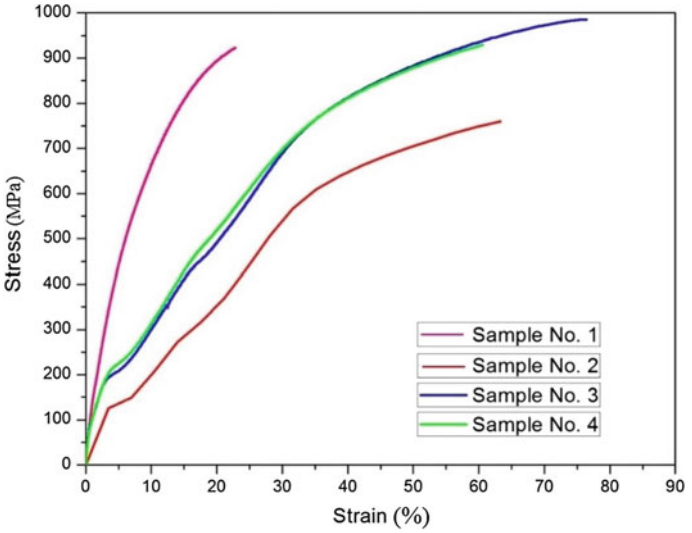

Fig. 12 Stress–strain graph obtained from universal testing machine

Table 3 Universal testing machine readings

Sample no.	Width (mm)	Thickness (mm)	Area (mm^2)	Modulus (MPa)	Ultimate force (N)	Ultimate stress (MPa)	Gauge length initial (mm)	Gauge length final (mm)
1	5	1.12	5.91	2665	4500	760	20	24.06
2	5	1.05	5	1470	4510	901	20	34.583
3	5	1.17	5.92	1350	5740	969	20	35.294
4	5	1.05	5.25	1520	4740	903	20	32.138

This shows that the rigidity of the material has decreased on continuous hot rolling. This is due to dislocations in the crystal lattices.

Similarly, the ultimate tensile strength of the samples have also reduced from 1900 MPa to the values as given in Table 3 again due to dislocations in the crystal lattice. It is worth mentioning that 1900 MPa is the tensile strength of TiNi alloy specimen which is not subjected to hot rolling.

The Tensile testing results of the TiNi shape memory show that Young's modulus and the Ultimate tensile strength have reduced due to dislocations caused in the crystals structure induced due to hot rolling. The strength of a material with no dislocations is very high. However, at moderate dislocation density values, the materials exhibit a significantly lower tensile strength. The dislocations are caused during hot rolling because, after each rolling pass, strain is imparted to the material.

3.3 SEM Analysis

There were no mechanical (e.g., strain vs. plane stress) or physical (e.g., surface roughness) diversity in between specimens. However, it is sensible to characterize the observed diversity in the fatigue behavior which is exclusive to each specimen. Figures 13 and 14 present the scan electron microscopic images to understand the capability of wire-EDM to generate the subsurface characteristics of TiNi alloy type difficult-to-machine material.

The presence of dimples points to the failure of TiNi layers due to microvoid coalescence. The dimples that arise enlarge and during further yielding, the material between them is necked and sheared and hence the voids coalesce. Also, the presence of the dimples confirms that ductile failure has occurred in the sample. Also, the depth of the dimples can be approximated as a measure of the specimen's ductility. Hence, the investigation result is that the mode of fracture is confirmed as ductile fracture. For a clear representation, the pores and the dimples are circled in the below Fig. 13 same as presented in Fig. 14 for each sample.

3.4 Microhardness Analysis

Thesamples for micro-hardness test and indentation images are shown in Fig. 15. Three readings were taken each for the unrolled button, rolled specimen, and wire-EDM cut specimen underwent tensile testing. Average of the three readings is considered (Table 4).

In case of wire-EDM cut tensile test specimen, the micro-hardness test was conducted for 9 different points on the fractured specimen, 3 points P7, P8, P9, just next to the fractured surface and 6 points away from the fracture surface with point P1 the furthest (Fig. 16). Reference point is considered at the closest area of the machined surface since it is tremendously problematic to measure the microhardness accurately on the machined edge because of inappropriate indentations. The depression closest

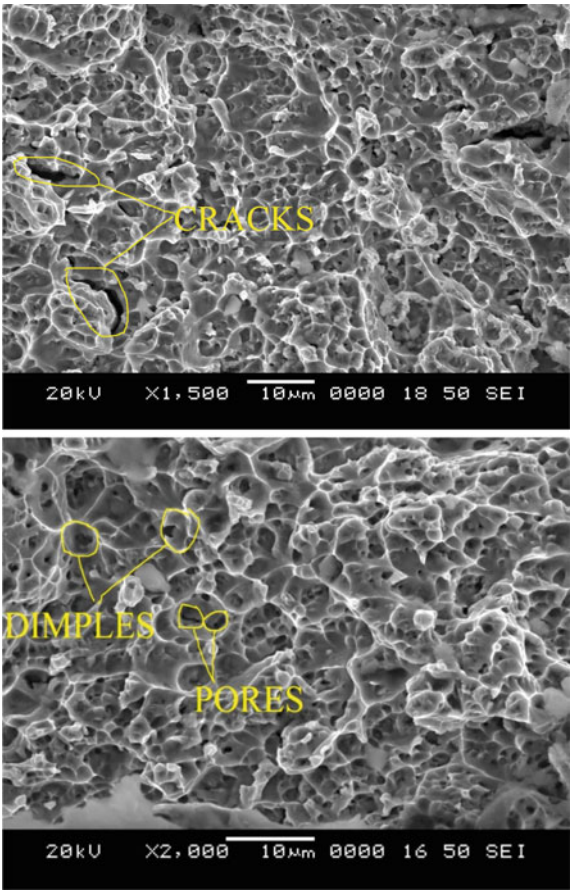

Fig. 13 Microstructure of TiNi indicating cracks, pores and dimples as observed from SEM

to the machined surface is relatively bigger, but not rhombus exactly due to metallurgical variation that came into existence during WEDM process. The micro-hardness values corresponding to each point are presented in Table 5.

It can be noted that the hardness decreases as the measurements are taken closer to the fractured surface. This was expected because at the fractured surface, the grains are elongated due to ductile fracture and that led to the appreciable decrease in hardness. Most importantly, increments in micro-hardness are found from the arc melting to wire-EDM cutting. Higher hardness represents presence of the compressive residual stresses, that is important for the higher fatigue strength and longer life of the TiNi machined by wire-EDM.

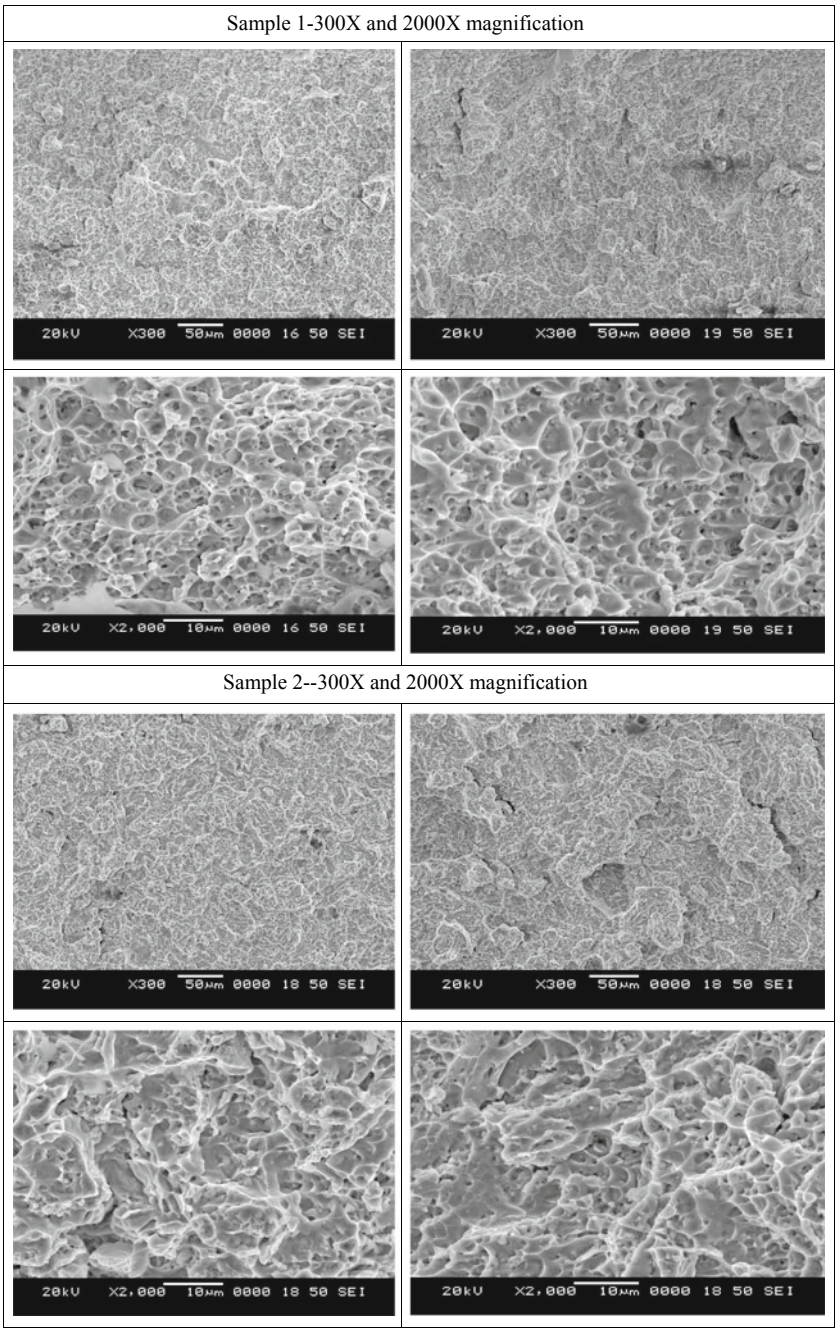

Fig. 14 SEM analysis of all four specimens of TiNi

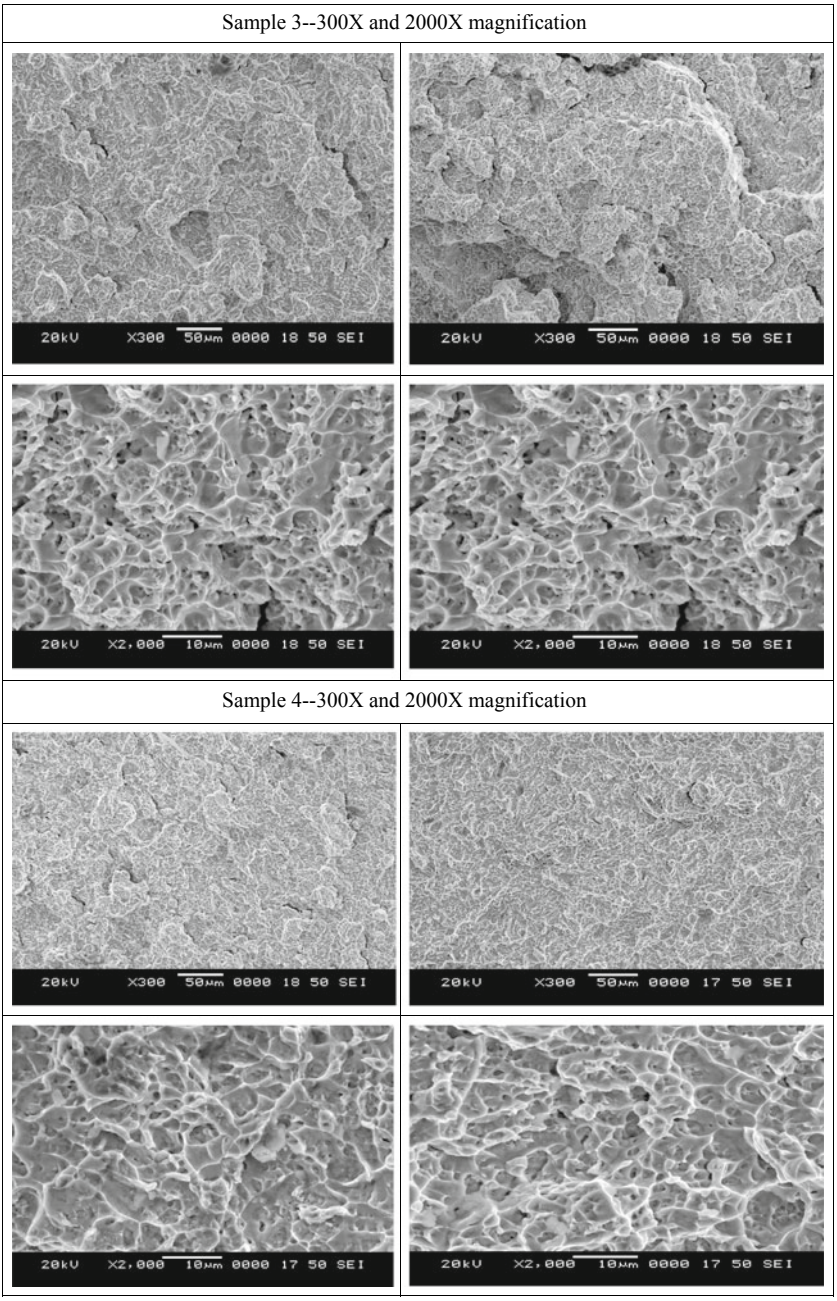

Fig. 14 (continued)

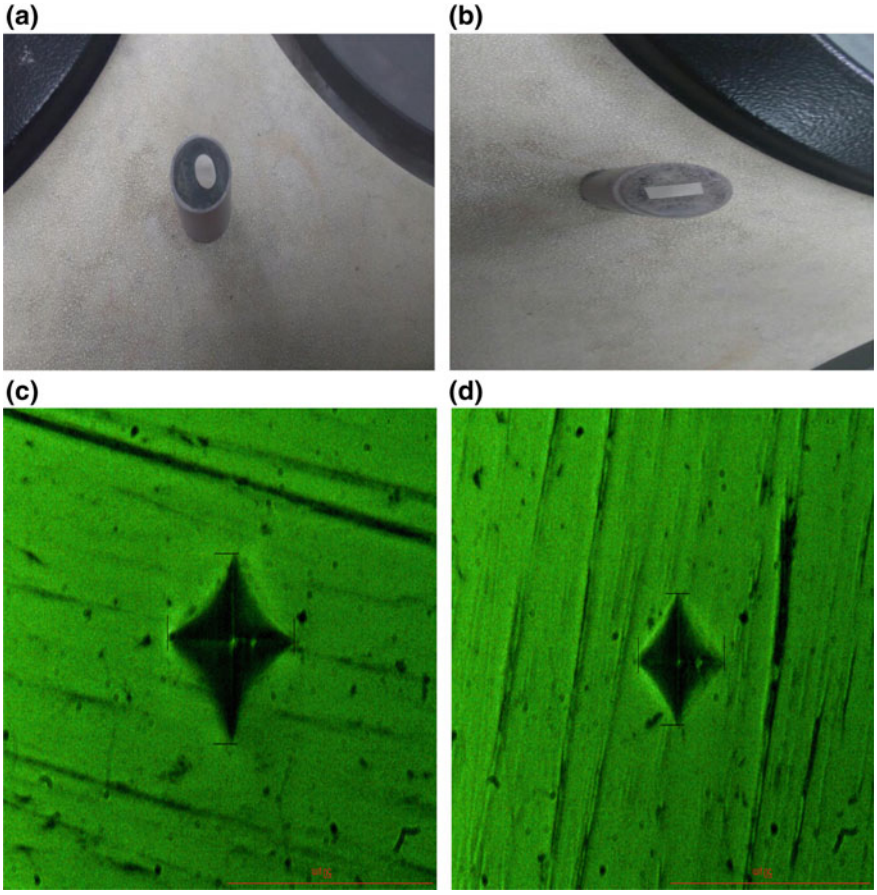

Fig. 15 **a** and **b** Polished specimens before conducting micro-hardness test **c** and **d** cross section of specimens showing indentation

Table 4 Micro-hardness results

Reading no.	Unrolled TiNi	Hot rolled TiNi
R1	191.6576	323.9013
R2	207.8699	376.4472
R3	213.733	399.8781
Hardness value	204.4202 Hv	366.7422 Hv

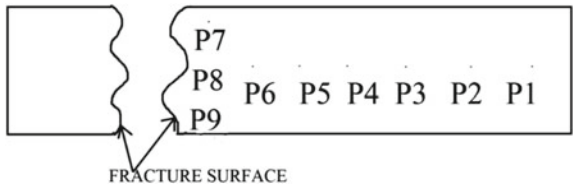

Fig. 16 Locations of micro-hardness testing points for wire-EDM cut tensile tested specimen

Table 5 Hardness values at different points

Point	P1	P2	P3	P4	P5	P6	P7	P8	P9
Hardness value (Hv)	399.87	397.89	390.84	390.84	384.98	355.017	335.35	321.67	347.45

4 Conclusions

This chapter reports the development, processing, and wire-EDM cutting of TiNi shape memory alloy and its surface characteristics and mechanical properties. The following conclusions can be drawn from this research work:

1. Cold rolling doesn't yield satisfactory results during rolling of TiNi shape memory alloys making hot rolling more suitable.
2. Tensile testing of the TiNi shape memory alloys showed that the Young's modulus and the Ultimate tensile strength has reduced due to dislocations caused in the crystals structure induced due to hot rolling.
3. From SEM analysis, it was confirmed that ductile failure occurred during tensile testing of the hot rolled samples. Simultaneously, cracks and dimples are observed which further clarifies the failure mode.
4. In microhardness test, it was confirmed that hot rolled specimens are harder than the TiNi specimen obtained directly by arc melting. By measuring the microhardness along the fracture surface, it was confirmed that due to ductile failure the hardness was less near the fracture zone compared to hot rolled material.

References

1. Mehta, K., Gupta, K.: Fabrication and processing of shape memory alloys. Springer International Publishing, Switzerland (2019)
2. Magabe, R., Sharma, N., Kapil Gupta, J., Davim, P.: Modeling and optimization of wire-EDM parameters for machining of Ni55.8–Ti shape memory alloy using hybrid approach of Taguchi and NSGA-II. Int. J. Adv. Manuf. Technol. **102**(5), 1703–1717 (2019)
3. Piller, J.: A Case Study—Hardness testing assures quality in advanced materials (2014). https://www.qualitymag.com/articles/91828-hardness-testing-assures-quality-in-advanced-materials
4. Qian, L., Xiao, X., Sun, Q., Yu, T.: Erratum: anomalous relationship between hardness and wear properties of a superelastic nickel-titanium alloy (Appl. Phys. Lett. **84**, 1076 (2004)). Appl. Phys. Lett. **86**(12), 1 (2005)
5. Page, C.O., Kauffman, G.B., Mayo, I.: For Magazine (October 1993)
6. Batalu, D.: A review on TiNi shape memory alloys (SMA) used for medical applications. Recycling aspects (November 2014)
7. Cai, W., Zheng, Y., Meng, X., Zhao, L.: Superelasticity in TiNi alloys and its applications in smart systems. **479**, 1915–1920 (2005)
8. Li, S., Hassanin, H., Attallah, M.M., Adkins, N.J.E., Essa, K.: Acta materialia the development of TiNi-based negative poisson's ratio structure using selective laser melting. Acta Mater. **105**, 75–83 (2016)
9. Wu, S.K., Lin, H.C., Yen, Y.C.: A study on the wire drawing of TiNi shape memory alloys. Mater. Sci. Eng. A **215**(8), 1–2, 113–119 (1996)
10. Zheng, Y., Huang, B., Zhang, J., Zhao, L.: The microstructure and linear superelasticity of cold-drawn TiNi alloy. Mater. Sci. Eng. A **279**(7), 1–2, 25–35 (2000)
11. Shahmir, H., Nili-ahmadabadi, M., Mansouri-arani, M., Langdon, T.G.: The processing of NiTi shape memory alloys by equal-channel angular pressing at room temperature. Mater. Sci. Eng., A **576**, 178–184 (2013)

12. Ahadi, A., Rezaei, E., Karimi Taheri, A.: Effect of hot rolling on microstructure and transformation cycling beaviour of equiatomic NiTi shape memory alloy. Mater. Sci. Technol. **28**(6), 727–732 (2012)
13. Wu, S.K., Lin, H.C., Chen, C.C.: A study on the machinability of a $Ti_{49.6}Ni_{50.4}$ shape memory alloy. (6), 27–32 (1999)
14. Ezugwu, E.O., Wang, Z.M.: Materials titanium alloys and their machinability. **68**, 262–274 (1997)
15. Lin, H.C., Lin, K.M., Chen, Y.C.: A study on the machining characteristics of TiNi shape memory alloys. **105**(9), 327–332 (2000)
16. Manjaiah, M., Narendranath, S., Basavarajappa, S.: Review on non-conventional machining of shape memory alloys. Trans. Nonferrous Met. Soc. China **24**(1), 12–21 (2014)
17. Sharma, N., Gupta, K., Davim, J.P.: On wire spark erosion machining induced surface integrity of $Ni_{55.8}Ti$ shape memory alloys. Arch. Civ. Mech. Eng. **19**(3), 680–693 (2019)
18. Jaware, V.B., Takale, A.M.: Review on EDM and wire-EDM machining of TiNi shape memory alloys. **3**(1), 99–108 (2015)
19. Prajesh, P., Chawla, P.: A review on the machining of titanium alloys using WEDM, 34–40 (2015)
20. Gupta, K., Jain, N.K.: Deviations in geometry of miniature gears fabricated by wire electrical discharge machining. In: Proceedings of International Mechanical Engineering Congress & Exposition (IMECE 2013) of ASME, V010T11A047, San Diego, California, USA, pp. 13–21 Nov (2013)

Wear of Rubbers and Its Control in Conveyer Belt System

Dilip Thapa Masrangi, Hadinata Salim, F. Hakami, A. Pramanik, and A. K. Basak

Abstract Rubbers are polymer materials characterized by the ability of reversible deformation under influence of external deformation forces, described as a material with elastic properties. Rubbers include natural rubber, naturally occurring substance and synthetic rubber, artificially derived from petrochemical product. Products made from rubber have flexible and stable 3-dimensional chemical structure and the ability to stretch repeatedly of about twice the original length and return to original length. These materials are enormously used in conveyer belt system. Today, rubber materials are altered with approximately 60% synthetic polymers to achieve desired properties of final product. This chapter investigates the wear of different types of rubbers against ceramic liners which is the most realistic case in mining industries, where conveyor belts are used for ore transportation pulleys in conveyer belt system are coated with sacrificial liners of ceramics and rubbers to prolong the life of the conveyor system. However, such pulley liners are exposed to wear and even chemical reactions particularly in mining industries that are involved in transporting ores. The investigation will provide information on surface in terms of wear mechanism of rubber against ceramics, wear rate and appearance of wear surfaces.

1 Introduction

As one of the primary tasks in mining industry, materials handling, is very important and carried out via conveyor belt system. Cost of maintaining conveyor belt system is one of the big contributors to overall mines' maintenance cost [1]. Wear is an obvious contributor in this aspect, however, unwanted materials from mining activity have the ability to damage the machinery which may incur extra maintenance cost [2]. Conveyor system is the most common procedure used in transporting mining materials in bulk [3]. Conveyor system usually consist of a drive pulley, a tail pulley and multiple

D. T. Masrangi · H. Salim · F. Hakami · A. Pramanik (✉)
Department of Mechanical Engineering, Curtin University, Bentley, Perth, Australia
e-mail: alokesh.pramanik@curtin.edu.au

A. K. Basak
Adelaide Microscopy, The University of Adelaide, Adelaide, South Australia, Australia

K. Gupta (ed.), *Surface Engineering of Modern Materials*, Engineering Materials,
https://doi.org/10.1007/978-3-030-43232-4_3

troughing idlers in between. Being a significant aspect in mining materials handling, pulley liners which are usually made from combinations of ceramic and rubber, experience abrasive wear after some period [4]. Aluminium oxide-based ceramic, like alumina, is widely known as a material with remarkable strength, exceptional hardness, high melting point, and resistivity to corrosion. Hence, this material has been extensively used as pulley liners where durability is a significant aspect. However, due to ceramic's high cost and low impact resistance, rubber was introduced to form a ceramic-rubber lagging. The common elastomers widely used for this purpose are [5]: (a) Nitrile rubber (NBR), (b) Natural rubber (NR), (c) Acrylic rubber (ACM), (d) Hydrogenated nitrile butadiene rubber, (e) Ethylene propylene rubber and (f) Styrene—butadiene rubber (SBR).

Natural rubber (NR) is a polymeric material that contain mainly oxygen and hydrogen atoms; allowing to ignite easily and burn rapidly [6]. It has very high elasticity, high tensile strength with poor abrasion resistance. The material is obtained by coagulation of latex derived from rubber tree. It is obtained through a series of steps that involves collection of latex and followed by filtering, washing and chemically reacting with diluted acid such as formic acid to coagulate rubber particles. After which, coagulated particles are pressed into sheets before drying them (Woodford, 2008). Natural rubber polymer is generally 100% cis-1,4 polyisoprene with molecular weight (Mw) ranging from 1 to 2.5×10^6 [7]. Natural rubber is not resistant to aging and oil; hence it is seldom used as a seal for technical applications but combined with other elastomer compound to improve its rubber properties.

The unique properties of rubber attracted great demand for it. As such, to accommodate high demand, synthetic rubbers were produced by means of poly-reaction of the chain or gradual character [8, 9]. Unlike natural rubbers with one chemical structure, synthetic rubbers have many variations each with its own unique properties. Such development allowed industries to customize rubber product to specific demand. Hence, synthetic rubbers are used for many applications such as tires, hoses, belts and floorings.

2 Wear and Friciton: Tribology

Tribology is described as a combination of friction, wear and lubrication [10]. Mechanically, this term describes the technicality when surfaces moving relative to each other come in contact. It includes the study and application of the principles of friction, wear and lubrication. According to Stachowiak and Batchelor [11], based on the result obtained from experiments and theories, tribology involves the study of characteristics films of intervening material between colliding bodies. The concerns of either film failure or absence of a film usually manifested by severe friction and wear.

The basic idea of tribology is that, friction and wear are best handled with a thin layer or intervening layer of substance separating the sliding, rolling and impacting bodies (form of lubrication). Hence, aim of tribology is either to predict the sequence

of events when a sliding/rolling/impacting contact is left to generate its own intervening film or to find an optimum sacrificial material for a given application. One of the main purposes of tribology is to achieve economic savings as massive economic losses due to wear and friction have happened throughout decades in mining industries [12]. Although lubrication has been extensively used to overcome material's wear that is caused by friction, optimal efficiency is yet to be achieved [13]. Therefore, by conducting tribology studies, possible solutions to the challenges and problems are expected to be achieved.

2.1 Wear

Wear is primarily caused by the occurrence of friction, in which wear in material causes energy loss and wastage. Generally, lubrication is used to handle wear and reduces friction [14]. Therefore, tribology study focuses on minimisation of friction and wear to improve component efficiency. Even though minimisation of both friction and wear appears to be the most desirable option, but it will not be very desirable for object such as tyre. Generally, tyre requires less wear and high friction. However, component such as gears would require the minimisation in both friction and wear [15].

Wear, particularly three-body wear is the primary focus of this study. An extensive study on commonly occurring wear in mining industry is hence carried out. Wear is the progressive loss of material from the surface of an object due to mechanical means such as contact with and frictional motion against a solid, liquid or gaseous counter body [16]. Wear rate can vary drastically depending on operating conditions, material selections and dynamic parameters [17]. Eventually, progressive loss of material can result in financial loss due to equipment failure, downtime for repairs and replacement of wear-out parts. Adachi and Hutchings [17] further mentions that, wear can be in different types based on surface interaction of colliding bodies. According to Adachi and Hutchings [17], four major wear modes are adhesive wear, abrasive wear, fatigue wear and corrosive wear. As such, these wear mechanisms will be further elaborated.

Adhesive wear is where relative movement of two bodies cause wear on contacting bodies. In such cases, two contacting surfaces resist relative sliding and due to dislocation, it induces large plastic deformations. As a result of deformation, crack is originated and transmitted in combined fracture mode of tensile and shearing. Eventually, when crack reaches contact interfaces, a wear particle is formed and resulted in adhesive wear [18]. In cases where milder form of wear occurs, particles are generated due to repeated cycle of contact in a form of cracks. Such fatigue process is caused by repetitive stresses under either sliding or rolling and known as fatigue wear [18]. In cases where film material comprises of solid particles or moves against a body without providing support against another body, ploughing takes place. As a result, material from weaker surface is removed and this phenomenon is known as abrasive wear [18]. Wear caused due to impact of solid or liquid particles against

the surface of an object and gradually removing material through repeated deformation and cutting action, is known as erosive wear [18]. Other form of wear includes cavitation wear, corrosive wear, oxidative wear, fretting wear, impact wear, melting wear and diffusive wear. As far as engineering is concerned, all wear types are undesirable occurrence and mostly related to deterioration of functional capability and depreciation of value. Any reduction in wear can result in considerable savings [11].

Abrasive wear can be in a form of two-body or three-body. Typically, movement of grits determine types of abrasive wear [19]. Two-body wear generally have grits that is firmly attached on either surface when abrasion occurs. On the other hand, three-body wear has grits that is free to roll between connecting bodies when abrasion occurs. In relation to the focus of this project, most relevant wear mechanism will be focused upon. In essence, three body abrasive wear will be highlighted, as it is the most common form of wear in conveyor belt system used in mining industry. Regardless, it is important to understand both forms of abrasive wear: 2-body and 3-body.

3 Ore Handling

Different kind of ores are handled in mining industries and out of them, iron ore is the fourth most abundant element that accounts for estimated 5% of the earth's crust [20]. It is commonly found in a form of iron ore and has been used for centuries in making weaponries and tools. It is mindboggling for a modern society with the absence of iron ore, as it is an essential part in the manufacture of steels that are used abundantly. Total annual production of iron has increased from over 607 million tonnes in 2000 to 1670 million tonnes in 2015 [20]. To accommodate the increasing production of iron ore, use of mining equipment also has to increase proportionately.

Mining equipment includes conveyor belts that are used for transportation of excavated materials over large distance [21]. Increasing production rate of iron ore over the year results in higher use of conveyor belts, which reduces the workload in mines significantly, decreases investment in capital construction, shorten construction periods and generates socio-economic benefits. As such, increasing use of conveyor system invites higher risk of damaging conveyor system due to friction and wear [22].

In view of this, the purpose of present chapter is to determine the most suitable belt and pulley lining for a conveyor system used to transport iron ore. As such, conveyor system, particularly belt and pulley were reviewed based on factors such as effect of force on 3-body wear due to iron ore particles.

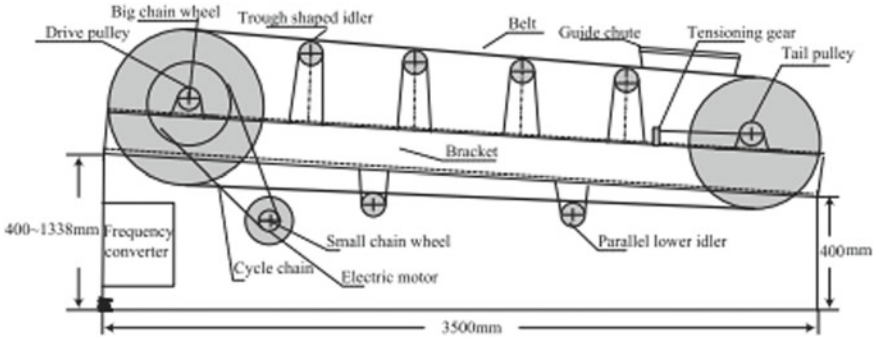

Fig. 1 Conveyor belt schematic [24] (with kind permission from Elsevier)

3.1 Conveyor Belt System

Simply defined, conveyor is any system that contains two or more pulleys with the continuous loop of material, called conveyor belt. The belt is supported by structure members that hold the pulleys in place, called conveyor structure. Conveyor belts systems have been meaningfully industrialized for decades as they perform a vital role in today's large scale continuous transport systems [23]. It is one of the most effective conception for transporting bulk materials in numerous field of industries [24]. These industries includes mining, handling bulk material, timber industry and many other fields where great extent of goods are transported over distance that range from few meters to hundreds of kilometres [25]. Figure 1 indicates the general design of a conveyor belt system.

Generally, rollers between drive pulley and return pulley are known as idler rollers. The rollers below the load are called impact rollers that perform a specific task with high intensity workloads. The weight carrying rollers are known as carrying rollers or idler rollers. The rollers that support the belt on reverse motion direction is known as return idler sets, which are same as carrying idler sets. The idler spacing for return idlers are much larger than carrying idlers. Depending on application of conveyor belts, design of common belt conveyor arrangements can be very complex. Ultimately, regardless how conveyor systems are designed to suit intended application, abrasive wear is merely unavoidable.

3.2 Conveyor Belt

One critical component of conveyor system is the conveyor belt. Belt selection plays an integral role in minimising wear [26]. Belts are usually made up of three components: cover, carcass, and coating [27]. The cover rubber is the layer (top and bottom) that comes in contact with transported materials, while carcass is located

underneath to provide support from the load impact. The function of the coating is to hold the cover and carcass in place (Roulunds). These belts can be distinguished in many aspects such as according to carcass, steep angle or covers. The belts can also be in a form of woven wire, hinge metal or plastic, depending on the applications. To maximize the use of any conveyor belt, it is important to choose right type of belt suited for specific application. Not doing so can significantly affect throughput, downtime and even compromise safety. One aspect of belt to consider is the angle of response of a material, which is also known as 'angle of natural friction'. Such angle is the position at which materials loaded on belt takes up to the angle of the plane.

In general, important parameters for design of belt conveyor are belt speed, belt width, gear box selection, drive pulley shaft and absorbed power. In view of the present work, emphasis is on 'wear'; hence material of the belt is another crucial parameter to consider. Following examples illustrate different types of belts applicable to different working conditions [28].

Abrasion resistant belts (type A) are based with natural rubber and recommended for conveying large lumps of abrasive materials through difficult conditions. They are generally resistant to high impact energy and maximum temperature resistance of 70 °C. Such belts are not recommended for oily, acidic, alkali media but resistant to oxygen, impacts and abrasion. Flame resistant belts (type B) are generally based with chloroprene rubber covers. They are suited for harsh working conditions similar to type 'A' Belts. Furthermore, they have a higher maximum temperature tolerance up to 100 °C. Such conveyors belts are commonly used in underground mines. Heat resistant belts (type C) are commonly based with EPDM covers suited for conveying high-temperature materials that range from 100 to 400 °C with belt surface temperature between 60 °C and 200 °C. Such belts are resistant to acids, oxygen, water, ozone and commonly used in foundries or cement works. Oil resistant belts (type D) are commonly based with nitrile covers. They are suited for conveying working in oily and greasy environment. These belts have maximum working temperature of 90 °C and are resistant to acids, aliphatic and aromatic hydrocarbons. Such conveyor belts are commonly used in glass works or fertilizer plants.

The year 1979 marked the advancement of technology that allowed testing of conveyor belt damage and degradation [23]. In case of conveyor belts, despite different resistive type belts, debris that are present and likewise external parameters, contributes to wear and friction of pulleys and belts. Material wears does not only depend on the nature of material but also other elements such as geometry of contacting pairs, surface topography, loading, lubrication and environment [29]. Additionally, variation of friction and wear rate also depended on interfacial conditions such as normal load, geometry, relative surface motion, sliding speed, surface roughness, material type, system rigidity, temperature, humidity, lubrication and vibration [30].

Environmental condition is one of the causes behind negative impact on conveyor belt system. Especially for belts operating in abrasive atmospheres such as mining industries, conveyors often exhibit a high degree of belt land and tooth flank wear. Chowdhury [30] states that, sliding speed and normal load are two major contributing to wear and friction. Based on past investigation, wear rate increases with the increase

in normal load and sliding speed for polymers such as gear fibre, glass fibre, nylon and PTFE.

Another parameter linked to the cause of conveyor belt damage is a degradation influence of heat factor. This damage arises because of high temperature of transported material or due to high ambient temperature [31]. The effect of temperature includes formation of cracks. According to Fedorko et al. [31], these crakes are a result of contact between belt and hot transported material; and such, cracks can entre as deep as inner textile structure of the belt. Operation of rubber belt at elevated temperature (greater than 85 °C) for long duration also causes the rubber compound to harden and back crack due to bending and even melting over prolonged period.

Additionally, ASTM G65 test was carried out to study the effects of temperature on wear rate on four high silicon content steel quenched and aus-tempered at 300 and 320 °C [32]. It was observed that, wear rate increases with temperature. This is justified by the fact that, all materials exhibited similar increasing wear rate behaviour as initial room temperature was increased [32]. Thermal damage of conveyor belt is a result of an insufficient maintenance, improper operational conditions, inconveniently selection of conveyors belt or producer failure [31]. Hence, failure can be eliminated fully if necessary conditions are fulfilled.

3.3 Pulley

Within conveyor system, apart from conveyor belt, a pulley is recognized as most important component [33] which play an essential role in the performance and reliability of conveyor belt system [34]. Design of conveyor pulley ensure power transmission from motor to belt experience a minimum friction loss [35]. Although pulley diameter contributes in achieving ideal speed, pulley are usually manufactured according to the ISO 3684 or DIN 22101 standard diameter size [36].

Pulley is a standard cylindrical drum. However, it is what goes around the pulley that become vital for conveyor belt operation. Rubber and ceramic are two main materials utilised in conveyor pulley; however, its lagging pattern is also significant in determining pulley lifetime. Pulleys are installed on conveyor belt system to drive, redirect, provide tension or help track conveyor belt. They are classically mounted in exterior bearings and driven by an external drive source. Apart from drive or head pulley, many other pulleys may co-exist in a conveyor system.

To accommodate different types of pulleys, a conveyor system have the configuration such as, (a) Idler pulley—used in non-drive position, rotates freely and be driven by belt, (b) Tail pulley—redirects a conveyor belt back to drive pulley, (c) Snub pulley—increases belt wrap around drive pulley to improve traction, (d) Take-up pulley—eliminates slack and provide tension, (e) Bend pulley—redirects belt and provides belt tension where bend occurs, and (f) Conveyor roller—used either in bed as a support for conveyed load or as return section under bed as support for conveyor belt [37]. Apart from the arrangement of different pulleys orientated in one

conveying system, pulley configuration is another aspect that greatly impacts the ability of conveyor system to effectively operate in desired conditions [37] such as: (a) drum style pulleys are of cylindrical, shell, tube or pipe shaped hence providing for nonstop contact with conveyor belt; hence highly preferred in drive positions, (b) wing style pulleys are non-continuous contact surface comprising of a series of individual fins that allow loose materials to fall away. Robust fins incorporate support for gussets and rings. (c) spiral style pulleys have metal strip contact surface secured in a spiral pattern round outside of a drum. Continuous contact enhances material removal which is primarily used in bulk handling systems, and (d) angled wing pulleys consist of wing angled towards edge to achieve continuous contact with belt while improving material removal. To maximize removal, some design features cleanout ports.

Wear of components such as on conveying pulleys are of main concerns in all industries. Prevention or deceleration of wear is one of the most challenging yet most vital aspect [38]. As such, pulley linings as means of sacrificial layers are utilised in modern pulleys to minimize damage on pulleys in a conveyor system. Pulley lagging is applied to increase productivity and reduce downtime. Main forms of pulley linings are rubber linings, ceramic linings or combination of both. Picking pulley lagging with accurate properties for application is vital to get maximum pulley life [39]. Proper lagging increases the coefficient of friction between pulley and belt.

Pulleys can be coated with different materials in varying pattern to meet required applications need. In light with this work, main focus of the material used was on rubber and primarily, ceramic lagging. As such, respective characteristics of two materials are analysed.

4 Lining Materials

The most commonly used liners for pulley are ceramic/rubber lagging which provides a great lifespan compared to any other materials. Ceramic's wear resistance and rubber's shock resistance are combined to deliver the needs of ore handling process in conveyor belt [40]. Thus, this section will evaluate each material properties accordingly.

4.1 Rubber

In a conventional belt conveyor device, rubber lining has been widely used on outer periphery of belt contacting surface of drive pulley [41]. Doing so increases the coefficient of friction between pulley and conveyor belt hence ensuring friction grip even under adverse conditions such as moisture and soiling. Not only its ability to deform elastically is highly regarded, rubber is also widely considered as a tough material, and obviously invincible to corrosion [42]. On the other hand, rubber has

a lower melting point than ceramic. Rubber's bulk modulus ranges between 2000 and 3000 MPa which is considerably high when compared to its Young's modulus of ceramic which is around 0.5–3.0 MPa [43]. However, Suginaka [41] further adds that rubber coated pulleys wear-out fast and require replacement every 2–3 months. As such, other alternatives are considered such as ceramic (alumina) lagging. Rubber is categorised as polymers [44] and it has broad range of variations. Natural rubber has wide range of applications whereas styrene butadiene (synthetic) has slightly less applications. According to bin Samsuri [43], although NR has oil resistance capability that SBR does not possess, SBR is better in terms of wear resistance and abrasive resistance. Furthermore, NR has a tackier surface when compared to SBR.

Chlorobutyl rubber is a synthetic rubber formed by chlorine and butyl reaction [45]. This rubber was typically created in order to attain faster cure rate, increased adhesion, and thermal resistance (ExxonMobil). Chlorobutyl is also a type of synthetic rubber that has similar properties to SBR but better in terms of few properties mentioned in previous line.

4.2 Ceramic

Ceramics are widely used in engineering industry due to their exceptional strength, hardness, elevated melting point and resistance to corrosion that makes them suitable for high temperature operation and wear resistance operation [46]. Due to its mixed ionic-covalent bonding, most ceramic is known to be brittle. Furthermore, majority of ceramic has low heat and electric conductivity [47]. Ceramic is defined as a term for products that are made from non-metallic inorganic substances. Traditionally, clays were used to make pottery, bricks and tiles. The atomic bonding in ceramic is either of covenant or ionic character [48]. In case of ionic bonding, repulsive forces of electrically charged atoms restrict the slip of atoms while for covalent bonding, strength of bands prevent slip. Such limitation in slippage of atoms hence limits plastic deformation of ceramic, making it a hard material.

Alumina (Al_2O_3) is the most commonly used ceramic due to its high ability in almost every aspects such as strength, hardness, temperature, and corrosion resistance [49], Shackelford and Doremus [50], Figiel et al. [51]. Some of its applications are on anti-corrosive paint, abrasives, cutting tools, and mining liners. Its chemical and thermal stability, its good strength together with thermal and electrical insulation characteristics with its availability in abundance makes alumina desirable for industrial applications [52]. However, an experiment conducted by Shackelford [53] has proven its Young's modulus experienced a decrease as temperature increases which is due to weakening of particles bond. Although ceramic offers several favourable properties for ore handling, ceramic is lacking in shock resistance ability that can be covered up with rubber. Due to their exceptional mechanical properties, alumina-based ceramics are abundantly used as a substitute material for applications such as pulley linings where wear resistance qualities are critical [54]. Ceramic laggings

are instrumental invention that brought about great benefit in engineering application. Main reasons to apply ceramic lagging on pulleys are to increase friction between belts and drive pulley lagging in changing conditions, to eliminate bodily slip between belts and drive pulley and to eliminate wear for driven or non-driven pulley. The typical properties of such alumina are flex strength (MPa) > 300, Impact resistance (MPa*mˆ0.5) > 4.5, average particle size distribution (μm) < 6.0, Vickers hardness (Hv5) > 950.

Before incorporating a ceramic as pulley lagging, it is essential to determine the percentage composition of alumina. Mechanical penetration of ceramic lagging into belt rubber can significantly increase friction force between pulley and belt. The increase in friction can eventually causes an increase in shear forces within belt which can hence be detrimental in ways such as ceramic tiles delaminate from rubber backing, rubber backing delaminates from drive pulley and belt bottom cover wear at accelerated rate. In essence, ceramic lagging is a good method in preventing belt slip, prolonging lagging life and increasing drive efficiency. Regardless, inappropriate composition and positioning of ceramic on pulley can also result in disastrous impact that may prove costlier. As such, combination of both ceramic and rubber lagging is generally utilised in most applications.

4.3 Ceramic-Rubber Lagging

For many years, ceramic-rubber laggings have been used as conveyor system's pulley liners [55]. Both ceramic and rubber has their particular downsides, ceramic has low shock resistance while rubber has lower hardness than ceramic [56]. Hence, lagging body of most belt conveyor pulley comprises of combination of rubber and ceramics [41]. It generally consists of long rubber substrate and numerous plate-like ceramic elements aligned in lateral and longitudinal direction and secured on the surface of said wide and long rubber to produces a desired thickness.

5 ASTM G65 Test

There are many wear test methods used for analysing thickness, strength, hardness, ductility, chemical composition, stress and wear resistance. Wear resistance being the priority in this project, ASTM G65-81 methods were used which is to rank the abrasion or scratch resistance of materials against silica sand [57]. American Society of Testing and Materials (ASTM) tests are a common tests to evaluate abrasive wear resistance using dry sand/rubber wheel apparatus [58]. It is a standard test method used to determine abrasive wear of materials by means of sand/wheel (coated with different linings) test. Such test rigs are commonly used in various industries when selecting materials for abrasive wear service such as using conveyer belts and pulleys [59].

Generally, ASTM G65 test involves loading a specimen against a rotating wheel coated with a lining while a flow of abrasive sand is directed at contact zone in the direction of wheel rotation. Test specimen is pressed against rotating wheel at a specified force by means of weights hooked onto lever arm. Duration of test, flow of abrasive sand and force applied on specimen is altered while keeping all other conditions constant through all tests and corresponding volume loss by specimen is identified as abrasion. Further chemical analysis on specimen can be done to determine chemical composition of specimen. Figure 2 illustrates standard set up of test rig based on ASTM G65 standard [60]. Different procedures, as mentioned in Table 1 require specific individual parameters to obtain desired results as illustrated in Table 2.

Specified abrasive is nominally 100% silica sand SiO_2, sieved to 50/70 mesh. Sand hopper with plastic tubing is also necessary to control sand flow rate to 300–400 g/min. Humidity should be under 0.5 wt% and sand should not be reused. To

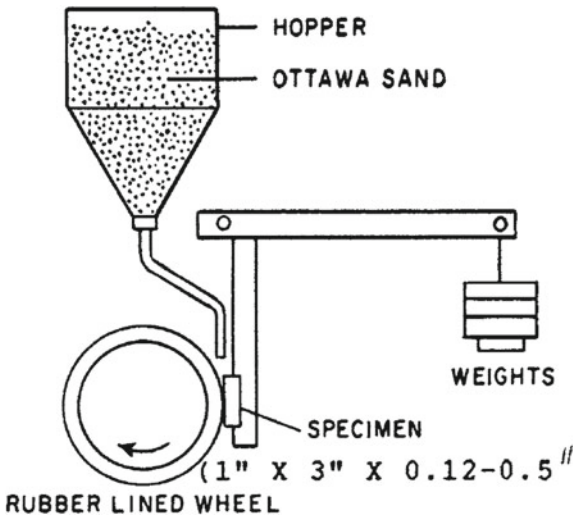

Fig. 2 ASTM G65 standard sand/rubber wheel test rig [60]

Table 1 Recommended procedures for ASTM G65

Procedure A	Test for ranking materials with low to extreme abrasion resistance
Procedure B	Suitable for ranking of medium and low abrasive resistant materials and it is a short-term variation of procedure A
Procedure C	Procedure use on thin coatings
Procedure D	Lighter load variation of procedure A used for materials of low abrasion resistance
Procedure E	Short term variation of procedure B that is useful to rank materials with medium or low abrasion resistance

Table 2 Procedure parameters [60]

Specified procedure	Force against specimen,[B] N (lb)	Wheel revolutions	Lineal Abrasion[A] m (ft)
A	130 (30)	6000	4309 (14,138)
B	130 (30)	2000	1436 (4,711)
C	130 (30)	100	71.8 (236)
D	45 (10.1)	6000	4309 (14,138)
E	130 (30)	1000	718 (2,360)

Table 3 Sieve analysis of silica sand [60]

U.S. sieve size	Sieve opening	% retained on sieve
40	425 μm (0.0165 in.)	None
50	300 μm (0.0117 in.)	5 max
70	212 μm (0.0083 in.)	95 min
100	150 μm (0.0059 in.)	None passing

accommodate speed, tube nozzle also must be designed to the specification. Details of sieve analysis of sand is shown in Table 3.

Wheel is another important component in test rig. It is made of steel disc of 228.60 mm and coated with 12.70 mm thick chlorobutyl rubber. It also has hole in the middle to fit drive shaft from motor. Test specimen is typically rectangular shape 25 × 75 mm and between 3.2 and 12.7 mm thick. This dimension may be varied in accordance to the need of user as long as the length and width is sufficient to show full length of wear scar as developed during the test. Test holder holding test specimen is attached to lever arm that is attached to the weights. ASTM G65 test is recommended for five procedures that are suitable for specific degrees of wear resistance or thicknesses of test material. Test requires a motor connected to wheel that will grind against specimen. The motor is required to deliver 200 ± 10 rpm and one experiment is expected to run up to 12000 revolutions. Main objective of ASTM G65 is to determine wear rate of a specimen. To do so, it is essential to calculate weight loss and to convert that in volume loss which eventually provide wear rate according to following equation:

$$Volume\ loss\left(\mathrm{mm}^3\right) = \frac{mass\ loss(\mathrm{g})}{density\left(\frac{\mathrm{g}}{\mathrm{cm}^3}\right)} \times 1000$$

$$Wear\ rate\left(\mathrm{mm}^3/\mathrm{min}\right) = \frac{Volume}{time}$$

6 Previous Studies

To further understand the project in hand and for aid in completion, numerous outcomes and results of previously conducted experiment by professionals were observed.

According to Molnar et al. [25], conveyor belt experience different wear on its rim area and centre area. Figure 3 depicts used conveyor belts where rims area experienced enormous cracks of 2 mm thick and up to 300 mm length while the centre area remained relatively smooth. However, thickness of rim area remained as it was (11 mm) while centre area's thickness has reduced to 2 mm from original 11 mm.

Molnar et al. [25] conducted an ASTM G65 studies on natural rubber and styrene butadiene rubber. Five rubber samples of different properties (Table 4) were tested accordingly by following standard test condition depicted in Table 5. However, rubber lined wheel utilised in this experiment has a higher hardness of 85 duro instead of recommended 60 ± 2 duro.

Result achieved from the test was not of any surprise. Generally, sample with higher hardness possesses a lower wear rate. Sample D with hardness of 60 shows a wear rate of 0.025 mm^3/min, while sample E being the lowest in terms of hardness possess highest wear rate of 0.051 mm^3/min. Wear rate of each sample/specimen is listed in Table 6.

Tangudom et al. [61] conducted a test where natural rubber and styrene butadiene were abraded against steel, fabric and concrete. This test also utilised BASi into SBR and NR, however this will not be the focus of this study. NR and SBR were

Fig. 3 Used conveyor belt [25] (with kind permission from Elsevier)

Table 4 Rubber samples properties [25] (with kind permission from Elsevier)

Sample number	Shore A hardness (dimensionless)	Tensile strength (MPa)	Tear strength (ISO 34-1 Method A) (MPa)	Max. abrasion according to data sheet (acc. ISO 4649) (mm^3)	Rubber base
A	55	18.3	11.8	120	SBR
B	58	19.9	17.7	90	NR/S BR/BR
C	59	22.9	14.0	120	NR/BR
D	60	21.9	20.7	70	KIR/BR
E	56	16.7	10.2	100	SBR

Table 5 Test condition [25] (with kind permission from Elsevier)

	ISO 4649	ASTIM G65M
Load	10 N	130 N
Sliding velocity	0.31 m/s	2.43 m/s
Covered distance	40 m	4309 m
Testing time	~2 min	30 min
Abrasive	Fixed corundum, edged; mesh 60; Moh's hardness: 9	Standard, round Ottawa sand; 212–300 µm; Moh's hardness: 7
Sample size	Ø 16 × 6 mm^2	70 × 25 × 6 mm^3

Table 6 Wear rate of each specimen

Sample number	Shore A hardness	Wear rate (mm^3/min)
A	55	0.042
B	58	0.032
C	59	0.036
D	60	0.025
E	56	0.051

abraded against steel, fabric, and concrete with 100 and 200 m sliding distance. Tables 7 and 8 show the wear rate of each rubber where NR has a significantly lower specific wear rate compared to SBR. This occurrence is well supported by Fig. 4 where the structure of SBR has more irregularities than NR.

Table 7 Wear rate of NR [61] (with kind permission from Elsevier)

Counterfaces	Sliding distance (m)	Specific wear rate (10^{-3} mm^3/N m)		Friction force (N)	
		BASi content		BASi content	
		0	15	0	15
Steel	100	0.05 ± 0.07	0.02 ± 0.03	34.0	35.5
	200	0.82 ± 0.25	0.38 ± 0.29		
Fabric	100	29.50 ± 1.38	53.05 ± 1.47	27.5	21.0
	200	31.37 ± 0.10	64.61 ± 0.98		
Concrete	100	18.56 ± 1.84	10.91 ± 1.64	18.0	19.0
	200	18.00 ± 3.10	18.07 ± 0.85		

Table 8 Wear rate of SBR [61] (with kind permission from Elsevier)

Counter faces	Sliding distance (m)	Specific wear rate (10^{-3} mm^3/N m)		Friction force (N)	
		BASi content		BASi content	
		0	15	0	15
Steel	100	0.12 ± 0.04	0.75 ± 0.50	50.0	43.0
	200	0.28 ± 0.15	1.97 ± 0.56		
Fabric	100	52.38 ± 6.00	60.31 ± 3.54	24.0	19.5
	200	49.52 ± 1.31	56.99 ± 1.40		
Concrete	100	10.67 ± 0.24	14.71 ± 1.03	20.5	15.5
	200	15.11 ± 0.51	16.71 ± 0.47		

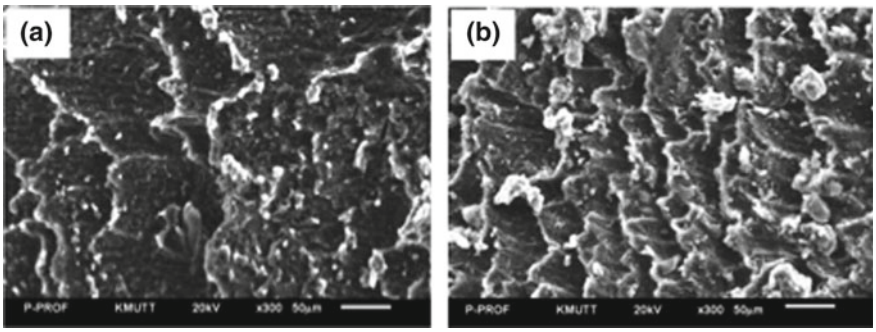

Fig. 4 SEM of worn **a** NR and **b** SBR [61] (with kind permission from Elsevier)

7 Experimental Procedure

Three tests (1, 2 and 3) were carried out in accordance to ASTM G65. The parameters are tabulated in Table 9. Each of the test was repeated three times to obtain an average (more reliable) value. ASTM G65 test rig as shown in Fig. 5 with rubber lining of 60 Shore A hardness and, width and diameter of 12.7 mm and 228 mm respectively, was used to conduct the tests.

AFS 50/70 silica sand is the standard abrasive used in ASTM G65 standard. However, to accommodate the test rig available, a similar super fine silica sand was used as abrasive in this experiment. As such, super fine white silica sand was

Table 9 Test parameters

Test parameters	Test 1: specimen A and B	Test 2: specimen C and D	Test 3: specimen E and F
Size (mm)	75 × 25 × 13		
Force (N)	80	130	180
Duration (min)	30	30	30
Temperature (°C)	18	18	19
Humidity (%)	67	59	56

Fig. 5 ASTM G65 Test Rig

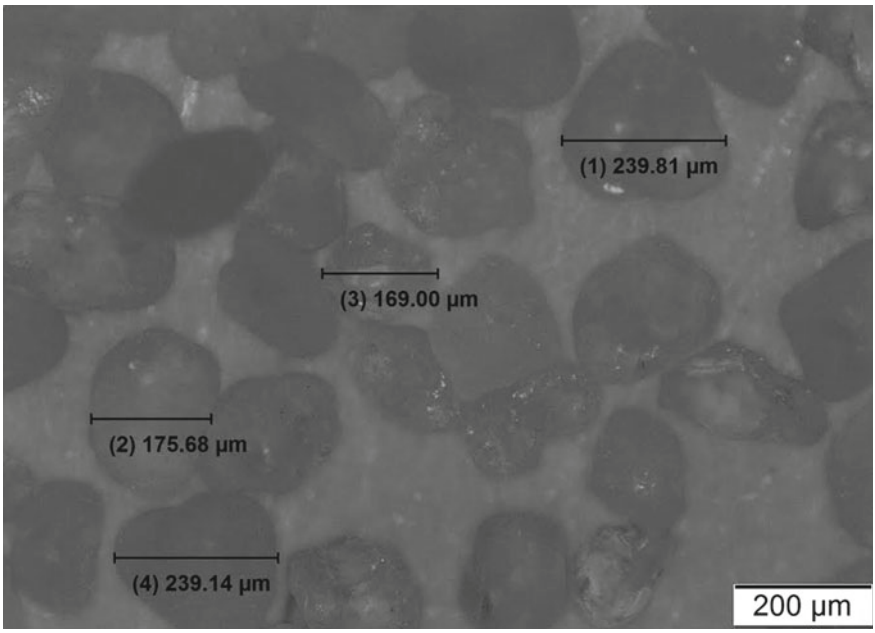

Fig. 6 Size distribution of white silica sand

purchased from Cook Industrial Minerals. Optical microscopic analysis was made and particle size prior to test is as shown in Fig. 6. Sieve analysis of sand is as illustrated in Table 10.

Ten ceramic specimens cut to required dimension of 75 × 25 × 13 mm. Composition of ceramic was of 90% alumina, 10% binding agents and with 1050 Vickers hardness. Ceramic specimens were polished respective according to method indicated by Kemet International Ltd using DIGIPREP 251 preparation system as shown in Fig. 7 according to polishing procedure is as indicated in Table 11.

The microscopic structure of ceramic specimen was analysed prior and after test using an optical microscope. Smooth surface of ceramic specimen after polishing and prior to test is as shown in Fig. 8.

Four natural rubber blocks of size 75 × 25 × 13 mm were purchased, and properties of rubber is listed in Table 12 while the image of rubber captured under microscope is shown in Fig. 9. Cleaning was performed by using only distilled water as any sort of polishing will likely to damage rubber.

Table 10 Sieve analysis of silica sand

Aperture (mm)	Retained (g)	Retained (%)	Cumulative on (%)	Cumulative passing (%)
1.000	0.000	0.000	0.000	100.000
0.850	0.000	0.000	0.000	100.000
0.710	0.040	0.030	0.030	97.970
0.600	0.140	0.100	0.130	99.870
0.500	0.380	0.280	0.410	99.590
0.425	1.190	0.880	1.290	98.710
0.300	50.160	37.010	38.300	61.700
0.212	49.180	36.280	74.580	25.420
0.150	25.95	19.150	93.730	6.270
0.106	6.670	4.920	98.650	1.350
0.075	1.310	0.970	99.620	0.380
0.053	0.049	0.360	99.980	0.020
PAN	0.030	0.020	100.000	0.000
Totals	135.540	100.000	100.000	0.000

Fig. 7 Polishing machine DIGIPREP 251

Table 11 Ceramic polishing procedure

Stage	Surface	Abrasive	Lubricant	Force (N)	Time (min)	Speed (rpm)	Relative rotation
Planar grinding	Diamond grinding disc	220 grit diamond grinding	Water	30	1	250	Contra
Fine grinding	Diamond grinding disc	1200 grit diamond grinding	Water	30	1	300	Contra
Pre-polishing	Fine grinding disc green	3 μ WP liquid diamond	GW2	15	4	150	Contra
Final polishing	MBL polishing cloth	1 μ WP liquid diamond	GW2	15	2	150	Contra

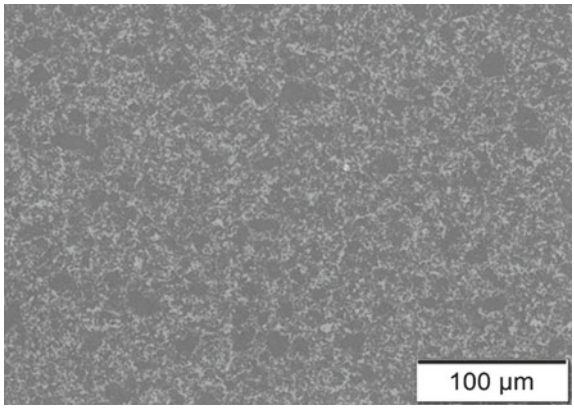

Fig. 8 Ceramic microstructure before test

Table 12 Natural rubber properties

Specific weight	1.13 g/cm^3
Hardness	60 ± 5 Shore A
Abrasion	90 mm^3
Resilience elasticity	45%

8 Results and Discussion

Effect of load on wear rate for three test conditions on six specimens (A–F) were obtained as illustrated in Table 13. Wears of ceramic and natural rubbers are compared in Table 14. Effect of load on ceramic wear is negligible for the range of load considered in this investigation. Ceramic possess an average wear rate of 0.255 mm^3/min

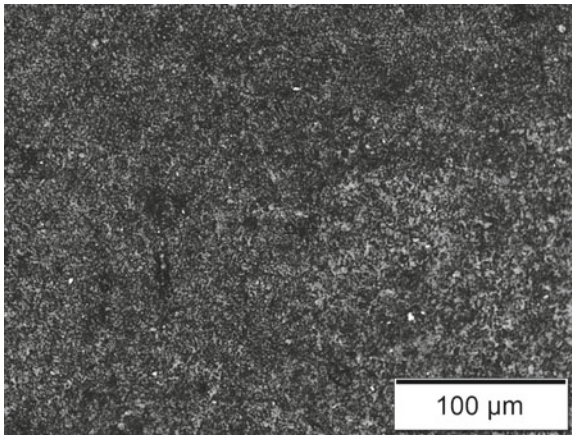

Fig. 9 Natural rubber surface before test

or volume loss of 7.8 mm^3 while rubber has an average 3.195 mm^3/min wear rate or 95.85 mm^3 volume loss. As expected, ceramic has a significantly lower wear rate compared to that of natural rubber under same test parameters.

As shown in Fig. 10, wear rate of ceramic experienced a significantly lower wear rate when compared to rubber. Due to ceramic's high porosity, wear debris was produced from cutting and fatigue wear mechanism which can also be observed from mass loss in Table 14. Furthermore, as shown in Fig. 11, grains have become irregular with minor pits due to sand particles rolling and wheel abrading against specimen.

As for natural rubber, wear is in some way different compared to conveyor belt studies conducted by Molnar et al. [25]. The rim area of specimen is smooth without any cracks (Fig. 12) while conveyor belt experienced cracks on its rim area. Furthermore, specimen's surface produced from ASTM G65 test conducted by Molnar et al. [25] possessed a smooth surface with high number of small pits instead of an uneven surface from this experiment (Fig. 13). Generally, worn natural rubber has a wavier surface compared to ceramic. Furthermore, tacky surface of rubber may have caused abrasion to be unsmooth during experiment, thus causing wear to be uneven. Furthermore, worn surface also contained some holes which was mainly caused by fatigue wear from the particles passing through.

It is established that sliding distance, applied load, and velocity influence the rubber wear rate. The loss of volume rises with the rise of these variables. Additionally, the mechanical properties, such as, tensile strength and hardness, of materials affect the rubbers' wear performance. Rise of those properties reduces the rate of wear. Furthermore, coefficient of friction and friction forces affect the mechanisms of wear based on the conditions of surface. Subsequently, lifespan of the belt can be enhanced by adjusting these factors.

The wear equation of Archard equation cannot forecast the wear of rubber because of extremely small Young's modulus and substantial dependency of material behaviours on temperature. Nevertheless, comparable equations are presented

Table 13 Effect of load on ceramic specimens

	Force on ceramic specimen								
	80 N			130 N			180 N		
	A	B	Avg.	C	D	Avg.	E	F	Avg.
Mass loss (mg)	27.5	26.4	27.0	30.3	26.1	28.2	23.9	32.6	28.3
Volume loss (mm^3)	7.8	7.5	7.65	8.6	7.4	8.0	6.8	9.2	8.0
Wear rate (mm^3/min)	0.26	0.25	0.26	0.29	0.25	0.27	0.23	0.31	0.27

Table 14 Wear rate of ceramic and natural rubber samples

	Ceramic			Natural Rubber		
	1st trial	2nd trial	Average	1st trial	2nd trial	Average
Mass loss (g)	0.0275	0.0264	0.0269	0.1024	0.1166	0.1095
Volume loss (mm^3)	7.8	7.5	7.65	89.6	102.1	95.85
Wear rate (mm^3/min)	0.26	0.25	0.255	2.99	3.40	3.195
Wear scar	Even			Uneven		

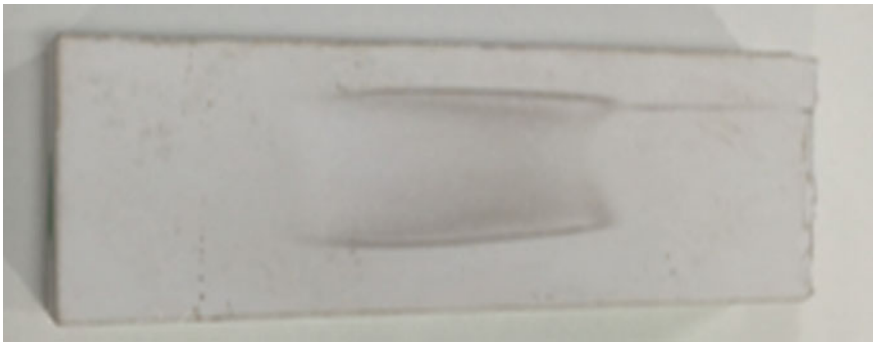

Fig. 10 Wear on ceramic sample after wear test

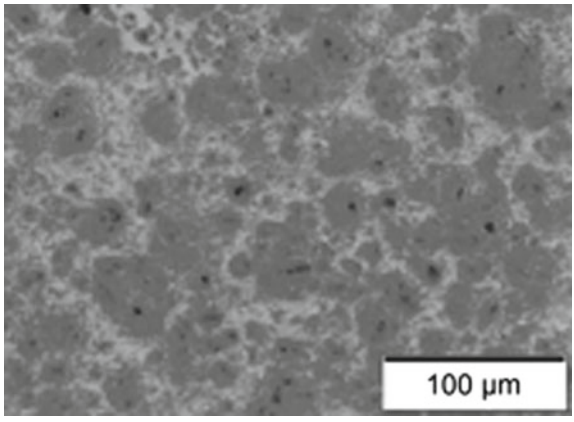

Fig. 11 Worn surface ceramic samples after wear test

by diverse investigators to formulate the wear performance of rubbers. In those formulations, simply one input variable for example, frictional work or normal force, is incorporated and numerous quantities are studied which affect the behaviours of abrader and rubber [62].

The leading mechanism of wear in a conveyor belt arrangement is 3-body abrasion wear. Nonetheless, maximum analyses about the mechanism of wear and effectual

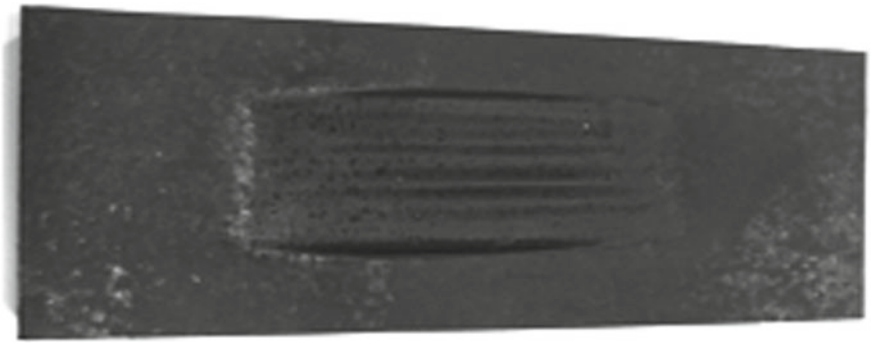

Fig. 12 Natural rubber sample after wear test

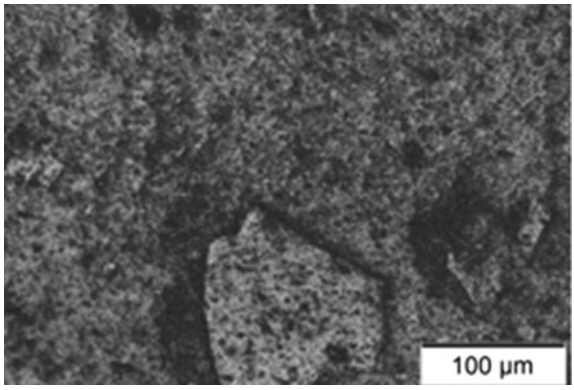

Fig. 13 Worn surface of natural rubber

variables on rubber wear are performed in 2-body environments. Accordingly, future studies are indispensable on 3-body wear of rubber for precise imitation of real service circumstance.

9 Conclusions

Conveyer system is an essential instrument particularly in a mining industry. Wear, particularly 3-body abrasive wear of pulley lining, is of great prominence in such instruments when applied in mining industries. As such, use of ASTM G65 rubber/sand test rig to replicate wear mechanism in studying three-body abrasive wears is beneficial in determining the parameters contributing to wear.

Results obtained showed a slight increase in average wear rate from 0.26 to 0.27 mm^3/min as load was increased from 80 to 130 N. However, wear rate stayed constant when the load was further increased to 180 N. Wear pattern of specimens

indicates a blacker spot on surface as compared to the surface prior to undergoing the test.

It was found that, natural rubber has a significantly higher wear rate compared to ceramic, 3.195 mm^3/min to 0.255 mm^3/min, respectively, for natural rubber and ceramic. However, this test was performed under 80 N of load instead of the standard 130 N. This was due to the concern in overwearing natural rubber specimen due to its low hardness compared to standard steel specimen. Wear pattern shown by both specimens also produced a dissimilar trend. Ceramic possessed a relatively smooth surface with small pits, whereas natural rubber possessed an uneven surface. It was observed that, wear pattern was generated from fatigue wear due to rolling of sand particles through specimens.

References

1. Yernberg, W.: Conveying and materials handling. Min. Eng. **60**(9), 39–40 (2008)
2. Finch, J.A.: Preface. In: Wills' Mineral Processing Technology, 8th edn. p. xi. Butterworth-Heinemann, Boston (2016)
3. Yardley, E.D.: Belt Conveying of Minerals. In: Stace, L.R. (ed.) Woodhead Publishing Series in Metals and Surface Engineering. Elsevier Science, Burlington (2008)
4. Hakami, F., Pramanik, A., Basak, A.K., Ridgway, N.: Elastomers' wear: comparison of theory with experiment. Tribol. Int. **135**, 46–54 (2019)
5. Kalina, D.: Rubber chemistry. In http://laroverket.com/wp-content/uploads/2015/03/rubber_chemistry.pdf (2007)
6. Intharapat, P., Nakason, C., Kongnoo, A.: Preparation of boric acid supported natural rubber as a reactive flame retardant and its properties. Polym. Degrad. Stab. **128**, 217–227 (2016). https://doi.org/10.1016/j.polymdegradstab.2016.03.004
7. Arayapranee, Wanvimon. 2012. *Rubber Abrasion Resistance* Edited by Marcin Adamiak: InTech
8. Hakami, F., Pramanik, A., Basak, A.K., Ridgway, N., Islam, M.N.: Effect of abrasive particle size on tribological behavior of elastomers. Proc. Inst. Mech. Eng. Part J J. Eng. Tribol.:1350650119864486 (2019)
9. Hakami, F., Pramanik, A., Islam, N., Basak, A., Ridgway, N.: Study of effective parameters on wear behavior of rubbers based on statistical methods. Polym. Adv. Technol. **30**(6), 1415–1426 (2019)
10. Shaffer, S.J. Tribology 101—introduction to the basics of tribology. Bruker TMT. https://www.bruker.com/fileadmin/user_upload/8-PDF-Docs/SurfaceAnalysis/TMT/Webinars/Tribology_101_Webinar-1_Intro_and_Basics_29-Jan-2013.pdf (2013). Accessed Oct 27 2013
11. Stachowiak, G.W., Batchelor, A.W.: 2—physical properties of lubricants. In: Engineering Tribology, 3rd edn., pp. 11–50. Butterworth-Heinemann, Burlington (2006)
12. Sethuramiah, A., Kumar, R.: Chapter 1—tribology in perspective. In: Modeling of Chemical Wear, pp. 1–23. Elsevier, Oxford (2016)
13. Mang, T.: Industrial Tribology: Tribosystems, Wear and Surface Engineering, Lubrication. In: Bobzin, K., Bartels, T. (eds.). Wiley-VCH, Weinheim (2010)
14. McKeen, L.W.: 2—Introduction to the tribology of plastics and elastomers. In: Fatigue and Tribological Properties of Plastics and Elastomers, 3rd edn. pp. 27–44. William Andrew Publishing (2016)
15. Stachowiak, G.W., Batchelor, A.W.: Engineering Tribology. In: [S.l] Butterworth-Heinemann. http://link.lis.curtin.edu.au/cgi-bin/gw?, http://www.sciencedirect.com/science/book/9780123970473 (2013)

16. Mang, T., Bobzin, K., Bartels, T.: Introduction. In: Industrial Tribology, pp. 1–7. Wiley-VCH Verlag GmbH & Co. KGaA (2010)
17. Adachi, K., Hutchings, I.M.: Wear-mode mapping for the micro-scale abrasion test. Wear **255**(1–6), 23–29 (2003). https://doi.org/10.1016/S0043-1648(03)00073-5
18. Kato, K., Adachi, K.: Modern Tribology Handbook. 2 vols, vol. 1 (2001)
19. Trezona, R.I., Allsopp, D.N., Hutchings, I.M.: Transitions between two-body and three-body abrasive wear: influence of test conditions in the microscale abrasive wear test. Wear **225**, 205–214 (1999). https://doi.org/10.1016/S0043-1648(98)00358-5
20. Ferreira, H., Leite, M.G.P.: A life cycle assessment study of iron ore mining. J Clean Prod **108**, Part A, 1081–1091 (2015). http://dx.doi.org/10.1016/j.jclepro.2015.05.140
21. Roumpos, C., Partsinevelos, P., Agioutantis, Z., Makantasis, K., Vlachou, A.: The optimal location of the distribution point of the belt conveyor system in continuous surface mining operations. Simul. Model. Pract. Theory **47**, 19–27 (2014). https://doi.org/10.1016/j.simpat.2014.04.006
22. Hou, Y., Xie, F., Huang, F.: Control strategy of disc braking systems for downward belt conveyors. Min. Sci. Technol. (China) **21**(4), 491–494 (2011). https://doi.org/10.1016/j.mstc.2011.06.005
23. Fedorko, G., Molnar, V., Marasova, D., Grincova, A., Dovica, M., Zivcak, J., Toth, T., Husakova, N.: Failure analysis of belt conveyor damage caused by the falling material. Part II: application of computer metrotomography. Eng. Fail. Anal. **34**, 431–442 (2013). https://doi.org/10.1016/j.engfailanal.2013.09.016
24. Zeng, F., Qing, W., Chu, X., Yue, Z.: Measurement of bulk material flow based on laser scanning technology for the energy efficiency improvement of belt conveyors. Measurement **75**, 230–243 (2015). https://doi.org/10.1016/j.measurement.2015.05.041
25. Molnar, W., Varga, M., Braun, P., Adam, K., Badisch, E.: Correlation of rubber based conveyor belt properties and abrasive wear rates under 2- and 3-body conditions. Wear **320**, 1–6 (2014). https://doi.org/10.1016/j.wear.2014.08.007
26. Brook, Norman. 1990. Mine Winding and Transport (Book Review)
27. Chandrasekaran, V.C.: 10—Beltings—transmission, conveyor, and v-belts. In: Essential Rubber Formulary, pp. 44–50. William Andrew Publishing, Norwich, NY (2007)
28. Commerce, Balkan Consult.: Rubber Conveyor Belts: Types of Conveyor Belts (2016)
29. Hossein, N., Saeed, C.C., Stichel, S.: Prediction of RCF and wear evolution of iron-ore locomotive wheels. Wear **338–339**, 62–72 (2015). https://doi.org/10.1016/j.wear.2015.05.015
30. Chowdhury, M.A., Khalil, M.K., Nuruzzaman, D.M., Rahaman, M.L.: The effect of sliding speed and normal load on friction and wear property of aluminum. Int J Mech Mech Eng **11**(01), 45–49 (2011)
31. Fedorko, G., Molnar, V., Marasova, D., Grincova, A., Dovica, M., Zivcak, J., Toth, T., Husakova, N.: Failure analysis of belt conveyor damage caused by the falling material. Part I: experimental measurements and regression models. Eng. Fail. Anal. **36**, 30–38 (2014). https://doi.org/10.1016/j.engfailanal.2013.09.017
32. Hernandez, S., Leiro, A., Ripoll, M.R., Vuorinen, E., Sundin, K.-G., Prakash, B.: High temperature three-body abrasive wear of 0.25C 1.42Si steel with carbide free bainitic (CFB) and martensitic microstructures. Wear **360–361**, 21–28 (2016). https://doi.org/10.1016/j.wear.2016.04.012
33. Gangadia, H., Sheth, S., Chauhan, P.: Design and modeling of special purpose equipment for shell-diaphragm welding in conveyor pulley. Proc. Technol. **14**, 497–504 (2014). https://doi.org/10.1016/j.protcy.2014.08.063
34. Ravikumar, M., Chattopadhyay, A.: Integral analysis of conveyor pulley using finite element method. Comput. Struct. **71**(3), 303–332 (1999). https://doi.org/10.1016/S0045-7949(98)00145-X
35. Chowdhury, S., Yedavalli, R.K.: Dynamics of belt-pulley-shaft systems. Mech. Mach. Theor. **98**, 199–215 (2016). https://doi.org/10.1016/j.mechmachtheory.2015.11.011
36. Yardley, E.D., Stace, L.R.: 4—Design of belt conveyors 2—hardware (Idlers, structure, pulleys, drives, tensioning devices, transfer points and belt cleaning). In: Belt Conveying of Minerals, pp. 44–70. Woodhead Publishing (2008)

37. PCI. Conveyor Pulley Selection Guide (2014)
38. Molnar, W., Nugent, S., Lindroos, M., Apostol, M., Varga, M.: Ballistic and numerical simulation of impacting goods on conveyor belt rubber. Polym. Testing **42**, 1–7 (2015). https://doi.org/10.1016/j.polymertesting.2014.12.001
39. Reibbelagtechnik, STS Friction.: Ceramic pulley linings for belt conveyor systems. Moeschter Group (2008)
40. Beninga, D.H.: Ceramic-rubber composites. Edited by 607 US Patent 3, 606: Coors Porcelain Company (1971)
41. Suginaka, M. Lagging body for belt conveyor pulley. Google Patents (1981)
42. Mark, J.E.: The Science and Technology of Rubber. In: Erman, B., Roland, M. (eds.) Science and Technology of Rubber, 4th edn. Elsevier Science, Burlington (2013)
43. bin Samsuri, A.: 3.33—Degradation of natural rubber and synthetic elastomers A2—Cottis, Bob. In: Graham, M., Lindsay. R., Lyon, S., Richardson, T., Scantlebury, D., Stott, H. (eds.) Shreir's Corrosion, pp. 2407–2438. Elsevier, Oxford (2010)
44. Gent, A.N.: Chapter 1—rubber elasticity: basic concepts and behavior. In: The science and technology of rubber, 4th edn., pp. 1–26. Academic Press, Boston (2013)
45. Saritha, A., Joseph, K.: Effect of nano clay on the constrained polymer volume of chlorobutyl rubber nanocomposites. Polym. Compos. **36**(11), 2135–2139 (2015). https://doi.org/10.1002/pc.23124
46. Zhang, H., Deng, J.X., Lian, Y.S.: Friction and wear behaviors of Al_2O_3 based ceramic tool materials at temperatures up to 800 °C. Appl. Mech. Mater. 148–149:908. http://dx.doi.org/10.4028/www.scientific.net/AMM.148-149.908 (2011)
47. Carter, C.B., Grant Norton, M.: Ceramic materials: science and engineering. In: Grant Norton, M., SpringerLink (eds.), 2nd edn. Springer, New York, NY (2013)
48. Olofsson, J.: Friction and Wear Mechanisms of Ceramic Surfaces, Uppsala University (2011)
49. Wachtman, J.B.: Mechanical properties of ceramics. In: Roger Cannon, W., John Matthewson, M., InterScience Wiley (eds.) 2nd edn. Wiley, Hoboken, N.J. (2009)
50. Shackelford, J.F., Doremus, R.H.: Ceramic and Glass Materials (2008)
51. Figiel, P., Rozmus, M., Smuk, B.: Properties of alumina ceramics obtained by conventional and non-conventional methods for sintering ceramics **48**(1) (2011)
52. Bansal, P., Upadhyay, L.: Effect of turning parameters on tool wear, surface roughness and metal removal rate of alumina reinforced aluminum composite. Proc. Technol. **23**, 304–310 (2016). https://doi.org/10.1016/j.protcy.2016.03.031
53. Shackelford, J.F.: Ceramic and Glass Materials: Structure, Properties and Processing. In: Doremus, R.H., SpringerLink (eds.). Springer US, Boston, MA (2008)
54. Auerkari, P.: Mechanical and physical properties of engineering alumina ceramics. Technical Research Centre of Finland ESPOO 1996 (1996)
55. Schimmoller, B.: Ceramic lagging cures belt slippage ills. Power Eng. **106**(10), 29–37 (2002)
56. Pomeroy, M.J.: Ceramic materials. In: Reference Module in Materials Science and Materials Engineering. Elsevier (2016)
57. Kennedy, D.M., Hashmi, M.S.J.: Methods of wear testing for advanced surface coatings and bulk materials. J. Mater. Process. Technol. **77**(1–3), 246–253 (1998). https://doi.org/10.1016/S0924-0136(97)00424-X
58. Doering, A., Danks, D., Mahmoud, S., Scott, J.: Evaluation of ASTM G65 abrasive—Spanning 13 years of sand. Wear **271**(9–10), 1252–1257 (2011). http://dx.doi.org/10.1016/j.wear.2011.01.051
59. Yanes, R.E., Hernandez, L.N., Morera, O.Z., Olivier, N.C., Neto, A.F.: Design and fabrication of a machine for test in abrasive wearing according to ASTM G65 standard. Am. J. Mater. Sci. Appl. **2**(5), 86–90 (2014)
60. International, ASTM.: Standard test method for measuring abrasion using the dry sand/rubber wheel apparatus (2010)
61. Tangudom, P., Thongsang, S., Sombatsompop, N.: Cure and mechanical properties and abrasive wear behavior of natural rubber, styrene–butadiene rubber and their blends reinforced with silica hybrid fillers. Mater. Des. **53**, 856–864 (2014). https://doi.org/10.1016/j.matdes.2013.07.024

62. Hakami, F., Pramanik, A., Ridgway, N., Basak, A.K.: Developments of rubber material wear in conveyer belt system. Tribol. Int. 111:148–158 (2017)
63. ExxonMobil. Butyl Rubber. Accessed 5 May. http://www.exxonmobilchemical.com/Chem-English/brands/butyl-rubber-exxon-chlorobutyl.aspx?ln=productsservices
64. Roulunds. Conveyor Belt. Accessed 6 May 2016

Surface Characteristics When Solid State Welding of Aluminium Alloys to Magnesium Alloys

P. Shenbaga Velu, N. J. Vignesh, and N. Rajesh Jesudoss Hynes

Abstract In the past two decades, there has been an ever-increasing demand for solid-state welding of dissimilar materials. This type of solid-state welding technique is gaining prominence in various disciplines but more importantly in naval, marine, aerospace and military applications. Most of the leading car manufactures today are exploring the possibilities of joining magnesium with aluminium, via solid-state welding process. In the present scenario these techniques are applicable for automotive applications like transmission cases and oil pans. In this work, the different types of solid-state welding techniques that were used for joining of aluminium alloys with magnesium alloys are reviewed from different perceptions. One of the important issues that is faced during joining of these dissimilar materials, is the formation of intermetallic compounds (IMCs) at the welded interface. The work also highlights the influence of various process parameters, structural morphology, intermetallic compound formation and variations in mechanical properties. Some of the important Solid-state welding processes that are elucidated here includes: friction welding, friction stir welding, friction stir spot welding, diffusion welding and third body welding. The above said techniques are carefully analysed for the formation of a satisfactory and quality sound aluminium-magnesium joints. In the overview, it can be summarized that friction-based joining processes have great potential to obtain sound Al–Mg joints. The amount of frictional heat generated at the surface of the contact helps to decide the type and volume fraction of IMCs that are subsequently affecting the mechanical properties of the joints. The joint properties can be enhanced by optimizing the process parameters.

P. Shenbaga Velu
Department of Mechanical Engineering, PSR Engineering College, Sivakasi, India

N. J. Vignesh · N. Rajesh Jesudoss Hynes (✉)
Department of Mechanical Engineering, Mepco Schlenk Engineering College, Sivakasi, India
e-mail: findhynes@yahoo.co.in

K. Gupta (ed.), *Surface Engineering of Modern Materials*, Engineering Materials,
https://doi.org/10.1007/978-3-030-43232-4_4

1 Introduction

1.1 Background of Dissimilar Materials

The accelerated demand for the improved mechanical and other properties has motivated scientists to do research and development to explore lightweight materials and alloys, as they possess superior qualities such as high specific strength, low weight, and corrosion resistance etc. Magnesium is considered to be the lightest of all the metals and is one of the most popularly used materials in industries. It is around 33% lighter than aluminium and about 75% lighter than steel. It is having a density of 1.74 g/m^3 [1]. The crystalline structure of Magnesium metal is having a hexagonally packed closed structure. This structure helps in resisting the slip of the atoms along the parallel basal planes. The plastic deformation of magnesium metal cannot be carried out at room temperature, because the rate of work hardening is high and also it has lower ductility. The forming operation in a magnesium alloy usually takes place above 226 °C. At elevated temperatures in the range between 343 and 510 °C, the slip process takes place easily. Other consequences of the HCP structure arising during the deformation is the existence of anisotropy in the cold-formed sheets [2–5].

The advantages of being extremely light alloys helps the magnesium alloys to exhibit good castability, hot formability and recyclability [1, 5]. Therefore, the combination of these Al and Mg alloys in a single entity will result in even more weight savings leading to advanced applications. The purpose of choosing Al/Mg alloy hybrid structures in this book chapter is that, they are having greater potential applications in automobile and aerospace fields.

The automobile industries highly reliant on Aluminium and its alloys due to the following reasons. They are lower density, good corrosion resistance, good thermal and electrical conductivity, high specific strength, good workability, intrinsic recyclability and good looking and attractive appearance [1–4]. Being the extreme lightest metal, magnesium and its alloys have excellent specific strength, excellent sound damping capabilities, good castability, hot formability, good electromagnetic interference shielding, and recyclability. The power input required for welding of magnesium is very low due to its excellent specific physical properties. Magnesium and its alloys have a very higher affinity to oxygen molecules forming oxides. Hence, the liquid molten weld has to be prevented from such an environment by using shielding gases. Further, in order to increase the complexity of the oxidation process, this molten magnesium, at the joint interface of the welds, forms a thermodynamically stable natural oxide layer on its surface, which becomes an inherent deficiency during the joining process.

Some of the applications are property specific, in a sense, it is capable of being exhibited by certain metals. For example, in case of Magnesium, it has damping capacity and Aluminium has good creep resistance. Combination of both these metals are expected to be used in industrial applications also in the near future. When these two components are combined together in one hybrid structure, then it would result in even more applications with desirable weight savings. In order to meet the demands

of making Al/Mg dissimilar joints, there is a pressing need for a technology which would help in developing these joints. In addition to this, the problems that are associated with joining these materials should also be resolved.

1.2 Current Research Status

As per the research findings, it has been noted that, the joint strength of the Al and Mg joints are affected due to the formation of hard and brittle Intermetallic Compounds (IMCs). Figure 1 shows the binary phase diagram of an Al–Mg joint. It can be seen that; it results in the formation of intermetallic compounds such as Mg_2Al_3 and $Mg_{17}Al_{12}$ after solidifying.

The formation of intermetallic layer in between the Mg/Al joints gives rise to technological difficulties i.e. IMCs as shown in Fig. 1. Therefore, the crucial thing to improve the strength of the joints formed is to eliminate or reduce the formation of IMCs in between them. There are primarily three approaches or methods used to reduce the formation of these IMCs. In the first method, the IMCs are reduced by maintaining the interface temperature of the welding process to a lower value. Solid state welding techniques which require low welding temperatures such as friction stir welding and diffusion bonding are capable of achieving higher strength. In the second method, the variety and distribution of the IMCs were controlled. This helps to prevent the joint strength degradation in fusion welding technique. In this approach,

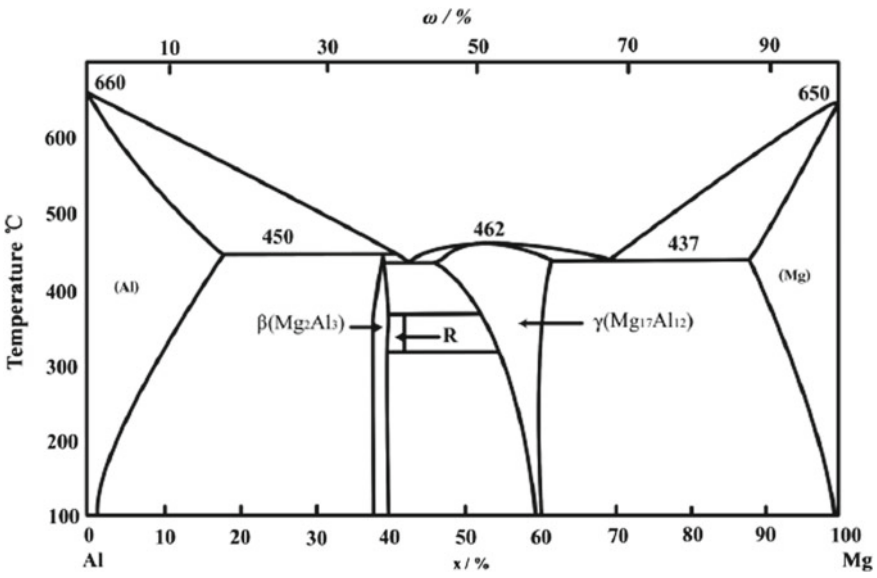

Fig. 1 Study on the microstructure and liquid–solid correlation of Al–Mg alloys [6]

during certain periods of time, filler metals are alloyed to the weld seam in order to reduce the formation of IMCs in techniques such as arc welding, laser welding and laser-arc hybrid welding. Techniques such as friction stir spot adhesive bonding and laser weld bonding were used to join Mg and Al. The mechanical structure and the microstructure of the Al/Mg welds could be improved by the stirring effect on the weld pool and the adhesive. In the third method, the IMCs could be reduced by having short reaction time and lower energy during the welds. Techniques such as ultrasonic welding, electromagnetic impact welding, resistance spot welding and explosive welding follow this type of approach in reducing the IMCs. By following any one of the above said methodologies, the Mg/Al joint strength has been significantly improved. Some of the techniques are very useful for joining Mg and Al alloy in the work place.

1.3 Need for Dissimilar Joints

Table 1 depicts the applications areas for various dissimilar joints.

Table 1 Dissimilar joints and applications

S. no	Previous research works	Applications
1.	Stainless steel/Al (Sahin et al. 2010) [7]	Energy saving
2.	Stainless steel/Cu (Sahin et al. 2010) [7]	Electrical conductors, blades, cooking kettles
3.	Al/Cu (Sahin et al. 2010) [7]	Replacing steel in electricity supply to reduce cost
4.	Brass/Cu (Naval Brass) (Sassani et al. 1988) [8]	X-ray machines, radio aerials, electric cables
5.	Bronze/1025 Steel (Cu interlayer) (Sassani et al. 1988) [8]	Bourdon springs, electric probes, heat exchangers
6.	Titanium/Ni (Sassani et al. 1988) [8]	Aerospace, development of bone structures, gas bottles
7.	Al/Lithium (Cu) Thermal Processing & Tempering (Cindie Giummarral et al. 2007) [8]	Aerospace industry (sheet and plate for fuselage, lower wing)
8.	Aluminum/Mild Steel (Rajesh Jesudoss Hynes et al. 2014) [9]	Oil and gas industries
9.	Mg–Al–Si, Magnesium MRI153M alloy and from aluminium A380 alloy (Blawert et al. 2004) [10]	Automotive applications like transmission cases, oil pan

1.4 Al/Mg Alloy Applications and Issues in Their Joining

Research findings show that, in the current scenario, Magnesium is expected to play a significant role in automobile applications. But, the efforts to completely replace aluminium and steel components is still under growing stage. This is due to the problems associated with galvanic corrosion etc. with Mg alloys. But in some cases, there is demand for replacing the aluminium alloys and steel with magnesium alloys. This helps increasing the opportunity for producing Magnesium/Aluminium and Mg/steel joints. The application areas of Mg alloys and thus the Mg alloy and Al alloy joints in automotives are shown in Fig. 2. Some of the important major challenges faced by leading car manufacturers are as described below (Table 2).

Hence, the reduction in the corrosion characteristics and also improving the mechanical behaviour of the Mg/Al and Mg/steel joints helps to find this material combination a permanent place in the automobile field.

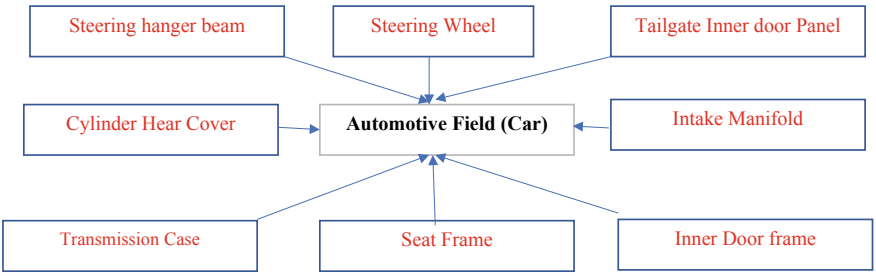

Fig. 2 Mg alloy used in automotive field

Table 2 Challenges faced by car manufacturers

S. no	Global car manufactures	Changes to be made in future cars	Challenges
1.	General Motors, Porsche	Magnesium wheels	High volume cost, low strength and corrosion of joints
2.	BMW	Magnesium housing for the intake manifold	High temperature
3.	Volks wagon	Engine blocks	Coolant reacts with Mg leading to corrosion and reduction in strength of joints
4.	Ford F-150	Cam covers	Good dampening characteristics
5.	Rolls-Royce Phantom	Interior components such as Instrument panels, steering and seat structures	Corrosion problem and strength of joints

2 Solid State Welding

2.1 Friction Welding

One of the novel techniques used for joining of dissimilar materials is Friction welding. The technique is well suited for joining similar materials too, but the original fact behind its development was to join dissimilar materials, because similar materials are joined more easily by conventional welding techniques itself. The two dissimilar materials that are used here, are fixed rigidly in their respective collects provided in the friction welding machine. Out of these two specimens being held, one of the specimens is made to rotate at a fixed angular velocity, whereas the other specimen is being held rigidly without any rotation. Once the specimens are fixed in their respective collets, then the friction welding machine is started and it makes the rotating collet to rotate at the desired speed. On the other hand, the non-rotating collet is used for application of axial force and it is the collect which moves towards the rotating collet in order to make direct frictional contact with the other specimen [7]. Once the desired axial pressure is applied on to the stationary collet, the joining process starts taking place. Plastic deformation takes place as the material reaches the softening temperature when there exists relative motion and friction in between the two components. When there is sufficient pre-set displacement and burn-off length reached during the friction welding process, then the rotation of the spindle is stopped and the axial pressure is increased on the non-rotating member. This helps in achieving superior quality welds. Some of the important and crucial parameters that are likely to affect the friction welding process includes friction time, friction force, displacement and temperature. By varying these process parameters, their effects on the friction welded components could be determined. Figure 3 illustrates the various stages of friction welding while making dissimilar joints.

2.1.1 Phases of Friction Welding

The important phases that are taking place in a friction welding process includes the following:

First Friction Phase
During this first phase, the collet is made to rotate at the desired speed. Then both the specimens are made to contact with each other by moving the stationary collet having one of the components held in it in the direction of the rotating collet having the other component. This helps in applying the force necessary at the area of the weld. At this stage, the preheating of the weld interface takes place. But there is not much displacement at this stage, because the components have just started to reach their melting temperatures. The duration of the time is controlled as given in [11]. This first phase helps in burning out all the light oxides that existing in the interface of the weld.

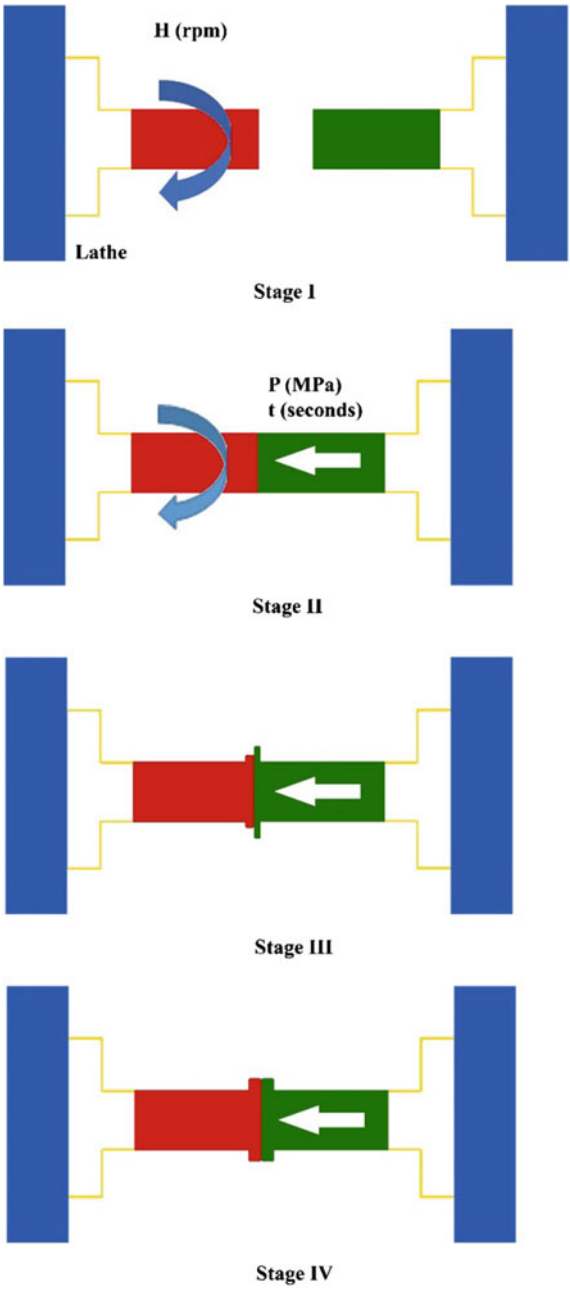

Fig. 3 Stages of friction welding process during dissimilar joints

Second Friction Phase
In the second phase of this welding process, the loss in material is controlled as there is reduction in the length of the specimens during the welding process. When taking the entire displacement of the material from the point of contact of the two materials, about 2/3 of the displacement from their actual position, takes place in this phase alone as reported by [12]. There are some three methods available for reducing this loss of material length during the friction welding process. It is achieved by time and constant axial distance.

Third Forge Phase
This final phase marks the end of the rotational moment of the spindle and the application of pressure is increased further so as to produce a strong weld and then the specimen is allowed to cool. It is the second stage of material displacement by which around 1/3 of the total displacement takes place as reported by [12]. This forge phase is mainly dependent upon the amount of heat generated during the second friction phase and the amount of final pressure applied. This forging phase can be controlled by varying the amount of forging force and forging time.

2.1.2 Friction Welding Process Parameters

The important parameters that are affecting the rate of friction welding include friction pressure (pressure required to attain the heat source for joining), rotational speed (the speed at which spindle is rotated), forging pressure (the axial pressure which is applied on the stationary component once rotation of the spindle is stopped), burn-off length (loss of material length during friction welding), friction time (the time taken to friction weld the specimens), forging time (the time up to which forging of the two metal specimens takes place) and the effect of joint design.

Rotational Speed
The mechanical properties of the AISI 4340 steel which is welded using friction welding technique has been studied by varying the rotational speed [11]. In most of the cases, higher rotational speeds are preferred for carrying out the welds. When quench-harden able steels are used, then proper friction pressure and time should be used in order to prevent the weld zone from the effect of excess heating otherwise it leads to possible cracks. Through experiments, it has been found that the formation of brittle intermetallic compounds could be reduced when the speed of rotation is lower.

Friction Pressure
Researchers studied the effect of friction pressure on mechanical properties of friction welded dissimilar materials [13]. They found that, increasing the friction pressure will result in the increase in tensile strength up to a certain value and then the value decreases slightly with further increase in forging pressure. They also reported that,

to achieve the desired or better mechanical properties, a friction pressure of 135 MPa is required. Hardness at the central layer increases when friction pressure increases.

Burn-off Length
Burn-off length plays an important role in the bonding mechanism and mechanical properties of dissimilar joints [14]. It was investigated that increasing the burn off length, will help to attain better mechanical strength of the welded joints and also to evaluate the joint integrity of dissimilar materials.

Forging Pressure
Forging pressure plays another major role in controlling the deformation and excess heat generation due to plastic deformation. Generally, the value of forging pressure should be kept at optimum, because high forging pressure will result in excess deformation and adverse orientation of the parent material.

Friction Time
In order to reduce the material loss and to increase the productivity, the friction time should be increased only up to a certain limit. On the other hand, lower friction time will cause uneven heating that leads to oxide formation. As a result of oxide formation, it may result in the formation of unbound zone at the joint interface [15]. Observed that, the value of tensile strength increases with the increase of friction time up to a certain limit and then decreases with further increase in friction time.

Forging Time
Khan and Ahmed (2011) [16] described that, severe plastic deformation occurs when the forging time is higher. But on the other hand, lower forging time will result in the formation of ineffective joints at the weld interface and attain insufficient removal of non-metallic insertions.

2.1.3 Surface Characterization of al/Mg Friction Weld Joint

The surfaces of welding region of both aluminium and magnesium samples were ground to ensure the smooth finish before welding. Similarly, the edges of welding surface were chamfered to make it perfect for welding. Morphological images of welded aluminium alloy (AA6061-T6) and magnesium alloy (AZ31B) joints are given in Fig. 4 (a) (aluminium alloy) and (b) (magnesium alloy).

Macrostructure

The macro level structural studies were executed at the interfacial part of welds and heat influenced region. These assessments revealed that rotational speed generates less temperature changes at the core or central region of interfacial zone. However, rotational speed induces maximum temperature at the outer region of the

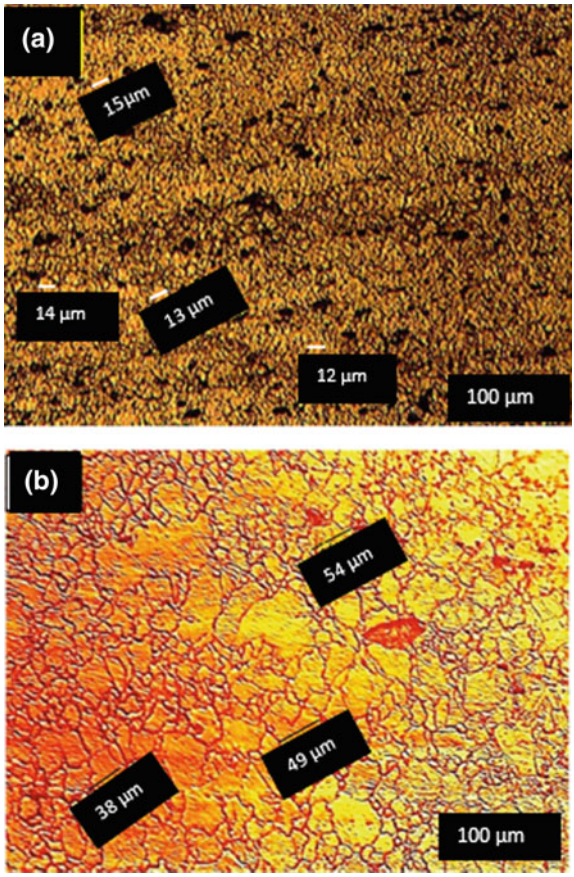

Fig. 4 Microstructure of parent materials. **a** Aluminium, **b** magnesium alloy

specimen. Structural transformations is experienced at the welds due to these heat inducement. Moreover, the duration of friction is also a decisive factor as far as the quality of weld is concerned. The irregularity at the welded region and burn-off-length has close relationship with the friction time. The excessive or limited duration of friction disturbs to achieve structurally defect free weld. The sacrifice of metal (forged) is higher at the magnesium alloy portion than aluminium alloy side. This loss occurs due to the changes (reduction) in the yield strength of magnesium alloy in comparison to aluminium alloy for the same temperature environment. Thermal conductivity difference between these two distinct alloys is an additional factor for differences where aluminium alloy conducts heat faster than magnesium alloy. Consequently, uneven temperature distribution occurs at the welded region and high plastic deformation is contributed by magnesium alloy. This leads to metal forging at the weld interface and asymmetric weld is generated. Figure 5 exhibits the micro level structural assessment of the Fully-dynamic-plasticized zone (FDPZ), Thermo-mechanical-affected zone (TMAZ) and heat-affected zone (HAZ) of the magnesium

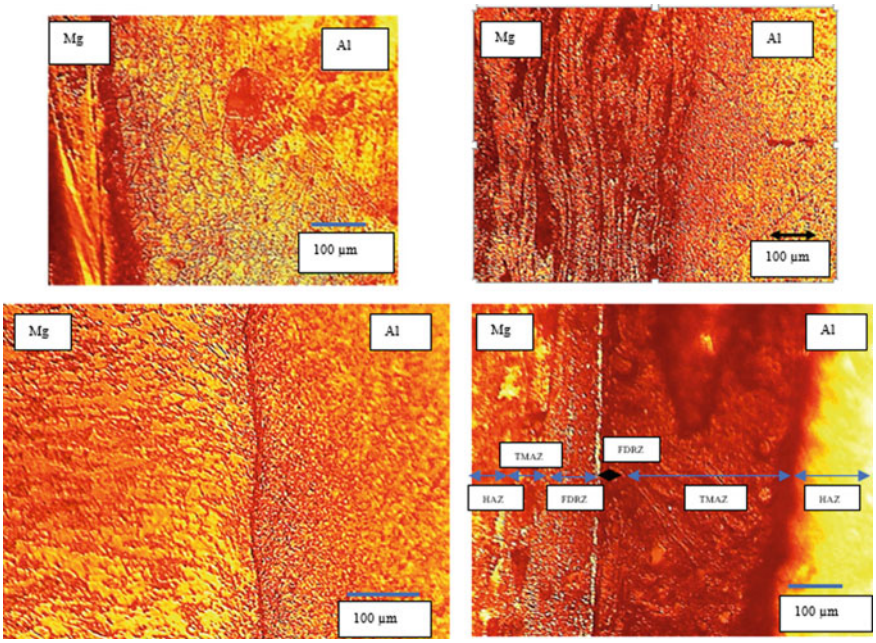

Fig. 5 Different zones of aluminium/magnesium joints using friction welding process

alloy region. Fully-dynamic-plasticized zone displays the generation of fine grains due to the frictional heat inducement and axial shortening. Eutectic particles (magnesium solution) precipitate at the friction zone. Mixed experience is observed at the thermo-mechanical-affected zone as both coarser and finer grains are present. Heat influenced zone behaves differently with large quantum of grains available at the magnesium alloy part in comparison to the rest of the region (HAZ). Similar proceedings are experienced at micro level of aluminum alloy part. Since, fully-dynamic-plasticized region possesses negligible width, thermo-mechanical-affected zone is forced little to rely on the grain size (second phase) of the alloy. However, this dependence doesn't disturb the dominance of size, dissemination of strengthening precipitates and volume fraction.

2.2 Friction Stir Welding

Friction stir welding is a solid-state welding process having a non-consumable rotating tool. This tool has a pin and shoulder which is allowed to rotate in between the abutting edges of the two specimens and are made to move along the line of the joint [17]. The side along which the tool moves along the direction of welding is said to be called as advancing side and the other side where the direction is opposite

to the rotational axis of the tool is known as retreating side [18]. The probe/pin is an important device which is protruding from the base of the tool or the shoulder. This pin has a length which is less than the thickness of the workpiece. The plastic deformation of the material starts taking place as soon as there is frictional heating in between the tool and the workpiece [19]. Because of this, the workpiece material that is around the pin starts softening due to the localized heating. There occurs the displacement of the softened workpiece material from the front end of the tool to the back end as there is a combination of the tool rotational on linear translation [20]. When cooling takes place, then a good quality solid state welded joint is produced.

2.2.1 Mechanism of Formation of Intermetallic Compounds

Weldment is formed as a result of the combined effect of tool rotation and softening of the material as the tool moves. This method was initially developed for welding of aluminium alloys [21]. This process was also described as a non-weldable technique due to the rapid solidification taking place in the fusion zone and the microstructure formed. This method of welding has been applied to a number of metals and alloys from the time of its development. This method has also been described as a feasible technique for joining magnesium alloys by Somasekharan [22].

The joints produced by FSW of Mg alloys are having very good characteristics. Some of them are high fatigue resistance, high joint strength, less distortion, cheaper as there is no need for any consumables and there is no loss of alloying elements during the process [23, 24]. The quality of the welds is based on optimizing certain process parameters such as tool shape, jig rotational speed, tool speed, and joint configuration.

2.2.2 Different Zones Formed During FSW Process

The following discussion deals with the formation of distinct zones during the FSW process. Four different kinds of weld zones are formed during the FSW process as compared to the traditional welding methods which is shown in the Fig. 6. The various zones that are present include; stirring zone (SZ), thermo-mechanical affected zone (TMAZ), heat affected zone (HAZ), and base metal (BM) [25, 26]. FSW is capable of joining Mg with a shear strength of 66–410 MPa and their hardness values are in the range from 50 to 110 HVN in Vickers Hardness scale [25, 27]. The efficiency of the joints produced are in the range of 60–95% when compared to the base metal alloy as reported by Singh et al. [22]. Due to the formation of the Intermetallic Compounds at the joint interface of the weld, there exists some difference between the hardness measured at the base metal and the centre of the weld. These similarities were documented by other researchers also, who carried out the FSW of other Mg alloys such as MgAZ31 [28, 29] and MgAZ31B [28–30] and dissimilar joint of Al6061/MgAZ31B [31, 32]. Mohammadi et al. [31] in his research findings proved

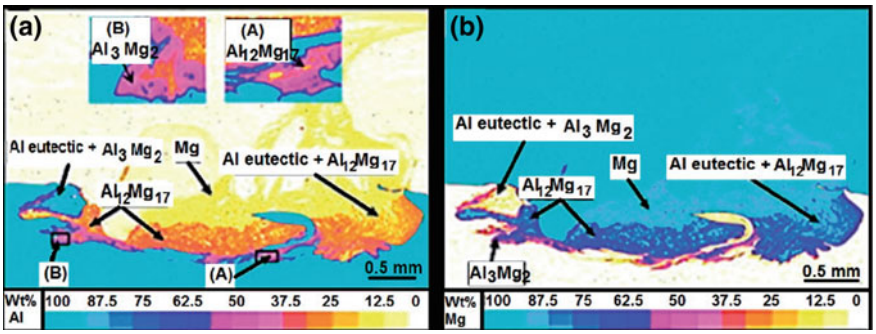

Fig. 6 EPMA results of the FSW region of the sample welded by using a weld-pitch ratio of 1400/40 r/mm in the cross-section perpendicular to the tool transverse direction. Element distribution: **a** Al and **b** Mg [33]

that the formation of intermetallic compounds during the FSW of dissimilar materials is reduced.

A recrystallized fine-grained microstructure was formed in the stir/nugget zone when there occurs frictional heating and plastic deformation during friction stir welding process. In certain circumstances, it is found that there is formation of onion like ring structure in the nugget zone [34]. In the regions of the nugget/stir zone, the smaller recrystallized grains are found. These grains contain higher density of sub-grains, sub-boundaries and dislocations. The interface is quite dispersed on the retarding side of the tool but is very sharp on the advancing side of the tool in between the recrystallized nugget/stir zone and the base metal. The following Table presents the grain sizes reported in various research findings with their substrate materials, tool geometries and welding parameters used to weld various grades of the magnesium alloys [35] (Table 3).

In the regions between the parent material and the nugget/stir zone (SZ), there is formation of a new zone namely thermo-mechanically affected zone (TMAZ) which is a transition zone. This TMAZ zone actually experiences both temperature effects and deformation during the FSW process [37–39]. It has been found that, this TMAZ is the highly deformed structural zone found in the microstructure. Along the regions of the stirred zone, the deformed grains of the parent metal were found elongated in an upward flowing pattern. In this region, the recrystallization of the grains does not occur because of the insufficient deformation strain.

Kouadri Henni et al. [40] in his research work reported that the weld zone is composed of two parts namely: (i) Transition region (TMAZ) and (ii) Stir zone. Magnesium grains in the TMAZ zone is found to have an elongated shape because of the plastic deformation during FSW (Fig. 7). In this TMAZ zone, the researchers are able to find a deformed grain structure consisting of sub-grains just outside the stir zone. When the distance from the stir zone is decreased, the deformation of the grains starts increasing. Also, when comparing the grain size, they are coarser in the

Table 3 Substrate materials, tool geometries, welding parameters and grain size of FSW Mg alloys [36]

Workpiece material	Plate thickness (mm)	Tool geometry	Rotational speed	Welding speed	Grain size (μm)
AZ31 Mg alloy	8	Conical threaded	800–1600 rpm	120 mm/min	6–20
AZ31 Mg alloy	6	Cylindrical threaded	1600 rpm	600 mm/min	9.8
AZ31B-H24 Mg alloy	2	Left-hand thread and right-hand thread	1000–2000 rpm	5–30 mm/s	5.4 ± 2.2
AZ31B-O Mg alloy	5	Left hand threaded tool pin	1200–1950 rpm	40–60 mm/min	9
AZ91 Mg alloy	5	Cylindrical, triangle, square	710–1400 rpm	12.5–63 mm/min	9–32
AZ91D Mg alloy	3	Tapered cylindrical threaded	1025–1525 rpm	25–75 mm/min	7–21
AZ91D Mg alloy	4		115–377 rad/s	32 and 187 mm/min	7–19

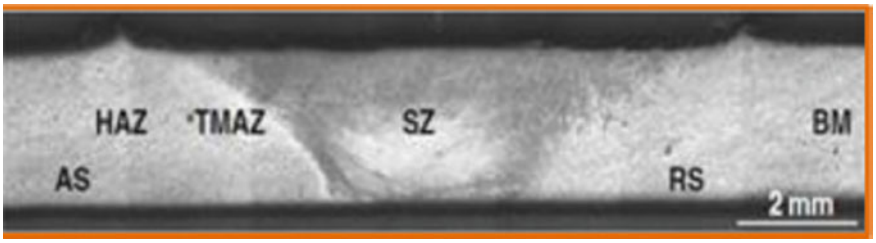

Fig. 7 Overview of the microstructural zones in FSW joint AZ31 [36]

TMAZ is coarser than in the stirred zone. This follows a grain size gradient pattern. This is due to the insufficient thermal exposure and deformation.

Next to the TMAZ, there is a zone called as heat-affected zone (HAZ). This zone does not undergo any plastic deformation but it experiences a thermal cycle. This has been confirmed in the research finding as reported by Esparza et al. [41]. It is a zone which is not stirred by the pin nor rubbed by the shoulder but was influenced by the heat of welding, leading to some microstructural changes.

2.2.3 Mechanical Properties

The weld strength enhances at high rotational speed of tool and low joining speed. However, Lim et al. [36, 42] explored that tensile strength of magnesium alloy (AZ31B) is least influenced by process parameters after friction stir welding. Lee et al. carried out the optimization studies of process parameters to friction stir weld the magnesium alloy (AZ91D) [43]. The rotational speed range of 1240–1750 rpm and travelling speed of 50 mm/min enhanced tensile properties of the weld than the base material. Padmanabham et al. [44] investigated the effect of friction tool on magnesium alloy (AZ31B) through friction stir welding. Chowdhury et al. [45] specified the strength properties and ductile nature of friction stir welded magnesium alloy (AZ31B-H24). The welding process reduced the strain rates and weld efficiency was achieved in the range of 75–80%. The reduction of strain rate has no significance on yield strength as well as ultimate tensile strength of the weld. The presence of aluminium as constituent decides the hardness of magnesium alloy. Additionally, the precipitated particles also influences the hardness of the materials irrespective of grain sizes. The hardness moved slowly towards around 63 HV from 73 HV at the central region of stir zone via heat-affected zone and thermo-mechanical-affected zone. The lowest possible hardness at stir zone was the reason behind the grain growth and easy recrystallization and the low hardness occurred due to high grain size. Park et al. [46] registered about the even distribution of harness across different zones after friction stir welding of magnesium alloy (AZ61). Singarapu et al. [47] disclosed that the micro-hardness can be enhanced through increasing the rotational speed of the tool to particular extend only, beyond which micro-hardness is lowered because of extensive heat generation. This heat build-up softens the material through disturbing the strengthened precipitates and/or coarsening. Consequently, low micro-hardness is observed. They expressed two reasons for the hardness enhancement at the stir zone. The finer grains at stir zone is one of the reason for high hardness that also strengthen the region than base material. Similarly, the tiny particles at the intermetallic region benefits to enhance the hardness.

2.3 Diffusion Bonding

One of the solid state joining method available is Diffusion bonding. It takes place when two metals are joined together by making them to contact with each other in such a way that, the temperature at the contact surfaces is less than 0.7 T_m under moderate pressure. This helps to reduce the macro deformation during the atomic migration. Most of the problems associated with the fusion welding is not taking place in diffusion bonding as the temperature available in this process is not exceeding the melting point. Traditional heating method is followed in this process having induction units and the entire process in carried out in a press.

Vacuum bonding is used for joining Mg/Al joints at a temperature range of 460–480 °C, having a pressure of 0.08–0.10 MPa and the time of the process is

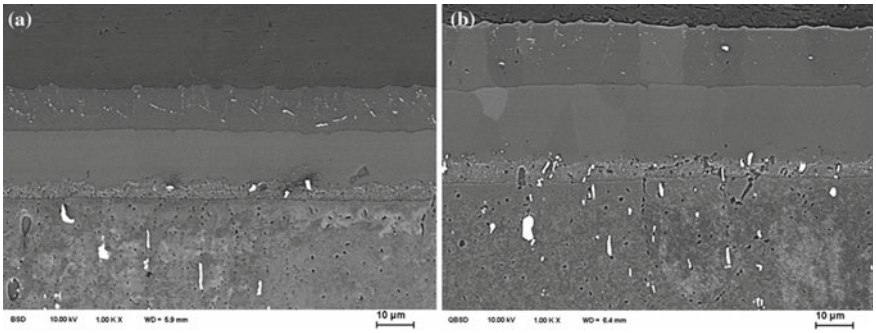

Fig. 8 Microstructures of Al/Mg diffusion welded joint at different temperatures [6]. **a** Diffusion-welding at 703 °C for 1200 s; **b** diffusion-welding at 703 °C for 1800 s

40–60 min [48]. Here there is formation of diffusion zones on both sides having two distinct transition zones. Different kinds of Mg_xAl_y phases were seen along the sides of the Al interface layer. They are: Mg_2Al_3, Mg_3Al_2 and Mg_2Al_3 respectively. Along the interface of the Mg side, Mg_3Al_2 phase is seen in addition to the Mg grains. This magnesium Mg_3Al_2 phase element has a FCC structure when compared to the HCP structure of magnesium grains. Research findings prove that, the resistance to the formation of cracks on the joints were reduced to a positive extent when there is formation of Mg_3Al_2. One of the important disadvantages with this process is the formation of the brittle intermetallic compound Mg–Al at the interface of the Mg and Al compounds which leads to the formation of cracks during service. Therefore, reducing the formation of these intermetallic compounds is the key factor in producing sound strong joints. One such method used to reduce this intermetallic compound formation is the introduction of a new interlayer in between the Al and Mg. Zn is used as an effective interlayer for producing AZ31B and AA6061 alloy joints [49]. Hot dipping method is used for depositing Zn layer having a thickness of 60 µm on the Al surface as shown in Fig. 8. The method was carried out for a time period of 3 s and with a temperature of 360 °C.

For alloys having higher melting temperatures such as Cu could be efficiently joined with Mg by using this Diffusion bonding process. A shear strength value of 66 MPa and a bonding strength of 81 MPa is achieved by joining these joints with temperature range of 450 °C and with a pressure of 12 MPa and 30 min [50].

2.4 Fusion Welding

The joining of aluminium and magnesium materials using fusion welding process, the results shows that the extended intermetallic layer gives lower mechanical properties when compared to the parent materials. The effect of intermetallic layer composition

and element distribution were precise to improve the metallurgical and mechanical properties of aluminium and magnesium joints.

In general zinc used as filler metals to improve the surface bonding between the dissimilar metals used in solid state welding process. Zhang et al. [51] utilised the MIG welding process with Zn foil as an thin intermetallic layer. They examined that the morphological evolution of aluminium and magnesium lap joints shows frequent aluminium-zinc intermetallic compound formation occur between the fuzion zone and the unmelted to magnesium parent metal. They also found that zinc act as a barrier between the parent metal zone and the mixed fusion zone. Scherm et al. [52] considered the three weight percentage of zincaluminium alloys with magnesium alloy using gas-tungsten arc welding process. They reported the effect of aluminium filler wire concentration affected the mechanical properties of Al/Mg joints. The surface structure and bonding strength exposed that a thin intermetallic phase seam didn't concurrence with a sophisticated strength of the joint, and also the bonding strength be subject to more on the depth of the weld penetration.

Figure 9 shows the thermodynamic behaviour of intermetallic compound in the Al–Mg–Ti ternary system and also to precise control of the laser power. For example, iron as an interlayer with aluminium/magnesium joints were lap together by means of a hybrid laser-TIG welding.

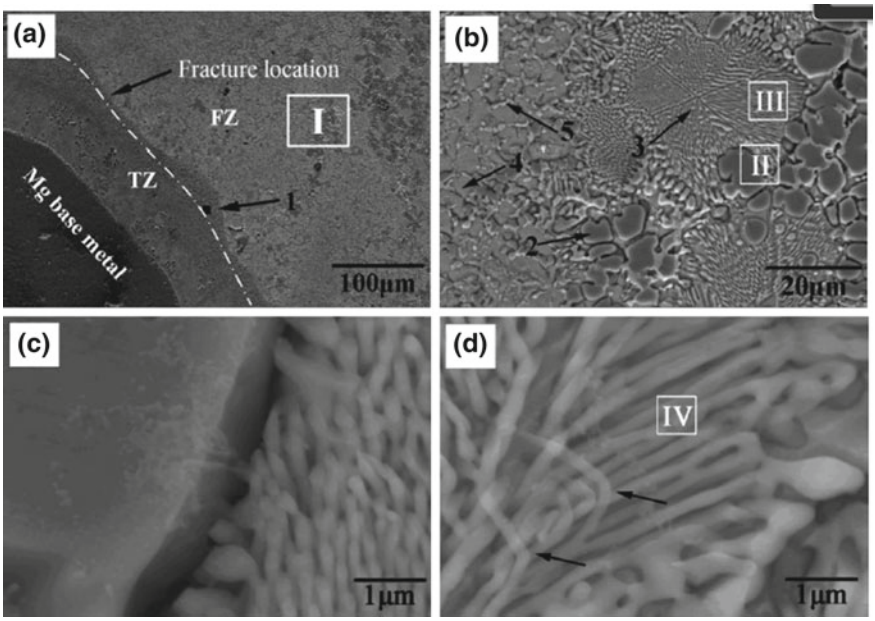

Fig. 9 Microstructures of the weak zone of the TIG welded joint with Zn-29.5Al-0.5Ti filler metal [53]. **a** The macrostructure near Mg base metal; **b** the magnification of area I from (**a**); **c** and **d** the magnified images of area II and III in (**b**)

The main significant effect of intermetallic compound formation were precised the properties of aluminium/magnesium joints using fusion welding process. Also, the interlayer improve the morphological properties using hybrid welding approach Generally, the used filler metals include pure Zn, Ti, Fe, Sn, Ni, and some binary alloys or ternary alloys, such as Zn–Al alloys, Sn–Zn alloy, Al–Si alloy, Zn–Al–Ti alloys and Zn–Al–Ce alloys and gradually reduces the strength in fusion welding [54, 55]. In any case, it is hard to discover one alloy which can totally take out Intermetallic compound with aluminium/magnesium joints. The few researcher explored intermetallic compounds, for example, Al–Fe and Al–Ti become the key factor in improving bonding quality, and later on some new composites ought to be investigated to take care of this issue. Some progressively ternary combinations might be utilized to improve the microstructures by second stage fortifying or fine grain reinforcing. Also, multicomponent compounds might be one appropriate decision for welding Mg and Al to maintain a strategic distance from intermetallic compounds [56, 57].

3 Summary

Different engineering applications such as automotives etc. use hybrid Al and Mg for making hybrid structures. Hence detailed research has been carried out in the joining of this dissimilar material combination by different joining techniques. This book chapter deals with the study of the properties and surface characteristics of Al–Mg dissimilar joints. One of the main problems faced during the joining of this dissimilar materials Al and Mg using all the techniques is the formation of the intermetallic compounds (IMCs) at the joint interface. Because of this intermetallic compound formation, which are hard and brittle in nature, there occurs a reduction in the strength of the joints produced. One of the three main approaches used for increasing the strength of the Mg/Al joints is the use of a solid-state joining process, improvement in the distribution and variety of the IMCs, and reducing the reaction and energy. Methods such as diffusion bonding and friction stir welding are capable of producing welds with sufficiently higher strengths as they require only lower welding temperatures. Eventhough there is reduction in the formation of these IMCs when there is reduction in the temperature of the welds, there is no chance for completely eliminating the IMCs formation. Fusion welding techniques such as laser welding uses a number of filler materials for reducing the formation of these intermetallic compounds. This usage of filler material has proved to reduce the formation of IMCs during Al/Mg joints and helped improve their mechanical properties. This surface characteristics of these Al/Mg joints could be still enhanced if more prominent solutions are found out by extending the research and development in this area.

References

1. Cam, G., Kocak, M.: Progress in joining of advanced materials. Int. Mater. Rev. **43**, 1–44 (1998)
2. Lanza, M., Lauro, A., Scanavino, S.: Fabrication and weldability in structures. AL Alumin. Alloys **13**, 80–86 (2001)
3. Meshram, S.D., Mohandas, T., Madhusudhan Reddy, G.: Friction welding of dissimilar pure metals. J. Mater. Process. Technol. **184**, 330–337 (2007)
4. Rajesh, N., et al.: Mechanical evaluation and microstructure of friction welded aluminium-mild steel joints. Arab. J. Sci. Eng. **39**, 5017–5023 (2014)
5. Mishra, A.: Friction stir welding of dissimilar metal: a review. Int. J. Res. Appl. Sci. Eng. Technol. **6**(I), 1551–1559 (2018)
6. Liu, Liming, Ren, Daxin, Liu, Fei: A review of dissimilar welding techniques for magnesium alloys to aluminum alloys. Materials (Basel) **7**(5), 3735–3757 (2014)
7. Sassani, F., Neelam, J.R.: Friction Welding of Incompatible Materials, 264-s I, Nov 1988
8. Giummarra, C., Thomas, B., Rioja, R.J.: New aluminum lithium alloys for aerospace applications. In: Proceedings of the Light Metals Technology Conference (2007)
9. Rajesh, et al.: Investigation on joining of aluminum & mild steel by friction stud welding. Mater. Manuf. Process **27**, 1409–1413
10. Blawert, C., Hort, N., Kainer, K.U.: Automotive applications of magnesium and its alloys. Institute for Materials Research, 10 May 2004
11. Mordike, B.L., Ebert, T.: Magnesium: properties—applications—potential. Mater. Sci. Eng. A **302**, 37–45 (2001)
12. Borrisutthekul, R., Miyashita, Y., Mutoh, Y.: Dissimilar material laser welding between magnesium alloy MgAZ31B and aluminum alloy A5052-O. Sci. Technol. Adv. Mater. **6**, 199–204 (2005)
13. Liu, P., Li, Y., Wang, J., Haijun, M.A., Guo, G., Geng, H.: Microstructure and phase constituents in the interface zone of Mg/Al diffusion bonding. Metall. Mater. Trans. B **37**, 649–654 (2006)
14. Cao, R., Wen, B.F., Chen, J.H., Wang, P.C.: Cold metal transfer joining of magnesium MgAZ31B-to-aluminum A6061-T6. Mater. Sci. Eng. A **560**, 256–266 (2013)
15. Liang, Z., Qin, G., Wang, L., Meng, X., Li, F.: Microstructural characterization and mechanical properties of dissimilar friction welding of 1060 aluminum to MgAZ31B magnesium alloy. Mater. Sci. Eng. A **645**, 170–180 (2015)
16. Kimura, M., Fuji, A., Shibata, S.: Joint properties of friction welded joint between pure magnesium and pure aluminium with post weld heat treatment. Mater. Des. **85**, 169–179 (2015)
17. Paradiso, V., Rubino, F., Carlone, P., Palazzo, G.S.: Magnesium and aluminium alloys dissimilar joining by friction stir welding. Procedia Eng. **183**, 239–244 (2017)
18. Su, J.Q., Nelson, T.W., Mishra, R., Mahoney, M.: Microstructural investigation of friction stir welded 7050-T651 aluminium. Acta Mater. **51**, 713–729 (2003)
19. Hirano, S., Okamoto, K., Doi, M., Okamura, H., Inagaki, M., Aono, Y.: Microstructure of dissimilar joint interface of magnesium alloy and aluminum alloy by friction stir welding. Q. J. Jpn. Weld. Soc. **21**, 539 (2003)
20. Park, S.H.C., Michiuchi, M., Sato, Y.S., Kokawa, H.: Dissimilar friction-stir welding of Al alloy 1050 and Mg alloy AZ31. In: Proceedings of the International Welding/Joining Conference-Korea, Gyeongju, Korea, pp. 534–538, 28–30 Oct 2002
21. Yan, Y., Zhang, D.T., Qiu, C., Zhang, W.: Dissimilar friction stir welding between 5052 aluminum alloy and AZ31 magnesium alloy. Trans. Nonferrous Met. Soc. China **20**, S619–S623 (2010)
22. Somasekharan, A.C., Murr, L.E.: Microstructures in friction-stir welded dissimilar magnesium alloys and magnesium alloys to 6061-T6 aluminum alloy. Mater. Charact. **52**, 49–64 (2004)
23. Straumal, B.B., Baretzky, B., Kogtenkova, O.A., Straumal, A.B., Sidorenko, A.S.: Wetting of grain boundaries in Al by the solid Al_3Mg_2 phase. J. Mater. Sci. **45**, 2057–2061 (2010)
24. Protasova, S.G., Kogtenkova, O.A., Straumal, B.B., Zieba, P., Baretzky, B.: Inversed solid-phase grain boundary wetting in the Al–Zn system. J. Mater. Sci. **46**, 4349–4353 (2011)

25. Gerlich, A., Su, P., Yamamoto, M., North, T.H.: Material flow and intermixing during dissimilar friction stir welding. Sci. Technol. Weld. Join. **13**, 254–264 (2008)
26. Mahoney, M.W., Rhodes, C.G., Flintoff, J.G., Bingel, W.H., Spurling, R.A.: Properties of friction-stir-welded 7075 T651 aluminum. Metall. Mater. Trans. A **29**, 1955–1964 (1997)
27. Guerra, M., Schmidt, C., McClure, J.C., Murr, L.E., Nunes, A.C.: Flow patterns during friction stir welding. Mater. Charact. **49**, 95–101 (2003)
28. Suni, B.R., Reddy, G.P.K., Mounika, A.S.N., Sree, P.N., Pinneswari, P.R.: Joining of AZ31 and AZ91 Mg alloys by friction stir welding. J. Magnes. Alloys **3**, 330–334 (2015)
29. Jaiganesh, V., Sevvel, P.: Effect of process parameters on the microstructural characteristics and mechanical properties of AZ80AMg alloy during friction stir welding. Trans. Indian Inst. Met. **68**, 99–104 (2015)
30. Rose, A.R., Manisekar, K., Balasubramanian, V.: Influences of welding speed on tensile properties of friction stir welded AZ61A magnesium alloy. J. Mater. Eng. Perform. **21**, 257–265 (2012)
31. Kouadri-Henni, A., Barrallier, L.: Mechanical properties, microstructure and crystallographic texture of magnesium AZ91-D alloy welded by friction stir welding (FSW). Metall. Mater. Trans. A **45**, 4983–4996 (2014)
32. Mofid, M.A., Abdollah-Zadeh, A., Malek Ghaini, F.: The effect of water cooling during dissimilar friction stir welding of Al alloy to Mg alloy. Mater. Des. **36**, 161–167 (2012)
33. Cooke, K.O., Alhazaa, A., Atieh, A.M.: Dissimilar Welding and Joining of Magnesium Alloys: Principles and Application. Intech Open. http://dx.doi.org/10.5772/intechopen.85111, 23 Apr 2019
34. Singh, K., Singh, G., Singh, H.: Review on friction stir welding of magnesium alloys. J. Magnes. Alloys (2018)
35. Venkateswaran, P., Reynolds, A.P.: Factors affecting the properties of friction stir welds between aluminum and magnesium alloys. Mater. Sci. Eng. A **545**, 26–37 (2012)
36. Elanchezhian, C., Ramnath, B.V., Venkatesan, P., Sathish, S., Vignesh, T., Siddharth, R.V., Gopinath, K.: Procedia Eng. **97**, 775–782 (2014)
37. Chen, Y.C., Nakata, K.: Friction stir lap joining aluminum and magnesium alloys. Scr. Mater. **58**, 433–436 (2008)
38. Chowdhury, S.H., Chen, D.L., Bhole, S.D., Cao, X., Wanjara, P.: Lap shear strength and fatigue life of friction stir spot welded AZ31 magnesium and 5754 aluminum alloys. Mater. Sci. Eng. A **556**, 500–509 (2012)
39. Kwon, Y.J., Shigematsu, I., Saito, N.: Dissimilar friction stir welding between magnesium and aluminum alloys. Mater. Lett. **62**, 3827–3829 (2008)
40. Kouadri-Henni, A., Barrallier, L.: Mechanical properties, microstructure and crystallographic texture of magnesium AZ91-D alloy welded by friction stir welding (FSW). Metall. Mater. Trans. A **45**, 4983–4996 (2014)
41. Esparza, J.A., Davis, W.C., Trillo, E.A., Murr, L.E.: J. Mater. Sci. Lett. **21**(12), 917–920 (2002)
42. Lim, S., Kim, S., Lee, C.G., Kim, S.J., Yim, C.D.: Metall. Mater. Trans. A **36**(6), 1609–1612 (2005)
43. Lee, W.B., Yeon, Y.M., Jung, S.B.: Mater. Sci. Technol. **19**(6), 785–790 (2003)
44. Padmanaban, G., Balasubramanian, V.: Mater. Des. **30**(7), 2647–2656 (2009)
45. Chowdhury, S.H., Chen, D.L., Bhole, S.D., Cao, X., Wanjara, P.: Metall. Mater. Trans. A **44**(1), 323–336 (2013)
46. Choi, D.H., Ahn, B.W., Kim, S.K., Yeon, Y.M., Kim, Y.J., Park, S.K., Jung, S.B.: Mater. Trans. **52**(4), 802–805 (2011)
47. Singarapu, U., Adepu, K., Arumalle, S.R., Magnes, J.: Alloys **3**(4), 335–344 (2015)
48. Liu, L.M., Tan, J.H., Liu, X.J.: Reactive brazing of Al alloy to Mg alloy using zinc-based brazing alloy. Mater. Lett. **61**, 2373–2377 (2007)
49. Zhao, L.M., Zhang, Z.D.: Effect of Zn alloy interlayer on interface microstructure and strength of diffusion-bonded Mg-Al joints. Scr. Mater. **58**, 283–286 (2008)
50. Liu, L.M., Zhao, L.M., Xu, R.Z.: Effect of interlayer composition on the microstructure and strength of diffusion bonded Mg/Al joint. Mater. Des. **30**, 4548–4551 (2009)

51. Zhang, H.T., Song, J.Q.: Microstructural evolution of aluminum magnesium lap joints welded using MIG process with zinc foil as an interlayer. Mater. Lett. **65**, 3292–3294 (2011)
52. Scherm, F., Bezold, J., Glatzel, U.: Laser welding of Mg alloy $MgAl_3Zn_1$ (AZ31) to Al alloy $AlMg_3$ (AA5754) using ZnAl filler material. Sci. Technol. Weld. Join. **17**, 364–367 (2012)
53. Liu, F., Zhang, Z.D., Liu, L.M.: Microstructure evolution of Al/Mg butt joints welded by gas tungsten arc with Zn filler metal. Mater. Charact. **69**, 84–89 (2012)
54. Şahin, M.: Friction welding of different materials. In: International Scientific Conference, Gabrovo, 19–20 Nov 2010
55. Liang, Z., Qin, G., Geng, P., Yang, F., Meng, X.: Continuous drive friction welding of 5A33 Al alloy to MgAZ31B alloy. J. Manuf. Process. **25**, 153–162 (2017)
56. Liu, F., Ren, D.X., Liu, L.M.: Effect of Al foils interlayer on microstructures and mechanical properties of Mg-Al butt joints welded by gas tungsten arc welding filling with Zn filler metal. Mater. Des. **46**, 419–425 (2013)
57. Automotive Uses of Magnesium Alloys: Part One, Total Materia, July 2010

Analytical Modelling for Laser Heating for Materials Processing and Surface Engineering

Jaideep Dutta, Balaram Kundu, Hargovind Soni, and Peter Madindwa Mashinini

Abstract Light amplification by stimulated emission of radiation (laser) is an organized monochromatic electromagnetic radiation beam which can proliferate linearly with negligible disparity and the source of energy is found in broad spectrum of wavelength. Laser has been witnessed as ample applications in thermal processing right from material processing to thermal therapy for cancer treatment. The laser processing of materials can be classified as: laser assisted machining, forming, joining and surface engineering. The emitted energy source from laser can be spotlighted into a small spot and it caters a large amount of intense energy which is quintessential for penetration in materials for surface treatment. In this book chapter, exact analytical solution of three-dimensional dual-phase-lag heat conduction model has been developed under the influence of non-Gaussian time and space dependent laser heat source. The corresponding mathematical solution is obtained with implementation of 'Finite integral transform' and 'Duhamel's theorem'. The consequence of lagging behaviour on laser heating has been studied. The laser heating process variables such as laser exposure, power density have been investigated with temperature variation. The development of surface thermal contours defines the heat flow in the substrate domain. The accuracy of present mathematical modelling has been justified based on the physical phenomena observed under laser heating.

Keywords Laser · Dual-phase-lag · Thermal response · Three dimensional · Analytical solution

J. Dutta (✉)
Department of Mechanical Engineering, MCKV Institute of Engineering, 243, G. T. Road (N), Liluah, Howrah 711204, West Bengal, India
e-mail: jdutta.mech@gmail.com

J. Dutta · B. Kundu
Department of Mechanical Engineering, Jadavpur University, Raja S. C. Mallick Road, Kolkata 700032, West Bengal, India

H. Soni · P. M. Mashinini
Mechanical and Industrial Engineering Technology, University of Johannesburg (Doornfontein Campus), Johannesburg, South Africa

K. Gupta (ed.), *Surface Engineering of Modern Materials*, Engineering Materials,
https://doi.org/10.1007/978-3-030-43232-4_5

1 Introduction

The contribution of laser processing of materials in the domain of engineering as well as medical science in recent years is an absolute plethora. The application of laser source as thermal energy finds a myriad of applications from development of new materials with better surface finish along with joining and heat treatment of several metallurgical applications to medical therapy for eradication of cancer treatment and so on [1–4]. Laser welding has been emerged as essential joining process for several grades of metallic and non-metallic materials. From past few decades of rigorous development in high power laser technology, joining of thicker sections of materials is now possible by laser welding. Though laser processing of materials gives better quality of product in less production time, but it is actually very challenging job to set the exact input variables such as scanning velocity, input power, selection of material, design of several process variables to produce the defect free weld with desired surface quality at the time of reproducible conditions in industry. To achieve the successful operation of laser processing, better understanding and strong idea about the elemental physical phenomena of laser processing is necessary. Since a large number of research papers, books and book chapters are published by researchers, this book chapter is intended to focus specifically on development of three-dimensional mathematical modelling of Dual-phase-lag (DPL) heat conduction by implementing space and time dependent laser heat source moving in a metallic surface.

2 Fundamental of Laser Surface Processing

2.1 Propagation of Irradiation Properties in Materials

A laser is a device that emits light through a process of optical amplification based on stimulated emission of electromagnetic radiation. The deposited energy in region's surface is purely depends on the refractive property of the material. When light drives on the material, a significant portion of the incident energy will be reflected from the surface due to discontinuity and rest of the energy will be transmitted into the material. The reflectivity of a specific material is dependent on the frequency of the light source through the scattering relation of its index of refraction. In case of normal incidence, magnitude for reflectivity of metals in the near ultraviolet and visible spectral range are lies in between 0.4–0.95 and in between 0.9–0.99 for the infrared wave [1]. Also the reflectivity of a surface builds upon the temperature of the material with variation of permittivity, band structure, plasma oscillations and material phase [5]. For example, the reflectivity of silicon increases by 2% while for Ni, it changes by a minute percent [6] at the time of melting.

2.2 Energy Propagation and Absorption Mechanism in Laser Irradiation

The utilization of heat treatment by using thermal energy source finds ample applications such as welding, cutting, cladding, hardening and several other industrial operations. In this process, heat conduction possesses the dominant role as a universal method. Advanced material processing technologies with betterment of material surface are in demanding sector right now in the arena of different manufacturing disciplines. Lasers are recognized to be advanced material processing appliance creating the bridge between conventional and advanced manufacturing technology. A high intensity laser source is targeted on the substrate surface and during this course the partial amount of laser beam is being absorbed by the substrate material (refer Fig. 1). The substrate material endures solid heating, melting and evaporation and these phenomena strongly depend upon the focused beam diameter of the surface, reflectivity of the surface and laser power intensity. As heating process advance, the liquid surface of substrate material progresses towards the solid bulk and forms crater on the incident material [7]. The higher demand of laser technology in various real life applications is due to its low cost, accurate processing, precision with better controlled action and high speed of operation. Though laser source seems to be localized heating source but the physical process behind its machining operation is sophisticated in nature and betterment of analysis (both theoretical and experimental) is always required for understanding the process to ensure superior aspect of end product development. Laser machining process can be categorized into two divisions: firstly laser conduction limited heating viz. substrate material is heated up to its melting point and the material remains in solid condition; secondly laser non-conduction heating where the substrate material undergoes phase change process [8].

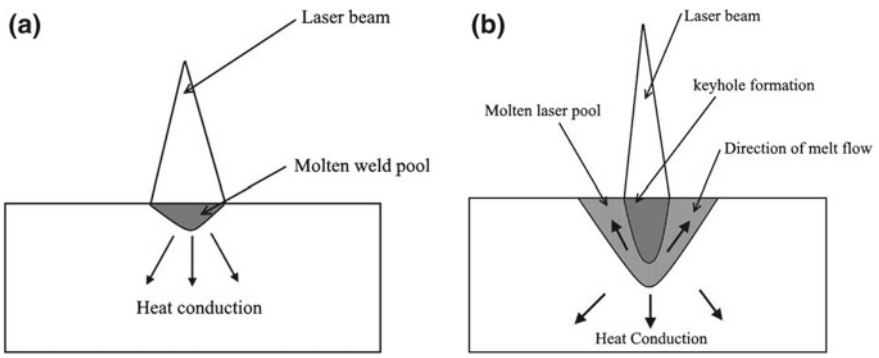

Fig. 1 Schematic diagram of heat flow process in laser welding of **a** mild penetration and **b** deep penetration

2.3 Heat Transfer Modelling in Moving Laser Source

In case of any photo-thermal processing operation, the thermal response developed by the material is solely due to temperature elevation. Hence to develop knowledge about laser interaction in materials, it is essential to model the heat transfer characteristics inside the material during movement of heat source. From the postulate of heat transfer modelling, the temporal and spatial characteristic is governed by specific heat transfer equation. The heat equation is generated based on energy conservation principle and Fourier's law of heat conduction [9]. For Cartesian coordinate system, the governing differential equation for temperature distribution can be represented as follows [10]:

$$k\nabla^2 T(\vec{r}, t) + Q(\vec{r}, t) = \rho c_p \frac{\partial T(\vec{r}, t)}{\partial t} \tag{1}$$

In Eq. (1), ρ is the mass density, c_p is the specific heat at constant pressure, k is the thermal conductivity and $\vec{r}$ is the spatial coordinate in the domain. The term $Q(\vec{r}, t)$ is the time and spatial dependent heat source and the elevated temperature inside the substrate material is driven by this volumetric heat source term along with the predefined boundary conditions. The laser scanning velocity is usually incorporated in the heating source term to realize the change in location from one point to another point during the movement of heat source. This term also consists of laser power density which is considered to be power input of movement process.

The absorption of laser source on the substrate material occurs over photon interaction with bound and free electrons of the material structure. The amplification of this incident energy takes place with various collision mechanisms associating electrons, lattice site phonons, ionized impurities, and defect structures. The energy transfer from electron subsystem to lattice subsystem purely depends of the collision between electrons and lattice structures and the entire energy conversion mechanism follows the path of electron kinetic theory approach [11–13].

In any kind of laser heating applications, development of thermal history is much essential phenomenon to analyse. Because whatsoever processing or formation happened in the substrate material is due to change in temperature. Researchers have focused theoretically (by development of mathematical models) as well as experimentally to bring out the best form of laser heat source applicable for processing. Yilbas [14] developed one-dimensional analytical solution of temperature distribution unsteady heat conduction model of semi-infinite solid influenced by step input laser heat source based on Laplace transform method and found out that maximum surface temperature is independent of wavelength of laser. Yilbas [15] portrayed numerical investigation of three-dimensional laser thermal studies based on explicit scheme with validation of experimental results and the research outcome indicated the influence of laser power intensity distribution across the heated spot. Yilbas and Kalyon [16] produced analytical solution of temperature response in pulsed laser heating process based on Laplace transform method with implementation of convective kind boundary conditions in metallic substrates and the impact of laser

parameters along with influence of Biot no. (Bi) has been investigated on temperature profiles. Yilbas et al. [17] developed analytical solution of electron and lattice temperature distribution by introducing strained parameters method for short laser pulse and it has been found that electron temperature decays sharply while lattice temperature increases gradually in the metallic surface region during cooling cycle. Kalyon and Yilbas [18] evolved analytical solution of electron-lattice subsystem temperature distribution based on Laplace Transform method and found that electron and lattice temperature becomes similar for heating period beyond the thermal equilibrium time. Hsiao et al. [19] analytically solved one-dimensional transient heat conduction model under the influence of Gaussian laser pulse applicable to laser-assisted direct imprinting (LADI) technique and analyzed different imprinting parameters during laser induced melting and solidification. Bouaziz and Boutalbi [20] investigated thermal analysis of laser heating with different shaped time dependent laser source by employing semi-analytical method and it was found that time needed for the desired surface temperature is sensitive to the temporal pulse shape. Yilbas et al. [21] derived analytical solution of one-dimensional temperature response under laser short-pulse by imposing hyperbolic heat conduction model and research outcome denotes that increasing laser pulse length results in slow temperature rise during heating period. Yilbas and Al-Dweik [22] produced analytical solution of lattice and electron temperature on the basis of finite Lie point symmetries and similarity solution to promote the non-equilibrium energy transfer in electron-lattice subsystem in a gold substrate in which the collisional energy transfer has been thoroughly studied under the influence of laser heating. Qi et al. [23] utilized time fractional Cattaneo model for computing temperature response with Laplace transform method and the impact of transient time and order of fractional derivate term has been analyzed. Zhang and Shang [24] considered the two-dimensional hyperbolic heat conduction model and the corresponding solution has been produced by implementing Laplace and Hankel-transform scheme of semi-infinite domain subjected to laser irradiation and brought out the impact of non-Fourier heating under laser irradiance. Peng [25] represented general solution of three-dimensional transient temperature field (Fourier) in a finite slab heated by moving heat source with application of integral transform method and for comparison study finite element method based numerical simulation has been performed. Chen et al. [26] solved two-dimensional Fourier axi-symmetric heat conduction model under step laser heat pulse with application of combined form of Green's function approach and Laplace transform method and temperature distribution has been computed for different radial locations, axial locations for different duty cycles and repetitive laser frequencies. Kashani et al. [27] presented analytical solution of three-dimensional transient temperature field of rotating cylinder subjected to laser assisted machining by employing Green's function method and this result has been compared with numerical solution carried out in ABAQUS software and importance of surface absorption coefficient has been investigated. Chen [28] established analytical solution of two-dimensional axi-symmetric Fourier heat conduction model with Laplace transform method and separation of variables under the influence of long pulse laser irradiance along with temperature dependent surface absorption and revealed the thermal interaction between heat source and

metal. Chen and Bi [29] obtained closed form solution of temperature distribution of three-dimensional heat conduction model by implementation of integral transform method under the influence of elliptical Gaussian laser beam. Chen [30] represented analytical solution of two-dimensional axi-symmetric heat conduction model for long pulse laser heating material with convective boundary conditions. Feng et al. [31] portrayed analytical solution of three-dimensional heat conduction model by employing Duhamel's theorem subjected to hybrid laser-waterjet micro machining technology with appropriate boundary conditions along with experimental research work. Ma et al. [32] employed Green's function method to produce analytical solution of two-dimensional dual-phase-lag (DPL) heat conduction model under the influence of moving non-Gaussian laser source and the effect of scanning speed along with phase lag parameters on temperature distribution have been discussed.

Fourier's law of heat conduction model is widely utilized for solving problems on heat transfer in past decades. This model is purely based on infinite energy propagation [33, 34]. While in real world, energy propagates in finite velocity i.e. thermal gradient takes place after certain finite time period of imposing heat flux. In this regard Fourier's law fails to capture the practical aspects of heat transfer. Dual-phase-lag (DPL) model is considered as most updated model which takes account of finite energy transfer concept by introducing two time lags viz. relaxation time for heat flux and temperature gradient [35]. From the viewpoint of mathematical modelling it can be stated that for same governing differential equation if both analytical and numerical solution is available then obviously analytical solution will be preferred as it is independent on domain size and solution is exact.

Based on the research work carried out in last few decades on thermal analysis of laser processing of materials, in present book chapter initiatives have been taken to construct the three dimensional analytical solution of DPL heat conduction model under the influence of volumetric laser heat source in a finite domain (square shaped). This is the first attempt to solve 3-D DPL model subjected to laser heating of materials (as per author's knowledge based on heuristic literature survey). The corresponding model is being solved by hybrid form of 'Finite integral transform' and 'Duhamel's theorem'. The impact of phase lags behaviour imposed by DPL model is investigated on laser thermal response. The orientation of 3-D surface contours is being studied in different spatial directions. Mathematically as well as physically the thermal behaviour of laser heating is being justified from the view point of material surface processing.

3 Mathematical Modelling of Moving Laser Source

Thermal analysis in laser heating is a complex phenomenon and it requires appropriate design variables with skillful knowledge about movement of laser source and it's interaction with substrate material. However mathematical modelling can be precious regarding the prediction of thermal behavior during laser heating. Though

mathematical models are based on some assumptions due to complexity in solving. But mathematical modelling can provide a glimpse of results which can be found out during solving by imposing accurate process parameters. As heat transfer study is predominant in laser processing, temperature response can be developed by employing Fourier's law of heat conduction based on the respective geometry of the substrate material. The selection of boundary conditions are important during heat transfer investigation. The mathematical solution can be generated either by analytical approach or by numerical schemes. The analytical solutions are exact and it doesn't have any error as it doesn't depend on the size of the solution domain while numerical schemes are dependent upon the size of the domain and the procedure of discretization method. Though mathematical formulation of any physical operation is based on some practically feasible assumptions due to difficulties in consideration of induced non-linearity, the output actually portrays the glimpse of actual phenomena and such insight is helpful for establishment of successful process planning layout.

3.1 DPL Heat Conduction Model

Rapid heating of objects in short span of time is an emerging area of heat transfer and laser heating process is one of most ideal example of such perspective. To analyse this effectively, the association of irreversible non-equilibrium thermodynamics and microscopic effects of energy exchange is essential. Fourier's heat conduction theory is based on infinite energy propagation and it suggests that thermal gradient is produced due to impose of heat flux. But in practical world, thermal gradient is produced on any object due to heating with a certain time lag between this. A thermodynamic state needs a certain time period to reach in equilibrium state and this signifies the transition period from non-equilibrium to equilibrium zone. Cattaneo [36] and Vernotte [37] first developed heat conduction model by modifying Fourier's postulate by addition of thermal relaxation time lag of heat flux. This model is termed as hyperbolic heat conduction (HHC) model or Cattaneo-Vernotte (C-V) model. But this model is not able to capture the microscopic response in the material. Tzou [38] further renovated the Fourier's heat conduction model by associating the two thermal relaxation time lags viz. thermal relaxation time lag for heat flux and for thermal gradient. Because of the presence of two phase lags, this postulate is denoted as dual-phase-lag (DPL) model where it has been allowed either the temperature gradient to precede heat flux or the heat flux to precede temperature gradient. Apart from the core engineering fields, DPL model is commonly employed in therapeutic treatment. Many researchers [39–41] have explored the laser heating process of biological tissue in thermal therapy based on different heat conduction models, including Fourier's Law, C-V model and DPL model. Comparison among the research output of the three theories suggested that the DPL model would lead to the same results as Fourier's Law in case of same magnitude of two time lags under uniformly distributed initial condition.

The DPL postulate of heat conduction model is [42]:

$$q\left(\vec{r}, t + \tau_q\right) = -k\nabla T(\vec{r}, t + \tau_T) \tag{2}$$

where, q is the heat flux vector, T is the temperature and k is the thermal conductivity. τ_q and τ_T are the phase lags of heat flux vector and thermal gradient respectively. Taylor's 1st order expansion on Eq. (2) gives:

$$q(\vec{r}, t) + \tau_q \frac{\partial q(\vec{r}, t)}{\partial t} = -k\left[\nabla T(\vec{r}, t) + \tau_T \frac{\partial}{\partial t}\nabla T(\vec{r}, t)\right] \tag{3}$$

The energy equation with volumetric heat source is [43]:

$$-\nabla \cdot q(\vec{r}, t) + Q(\vec{r}, t) = \rho c \frac{\partial T(\vec{r}, t)}{\partial t} \tag{4}$$

where, $Q(\vec{r}, t)$ is the source term generally expressed as heat generation per unit volume, ρ and c are the density and specific heat respectively.

The coupled form of Eqs. (3) and (4) yields the DPL heat conduction model and mathematically it can be expressed as:

$$\nabla^2\left(T + \tau_T \frac{\partial T}{\partial t}\right) + \frac{1}{k}\left(Q + \tau_q \frac{\partial Q}{\partial t}\right) = \frac{1}{\alpha}\left(\frac{\partial T}{\partial t} + \tau_q \frac{\partial^2 T}{\partial t^2}\right) \tag{5}$$

3.2 Problem Formulation

Considering a square shaped cuboid plate (refer Fig. 2) subjected to moving laser heat source in three dimensions at constant speed of v. The plate has length of l ($0 \leq x \leq 1$), width of l ($-1/2 \leq y \leq 1/2$) and height of l ($0 \leq z \leq -1$). The plate remains static and heat source moves along the x-direction and the impact of thermal response in all three directions will be studied.

The assumptions for present mathematical formulation are as follows:

(a) Thermal conductivity (k) and density (ρ) is constant.
(b) The laser source (heat generation term) is dependent on time and space coordinates.
(c) The boundary conditions along all the directions are termed as insulated (zero thermal gradient) to emphasize the minimum heat loss during movement of laser source.
(d) In dual-phase-lag (DPL) model, the thermal relaxation time lags are considered to be constant in magnitude.
(e) The substrate material is considered as cuboid in shape.
(f) Impact of convection and radiation heat transfer has been neglected due to dominance of conduction heat transfer.

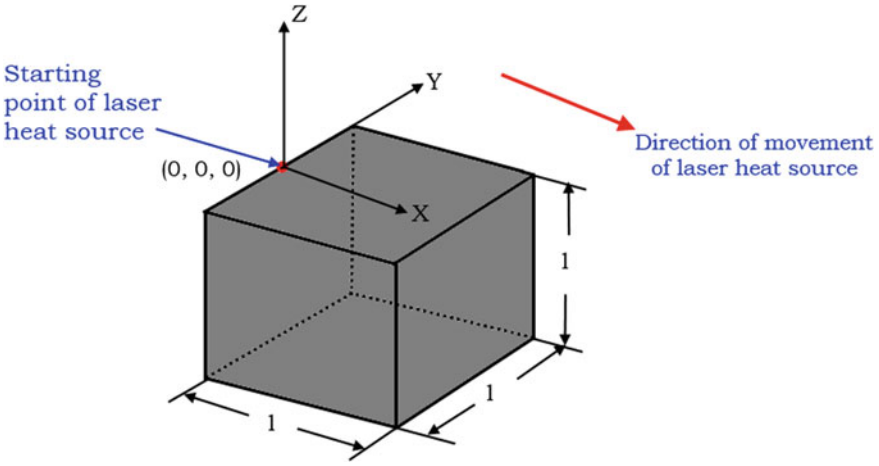

Fig. 2 Schematic diagram of substrate material plate (square shaped) subjected to moving laser heat source

In this research work, a time decaying laser heat source term has been considered and it can be expressed as [32]:

$$Q = \frac{R_a L_0}{t_p^2} t \exp\left(-\frac{t}{t_p}\right)\delta(x - vt)\delta(y)\delta(z) \tag{6}$$

where, R_a is the energy absorption ratio, L_0 and t_p are the power density and duration time of heat source respectively. v is the speed of moving laser source and t is the time. x, y and z are the spatial directions. δ() is the Dirac-delta function.

The boundary condition in all six edges is assumed to be zero thermal gradients and mathematically it can be presented as:

$$\begin{cases} \frac{\partial T}{\partial x}_{|x=0} = 0 & \frac{\partial T}{\partial x}_{|x=1} = 0 \\ \frac{\partial T}{\partial y}_{|y=-1/2} = 0 & \frac{\partial T}{\partial y}_{|y=+1/2} = 0 \\ \frac{\partial T}{\partial z}_{|z=0} = 0 & \frac{\partial T}{\partial z}_{|z=-1} = 0 \end{cases} \tag{7}$$

The boundary conditions presented in Eq. (7) is based on the literature survey [29–32] specifically on thermal analysis of laser irradiated moving heat source. The particular laser heat source (refer Eq. (6)) has been incorporated in the governing differential equation (see Eq. (5)), hence zero thermal gradient boundary condition (2nd kind) has been imposed on boundary surfaces of the domain as portrayed in Fig. 2. In this regard, it can be mentioned that application of constant temperature boundary condition (1st kind) is also valid in such modelling [32].

The initial condition for present mathematical modelling is as follows:

$$\begin{cases} T_{|t=0} = T_0 \\ \frac{\partial T}{\partial t}_{|t=0} = 0 \end{cases} \tag{8}$$

When laser irradiation hasn't been started, the surface temperature of substrate material is in ambience and hence it would be a constant temperature initial condition as presented in Eq. (8). The governing differential equation of present modelling (see Eq. (5)) is composed of 2nd order time derivative. Hence to solve such model, temperature differential w.r.t. time has been considered as zero [33].

The non-dimensional form of Eq. (5) can be depicted as follows:

$$\frac{\partial^2\theta}{\partial X^2} + \frac{\partial^2\theta}{\partial Y^2} + \frac{\partial^2\theta}{\partial Z^2} + Ve_T \frac{\partial}{\partial F}\left[\frac{\partial^2\theta}{\partial X^2} + \frac{\partial^2\theta}{\partial Y^2} + \frac{\partial^2\theta}{\partial Z^2}\right] + AF\exp(-F)\Phi(X, Y, Z) = \frac{\partial\theta}{\partial F} + \frac{\partial^2\theta}{\partial F^2} Ve_q \tag{9}$$

where, the normalization parameters are as follows:

$$\theta = \frac{T - T_0}{T_0}; X = \frac{x}{\sqrt{\alpha t_p}}; Y = \frac{y}{\sqrt{\alpha t_p}}; Z = \frac{z}{\sqrt{\alpha t_p}}; Ve_q = \frac{\tau_q}{t_p}; Ve_T = \frac{\tau_T}{t_p}; F = \frac{t}{t_p};$$
$$V = \frac{v}{\sqrt{\alpha/t_p}}; L = \frac{1}{\sqrt{\alpha t_p}}; A = \frac{\alpha R_a L_0}{kT_0}; \Phi(X, Y, Z) = \delta(X - VF)\delta(Y)\delta(Z) \tag{10}$$

In Eq. (9), F is the non-dimensional form of time and it is the most essential parameter of present formulation as it is the ratio of transient response to pulse time. The peak temperature development in different material depends mostly on the magnitude of 'F'.

The non-dimensional boundary conditions are as follows:

$$\begin{cases} \frac{\partial\theta}{\partial X}_{|X=0} = 0 & \frac{\partial\theta}{\partial X}_{|x=L} = 0 \\ \frac{\partial\theta}{\partial Y}_{|Y=-L/2} = 0 & \frac{\partial\theta}{\partial Y}_{|Y=+L/2} = 0 \\ \frac{\partial\theta}{\partial Z}_{|Z=0} = 0 & \frac{\partial\theta}{\partial Z}_{|Z=-L} = 0 \end{cases} \tag{11}$$

The non-dimensional initial conditions are as follows:

$$\begin{cases} \theta_{|F=0} = 0 \\ \frac{\partial\theta}{\partial F}\big|_{F=0} = 0 \end{cases} \tag{12}$$

3.3 Analytical Solution of Present Governing Differential Equation

In present research work, the combined form of 'Duhamel's theorem' and 'Finite Integral transform' method has been employed. The prime reason of implementation of Duhamel's theorem is presence of time and space dependent heat source term in governing differential equation (refer Eq. (9)). The speciality of this theorem is handling of such kind of source term in partial differential equations.

According to Duhamel's theorem, the initial condition of present research work can be modified as follows [43]:

$$\begin{cases} \theta_{|F=0} = 0 \\ \frac{\partial\theta}{\partial F}\big|_{F=0} = A\tilde{F}\exp(-\tilde{F})\Phi(X, Y, Z) \end{cases} \tag{13}$$

The modified form of Eq. (9) can be written as (after improvisation in Eq. (13)):

$$\frac{\partial^2\theta}{\partial X^2} + \frac{\partial^2\theta}{\partial Y^2} + \frac{\partial^2\theta}{\partial Z^2} + Ve_T\frac{\partial}{\partial F}\left[\frac{\partial^2\theta}{\partial X^2} + \frac{\partial^2\theta}{\partial Y^2} + \frac{\partial^2\theta}{\partial Z^2}\right] = \frac{\partial\theta}{\partial F} + \frac{\partial^2\theta}{\partial F^2}Ve_q \tag{14}$$

Equation (14) is set of higher order mixed partial differential equation which can be solved easily by finite integral transform method as this method converts partial differential equation to ordinary form with integral transform.

The pair of triple integral transform can be written as follows [44]:

$$\theta'''(i, j, k, F) = \int_{X=0}^{L}\int_{Y=L/2}^{Y=+L/2}\int_{Z=0}^{Z=-L}\theta(X, Y, Z, F)\cos(\alpha_i X)\cos\left(\alpha_j Y\right)\cos(\alpha_k Z)dXdYdZ \tag{15}$$

The corresponding inverse theorem is [44]:

$$\theta(X, Y, Z, F) = 8\sum_{i=0}^{\infty}\sum_{j=0}^{\infty}\sum_{k=0}^{\infty}\theta'''(i, j, k, F)\cos(\alpha_i X)\cos\left(\alpha_j Y\right)\cos(\alpha_k Z) \tag{16}$$

where,

$$\alpha_i = i\pi;\ \alpha_j = j\pi;\ \alpha_k = k\pi;\ (i = 1, 2, 3, \ldots, j = 1, 2, 3, \ldots, k = 1, 2, 3, \ldots) \tag{17}$$

α_i, α_j and α_k are the eigen functions.

First of all, applying triple finite integral cosine transforms on boundary conditions as portrayed in Eq. (11) as follows:

$$\Pi_{1X|X=0} = \int_{X=0}^{L}\int_{Y=L/2}^{Y=+L/2}\int_{Z=0}^{Z=-L} \frac{\partial\theta}{\partial X}\cos(\alpha_i X)\cos\left(\alpha_j Y\right)\cos(\alpha_k Z)dXdYdZ \tag{18a}$$

$$\Pi_{2X|X=L} = \int_{X=0}^{L}\int_{Y=-L/2}^{Y=+L/2}\int_{Z=0}^{Z=-L} \frac{\partial\theta}{\partial X}\cos(\alpha_i X)\cos\left(\alpha_j Y\right)\cos(\alpha_k Z)dXdYdZ \tag{18b}$$

$$\Pi_{1Y|Y=L/2} = \int_{X=0}^{L}\int_{Y=-L/2}^{Y=+L/2}\int_{Z=0}^{Z=-L} \frac{\partial\theta}{\partial Y}\cos(\alpha_i X)\cos\left(\alpha_j Y\right)\cos(\alpha_k Z)dXdYdZ \tag{18c}$$

$$\Pi_{2Y|Y=+L/2} = \int_{X=0}^{L}\int_{Y=L/2}^{Y=+L/2}\int_{Z=0}^{Z=-L} \frac{\partial\theta}{\partial Y}\cos(\alpha_i X)\cos\left(\alpha_j Y\right)\cos(\alpha_k Z)dXdYdZ \tag{18d}$$

$$\Pi_{1Z|Z=-L/2} = \int_{X=0}^{L}\int_{Y=-L/2}^{Y=+L/2}\int_{Z=0}^{Z=-L} \frac{\partial\theta}{\partial Z}\cos(\alpha_i X)\cos\left(\alpha_j Y\right)\cos(\alpha_k Z)dXdYdZ \tag{18e}$$

$$\Pi_{2Z|Z=+L/2} = \int_{X=0}^{L}\int_{Y=-L/2}^{Y=+L/2}\int_{Z=0}^{Z=-L} \frac{\partial\theta}{\partial Z}\cos(\alpha_i X)\cos\left(\alpha_j Y\right)\cos(\alpha_k Z)dXdYdZ \tag{18f}$$

Π is the transformed function declared above in Eq. (18).

Now implementing triple finite integral cosine transform on Eq. (9) w.r.t. 'X' gives:

$$\begin{aligned}
&\int_{X=0}^{L}\int_{Y=L/2}^{Y=+L/2}\int_{Z=0}^{Z=-L} \frac{\partial^2\theta}{\partial X^2}\cos(\alpha_i X)\cos\left(\alpha_j Y\right)\cos(\alpha_k Z)dXdYdZ\\
&+\int_{X=0}^{L}\int_{Y=-L/2}^{Y=+L/2}\int_{Z=0}^{Z=-L} \frac{\partial^2\theta}{\partial Y^2}\cos(\alpha_i X)\cos\left(\alpha_j Y\right)\cos(\alpha_k Z)dXdYdZ\\
&+\int_{X=0}^{L}\int_{Y=-L/2}^{Y=+L/2}\int_{Z=0}^{Z=-L} \frac{\partial^2\theta}{\partial Z^2}\cos(\alpha_i X)\cos\left(\alpha_j Y\right)\cos(\alpha_k Z)dXdYdZ\\
&+\mathrm{Ve_T}\int_{X=0}^{L}\int_{Y=-L/2}^{Y=+L/2}\int_{Z=0}^{-L}\left[\frac{\partial^2\theta}{\partial X^2}+\frac{\partial^2\theta}{\partial Y^2}+\frac{\partial^2\theta}{\partial Z^2}\right]\cos(\alpha_i X)\cos\left(\alpha_j Y\right)\cos(\alpha_k Z)dXdYdZ\\
&-\int_{X=0}^{L}\int_{Y=L/2}^{Y=t}\int_{X=0}^{Z=-L} \frac{\partial\theta}{\partial F}\cos(\alpha_i X)\cos\left(\alpha_j Y\right)\cos(\alpha_k Z)dXdYdZ\\
&-\mathrm{Ve_q^2}\int_{X=0}^{L}\int_{Y=-L/2}^{Y=+L/2}\int_{Z=0}^{Z=-L} \frac{\partial^2\theta}{\partial F^2}\cos(\alpha_i X)\cos\left(\alpha_j Y\right)\cos(\alpha_k Z)dXdYdZ = 0
\end{aligned} \tag{19}$$

After certain mathematical operations, the simplified form of Eq. (19) can be written as:

$$-i^2\pi^2\theta' + \frac{\partial^2\theta'}{\partial Y^2} + \frac{\partial^2\theta'}{\partial Z^2} - i^2\pi^2 Ve_T \frac{\partial\theta'}{\partial F} + Ve_T \frac{\partial}{\partial F}\left(\frac{\partial^2\theta'}{\partial Y^2} + \frac{\partial^2\theta'}{\partial Z^2}\right) - \frac{\partial\theta'}{\partial F} - Ve_9 \frac{\partial^2\theta'}{\partial F^2} = 0 \tag{20}$$

where,

$$\theta'(i, Y, Z, F) = \int_{X=0}^{L} \theta(X, Y, Z, F)\cos(i\pi X)dX \tag{21}$$

$\theta'(i, Y, Z, F)$ is the transformed temperature based on FIT w.r.t 'X'.

Following same procedure as presented in Eq. (19), finite integral transform method has been implemented on Eq. (20) and the simplified final form can be represented as follows:

$$Ve_q \frac{d^2\theta'''}{dF^2} + \left(i^2\pi^2 Ve_T + j^2\pi^2 Ve_T + k^2\pi^2 Ve_T + 1\right)\frac{d\theta'''}{dF} + \left(i^2\pi^2 + j^2\pi^2 + k^2\pi^2\right)\theta''' = 0 \tag{22}$$

$$\theta'''(i, j, k, F) = \int_{z=0}^{Z=-L} \theta''(i, j, Z, F)\cos(k\pi Z)dZ \tag{23}$$

$\theta'''(i, j, k, F)$ is the transformed temperature based on FIT w.r.t 'Z'.

Here it can be noted that Eq. (22) is a 2nd order ordinary differential equation with homogeneous form. This can be achieved by employing integral transform scheme and based on universal theorems of such differential equation; the solution can be easily achieved [42]. Also the solution will be achieved by Duhamel's theorem and the standard solution methodology can be represented as follows [44]:

$$\theta(X, Y, Z, F) = \int_{\widetilde{F}=0}^{\widetilde{F}=F} \theta(X, Y, Z, F : \widetilde{F})d\widetilde{F} \tag{24}$$

Hence applying Eq. (13) coupled with Eq. (24) on Eq. (22), the final structure of three-dimensional transient temperature response based on DPL heat conduction model influenced by moving laser source is as follows:

1st case: *for two different real roots*

$$\left(i^2\pi^2 Ve_T^2 + j^2\pi^2 Ve_T^2 + k^2\pi^2 Ve_T^2 + 1\right)^2 - 4Ve_q\left(i^2\pi^2 + j^2\pi^2 + k^2\pi^2\right) > 0$$

$$\theta(X, Y, Z, F) = 8\sum_{i=0}^{\infty}\sum_{j=0}^{\infty}\sum_{k=0}^{\infty}\left[\frac{A}{J}\Omega\exp(IF)\sinh(JF)\cos(i\pi X)\cos(j\pi Y)\cos(k\pi Z)\{1 - F\exp(-F) - \exp(-F)\}\right] \tag{25a}$$

2nd case: *for two repeated roots*

$$\left(i^2\pi^2 Ve_T^2 + j^2\pi^2 Ve_T^2 + k^2\pi^2 Ve_T^2 + 1\right)^2 - 4Ve_q\left(i^2\pi^2 + j^2\pi^2 + k^2\pi^2\right) = 0$$

$$\theta(X, Y, Z, F) = 8 \sum_{i=0}^{\infty} \sum_{j=0}^{\infty} \sum_{k=0}^{\infty} \left[\begin{matrix} A\Omega \exp(IF) \cos(i\pi X) \cos(j\pi Y) \cos(k\pi Z) \\ \{1 - F\exp(-F) - \exp(-F)\} \end{matrix} \right] \quad (25b)$$

3rd case: *for no real roots*

$$\left(i^2\pi^2 Ve_T^2 + j^2\pi^2 Ve_T^2 + k^2\pi^2 Ve_T^2 + 1\right)^2 - 4Ve_q\left(i^2\pi^2 + j^2\pi^2 + k^2\pi^2\right) < 0$$

$$\theta(X, Y, Z, F) = 8 \sum_{i=0}^{\infty} \sum_{j=0}^{\infty} \sum_{k=0}^{\infty} \left[\begin{matrix} \frac{A}{J}\Omega \exp(IF) \sin(JF) \cos(i\pi X) \cos(j\pi Y) \cos(k\pi Z) \\ \{1 - F\exp(-F) - \exp(-F)\} \end{matrix} \right] \quad (25c)$$

where,

$$\begin{cases} I = -\frac{\left(i^2\pi^2 Ve_T^2 + j^2\pi^2 Ve_T^2 + k^2\pi^2 Ve_T^2 + 1\right)}{2Ve_q} \\ J = \frac{\sqrt{\left(i^2\pi^2 Ve_T^2 + j^2\pi^2 Ve_T^2 + k^2\pi^2 Ve_T^2 + 1\right)^2 - 4Ve_q\left(i^2\pi^2 + j^2\pi^2 + k^2\pi^2\right)}}{2Ve_q} \\ \Omega = \frac{\{\cos(i\pi) - 1\}\{\cos(j\pi) - 1\}\{\cos(k\pi) - 1\}}{i^2\pi^2 j^2\pi^2 k^2\pi^2} \end{cases} \quad (26)$$

4 Results and Discussion

The thermo-mechanical behaviour evolved in laser surface processing applications is much efficient to produce designed output but the physical significance behind the heat treatment and its phenomenological effects on surface morphology, grain structure, hardness, variation of several mechanical properties must constantly monitored to develop quality of product. The thermal behaviour study is much more essential as this is the significant source of surface processing. As laser irradiance is being imposed on the substrate material and due to moving heat source the heat affected zone is being developed and desired surface processing is achieved. Hence the control of moving heat source is important for accomplishment of desired outcome. In this book chapter, the developed analytical solution of 3-D moving laser heat source (refer Eq. (25)) has been coded in in-house FORTRAN 90 software for creation of graphical analysis.

Figure 3 depicts the 3-D thermal response with temporal coordinate (refer Eq. (25)) in square cuboid shaped plate considered in present analysis for two different locations. The corresponding process variables are: $t_p = 150$ s and thermal relaxation time lags are $\tau_q = 7$ s and $\tau_T = 0.65$ s. The other thermophysical parameters are scripted in Table 1. It has been noticed in Fig. 3 that temperature increases from 40 °C (initial condition of the plate, assumed in present analysis) and after attaining a peak magnitude it falls then again it increases a smaller peak and then gradually attains thermal equilibrium. The physical significance of such peak is introduction

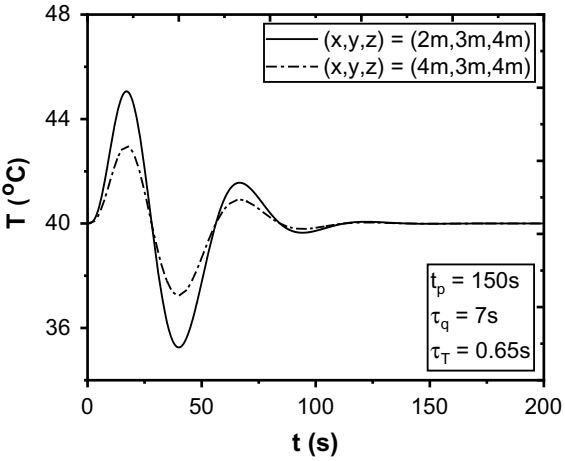

Fig. 3 Thermal response with temporal co-ordinate for two different locations in the physical domain

Table 1 Thermophysical process variables in present analysis [32]

L_0 (Jm^{-3})	R_a	α (m^2s^{-1})	k ($Wm^{-1}°C^{-1}$)	l (m)	v (ms^{-1})	T_0 (°C)
1.465×10^{10}	0.93	1.1643×10^{-4}	400	5	0.5	40

of dual phase lagging behaviour in the heat conduction model. Basically it is purely controlled by lagging behaviour where τ_q attributes for waveform behaviour and τ_T quantifies for diffusion characteristics [45]. Here $\tau_q > \tau_T$ and hence it is expected to behave as hyperbolic nature in its initial stages of heat conduction and the same nature of temperature distribution has been observed. From Fig. 3 it is also found that at the location of (2, 3, 4 m), the peak temperature is higher than the location of (4, 3, 4 m) as the previous location is nearer to the moving heat source (starting point) and latter one is comparatively away from the source zone. Hence DPL heat conduction model is bit differ than the conventional heating and cooling cycle for $\tau_q > \tau_T$.

Figure 4 delineates the temperature variation with temporal coordinate in physical domain at particular location (3, 3, 3 m) for two different set of thermal relaxation time lags. To investigate thermal response in DPL heat conduction, the selection of thermal relaxation times is decisive. The attenuation of peak temperature sharply depends on its selection. It has been observed in Fig. 4 that for $\tau_q = 4$ s, $\tau_T = 0.75$ s, the peak temperature is 91.05 °C while for $\tau_q = 3$ s, $\tau_T = 0.55$ s, the peak temperature is 76.77 °C. The combined form of wavelike and diffusion heat flow stands behind such thermal behaviour. Both heating and cooling cycle of laser moving heat source is influenced by this phenomena.

Figure 5 illustrates the thermal response with temporal coordinate at specific location (3, 3, 3 m) in the plate for two different laser power density L_0 with corresponding process parameters of $t_p = 150$ s, $\tau_q = 4.5$ s, $\tau_T = 0.85$ s. Selection of laser power density (refer Eq. (6)) is crucial as because of this entire surface processing depends.

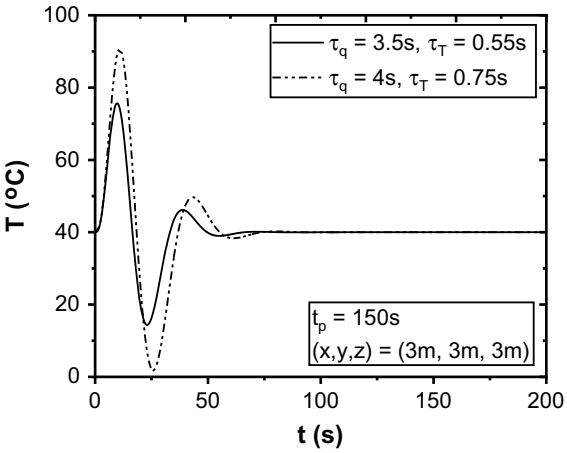

Fig. 4 Thermal response with temporal co-ordinate for two different thermal relaxation times (for heat flux) at a specific location

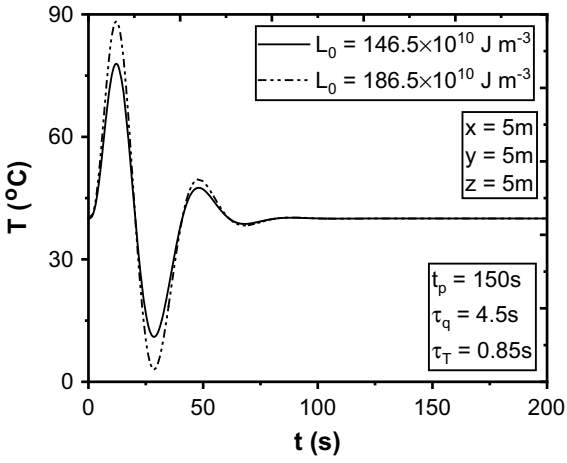

Fig. 5 Temperature variation with temporal co-ordinate for two different laser power densities imposed on the domain at particular location

It is distinct fact that if laser power density increase, peak temperature also rises and the similar development has been experienced in Fig. 5. Hence from the view point of physical significance of laser heating, present mathematical modelling along with in-house computer codes (developed in FORTRAN) have been justified.

Figure 6 exhibits the temperature distribution in substrate plate with laser exposure time (t_p) as introduced in Eq. (6) at specific location for three different τ_q with constant τ_T (0.85 s). The time of heating is kept as 10 s. It can be realized that laser exposure time can never be zero as it is not imaginable in case of moving heat source with fixed velocity (refer Table 1). Hence the initial laser time exposure is kept at 100 s in this analysis. It has been already discussed that if magnitude of τ_q increases, waveform behaviour is to be detected and peak temperature will be raised. For $\tau_q = 3$ s, $\tau_q = 4$ s and $\tau_q = 5$ s, the peak temperature is found as 2335.12 °C,

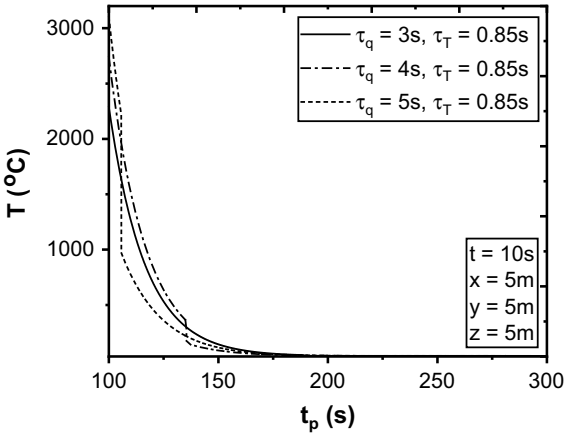

Fig. 6 Temperature variation with laser exposure time (t_p) for three different thermal relaxation time lags imposed on the domain at particular location

2776.86 °C and 3001.88 °C respectively. As laser exposure time increases temperature gradually falls and become similar at $t_p = 187.38$ s. Hence the spectrum of laser exposure time has been found from present analysis (with particular general set of process variables) as 100–200 s.

Figure 7 highlights the two-dimensional surface contours (developed by using SIGMAPLOT tool with in-house code in FORTRAN) of temperature proliferation in the substrate material. Development of such contours helps to understand the heat flow in the substrate material as due to heating, metallurgical changes occur in case of material processing. In Fig. 7, temperature pattern has been created in different spatial directions. For this study the constant process parameters are: $\tau_q = 3.5$ s, $\tau_T = 0.15$ s and $t = 60$ s. Figure 7a, b denotes the temperature variation along x-y direction (with specific location of $z = 3$ m) for two different t_p. The starting point of laser source is recognized and the along the x-direction temperature gradually falls. The focal point of laser source temperature varies depending upon the magnitude of t_p. Higher the t_p, raise in temperature is observed along the variation of two spatial directions. In Fig. 7c, d, thermal contours have been generated along x–z direction and same phenomena have been observed as in case of x–y direction but with different temperature. In Fig. 7e, f, along y-z direction (with fixed location along x-direction), thermal isotherms have been established. This result has indicated the spherical projection of laser source utilized in present mathematical modelling imposed on metallic substrate.

The surface contours provides the accuracy and efficacy of present mathematical solution subjected to 3-D DPL heat conduction model under the influence of laser irradiance on substrate material. The information of thermal history combining both heating and cooling cycles in laser processing of material would be helpful for design and optimization of process variables in laser processing of materials.

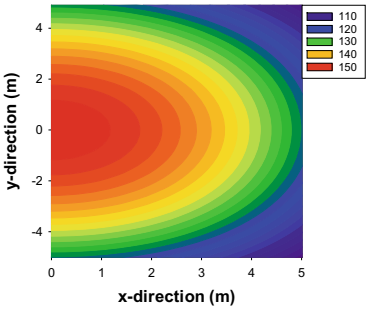

(a) t = 60s, t_p = 120s, τ_q = 3.5s, τ_T = 0.15s, z = 3m

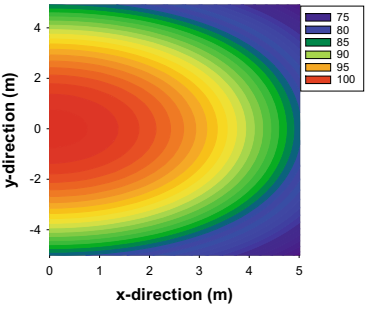

(b) t = 60s, t_p = 100s, τ_q = 3.5s, τ_T = 0.15s, z = 3m

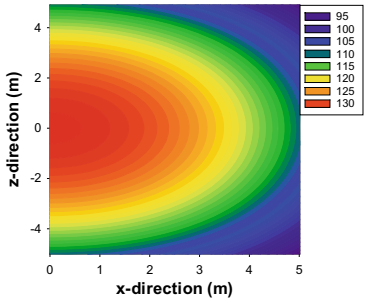

(c) t = 60s, t_p = 120s, τ_q = 3.5s, τ_T = 0.15s, y = 3m

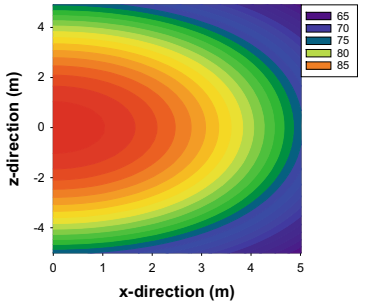

(d) t = 60s, t_p = 100s, τ_q = 3.5s, τ_T = 0.15s, y = 3m

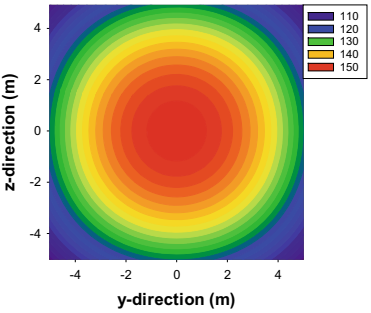

(e) t = 60s, t_p = 120s, τ_q = 3.5s, τ_T = 0.15s, x = 3m

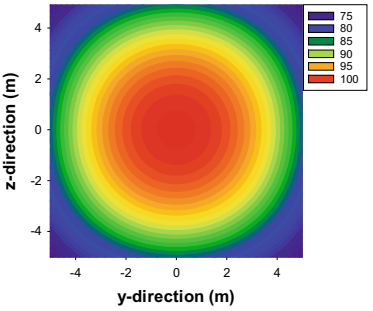

(f) t = 60s, t_p = 100s, τ_q = 3.5s, τ_T = 0.15s, x = 3m

Fig. 7 2-D surface thermal isotherms (°C) developed in two different directions for different transient response time, laser exposure and thermal relaxation time lags

5 Conclusion

Based on the research work fabricated in this book chapter, the concluding remarks can be summarized as follows:

(a) For the first time, 3-D DPL heat conduction model has been solved under the laser irradiance on metallic substrate. The exact analytical solution has been developed based on hybrid form of 'Finite integral transform' and 'Duhamel's theorem'. The present mathematical modelling justifies the physical phenomena of laser processing (moving heat source) of materials in terms of thermal behaviour.
(b) Estimation of thermal behaviour with DPL heat conduction model subjected to laser processing highly influenced by selection of thermal relaxation time lags (τ_q and τ_T). An amalgamation of hyperbolic and diffusion behaviour has been observed in development of thermal history.
(c) Two important laser processing variables have been found as major impact on temperature response viz. laser power density (L_0) and duration of laser exposure (t_p). Power density as well as laser exposure both define the peak temperature during laser movement.
(d) The surface isotherms point out that with increase in laser exposure, the focal point temperature of laser heat source increases along the two specific directions.

Conflict of interest The authors have declared no conflict of interest.

References

1. Bäuerle, D.: Laser Processing and Chemistry. Springer, Berlin (2000)
2. Schaff, P.: Laser Processing of Materials: Fundamentals, Applications and Developments. Springer, Berlin, Heidelberg (2010)
3. Dowden, J.M.: The Mathematics of Thermal Modelling: An Introduction to the Theory of Laser Material Processing. Chapman & Hall/CRC (2001)
4. Yilbas, B.: Laser Heating Applications: Analytical Modelling. Elsevier (2012)
5. Heller, J., Bartha, J.W., Poon, C.C., Tam, A.C.: Temperature dependence of the reflectivity of silicon with surface oxide at wavelengths of 633 and 1047 nm. Appl. Phys. Lett. **75**(1), 41–43 (1999)
6. Brown, M.S., Arnold, C.B.: Fundamentals of Laser-Material Interaction and Application to Multiscale Surface Modification. Springer, Berlin, Heidelberg (2000)
7. Yilbas, B.S., Al-Dweik, A.Y., Al-Aqeeli, N., Al-Qahtani, H.M.: Laser Pulse Heating of Surfaces and Thermal Stress Analysis. Springer International Publishing, Switzerland (2014)
8. Maiman, T.H.: Stimulated optical radiation in ruby. Nature **187**(4736), 493–499 (1960)
9. Fourier, J.: The Analytical Theory of Heat. Cambridge University Press, Cambridge Warehouse, London (1878)
10. Arpaci, V.S.: Conduction Heat Transfer. Addison-Wesley Pub. Co., the University of Michigan, Addisson Wesley Pub (1966)
11. Qiu, T.Q., Tien, L.: Femtosecond laser heating of multi-layer metals—I analysis. Int. J. Heat Mass Transf. **37**, 2789–2797 (1994)

12. Yilbas, B.S., Apalak, K.: The basic concepts of heat transfer mechanism during laser drilling of metals. Egypt J. Phys. **18**(1), 25–34 (1987)
13. Yilbas, B.S., Kalyon, M.: Formulation of laser pulse heating: a closed form solution including heating and cooling cycles with pulse parameter variation. Laser Eng. **14**(3–4), 213–228 (2004)
14. Yilbas, B.S.: Analytical solution for time unsteady laser pulse heating of semi-infinite solid. Int. J. Mech. Sci. **39**(6), 671–672 (1997)
15. Yilbas, B.S.: 3-Dimensional laser heating model including a moving heat source consideration and phase change process. Heat Mass Transf. **33**, 495–505 (1998)
16. Yilbas, B.S., Kalyon, M.: Analytical solution for pulsed laser heating process: convective boundary condition case. Int. J. Heat Mass Transf. **45**, 1571–1582 (2002)
17. Yilbas, B.S., Pakdemirli, M., Mansoor, S.B.: Analytical solution for temperature field in thin film initially heated by a short-pulse laser source. Heat Mass Transf. **41**, 1077–1084 (2005)
18. Kalyon, M., Yilbas, B.S.: An approach for analytical solution pertinent to lattice temperature variation due to laser short-pulse heating. Heat Mass Transf. **42**, 1111–1117 (2006)
19. Hsiao, F.B., Jen, C.P., Wang, D.B., Chuang, C.H., Lee, Y.C., Liu, C.P., Hsu, H.J.: An analytical modeling of heat transfer for laser-assisted nanoimprinting processes. Comput. Mech. **37**, 173–181 (2006)
20. Bouaziz, M.N., Boutalbi, N.: Laser heating of a material with time-dependent laser source. Int. J. Thermophys. **32**, 1047–1059 (2011)
21. Yilbas, B.S., Al-Dweik, A.Y., Mansour, S.B.: Analytical solution of hyperbolic heat conduction equation in relation to laser short-pulse heating. Phys. B **406**, 1550–1555 (2011)
22. Yilbas, B.S., Al-Dweik, A.Y.: Short-pulse heating and analytical solution to non equilibrium heating process. Phys. B **417**, 28–32 (2013)
23. Qi, H.T., Xu, H.Y., Guo, X.W.: The Cattaneo-type time fractional heat conduction equation for laser heating. Comput. Math. Appl. **66**, 824–831 (2013)
24. Zhang, L., Shang, X.: Analytical solution to non-Fourier heat conduction as a laser beam irradiating on local surface of a semi-infinite medium. Int. J. Heat Mass Transf. **85**, 772–780 (2015)
25. Peng, Q.: An analytical solution for a transient temperature field during laser heating a finite slab. Appl. Math. Model. **40**, 4129–4135 (2016)
26. Chen, G., Wang, Y., Zhang, J., Bi, J.: An analytical solution for two-dimensional modeling of repetitive long pulse laser heating material. Int. J. Heat Mass Transf. **104**, 503–509 (2017)
27. Kashani, M.M., Movahhedy, M.R., Ahmadian, M.T.: Analytical solution of transient three-dimensional temperature field in a rotating cylinder subject to a localized laser beam. J Heat Transf. **139**, 062701–1–062701–8 (2017)
28. Chen, G.: Semi-analytical solutions for 2-D modeling of long pulsed laser heating metals with temperature dependent surface absorption. Optik **132**, 46–51 (2017)
29. Chen, G., Bi, J.: Analytical solutions for three-dimensional modeling of temperature rise inside solid material induced by laser irradiation. Optik **132**, 80–88 (2017)
30. Chen, G.: Axisymmetric modeling of long pulsed laser heating with convective boundary conditions using analytical solutions. Optik **130**, 1038–1044 (2017)
31. Feng, S., Huang, C., Wang, J., Zhu, H., Yao, P., Liu, Z.: An analytical model for the prediction of temperature distribution and evolution in hybrid laser-waterjet micro-machining. Prec. Eng. **47**, 33–45 (2017)
32. Ma, J., Sun, Y., Yang, J.: Analytical solution of dual-phase-lag heat conduction in a finite medium subjected to a moving heat source. Int. J. Therm. Sci. **125**, 34–43 (2018)
33. Dutta, J., Kundu, B.: Two-dimensional closed-form model for temperature in living tissues for hyperthermia treatments. J. Therm. Biol. **71**, 41–51 (2018)
34. Dutta, J., Kundu, B.: A revised approach for an exact analytical solution for thermal response in biological tissues significant in therapeutic treatments. J. Therm. Biol. **66**, 33–48 (2017)
35. Xu, F., Seffen, K.A., Liu, T.J.: Non-Fourier analysis of skin biothermomechanics. Int. J. Heat Mass Transf. **51**, 2237–2259 (2008)
36. Cattaneo, C.: A form of heat conduction equation which eliminates the paradox of instantaneous propagation. Compte. Rendus **247**, 431–433 (1958)

37. Vernotte, P.: Les paradoxes de la theorie continue de l' equation de la chaleur. Compte. Rendus **246**, 3154–3155 (1958)
38. Tzou, D.Y.: A unified field approach for heat conduction from macro- to microscales. J Heat Transf. **117**, 8–16 (1995)
39. Hooshmand, P., Moradi, A., Khezry, B.: Bioheat transfer analysis of biological tissues induced by laser irradiation. Int. J. Therm. Sci. **90**, 214–223 (2015)
40. Zhou, J., Zhang, Y., Chen, J.K.: An axisymmetric dual-phase-lag bioheat model for laser heating of living tissues. Int. J. Therm. Sci. **48**(8), 1477–1485 (2009)
41. Ma, J., Yang, X., Sun, Y., Yang, J.: Thermal damage in three-dimensional vivo bio-tissues induced by moving heat sources in laser therapy. Sci. Rep. (Nature) **9**, 10987 (2019)
42. Tzou, D.Y.: Macro- To Micro-Scale Heat Transfer: The Lagging Behavior (Chemical and Mechanical Engineering Series). CRC Press (1996)
43. Ozisik, M.N.: Heat conduction. Wiley, Canada (1976)
44. Hahn, D.W., Ozisik, M.N.: Heat conduction. Wiley, New Jersey (2012)
45. Dutta, J., Kundu, B.: Exact analysis based on BDLTNE approach for thermal behaviour in living tissues during regional hyperthermia therapy. Act. Mech. **230**, 2853–2871 (2019)

Surface Roughness and Morphology Studies on Machining Hybrid Composite Material Using Abrasive Water Jet Cutting Process

S. P. Jani, A. Senthil Kumar, M. Adam Khan, and M. Uthayakumar

Abstract The accelerated demands of engineered products with superior properties have inspired researchers to investigate the substitutes of the manmade fibre-based composites and explore the utilization of natural fibre based polymer matrix composites (PMC). Although manmade fibres have many benefits, but their decreasing usage in decade has been due to high primary cost, non-bio degradability, non-renewability, high energy ingestion in engineering process and unfavourable eco-friendly effects. Bio fibres still compensate for their deprived compatibility with the matrix, naturally high moisture absorption rate with their positive aspects like low cost, nonabrasive nature, low density, good thermal characterise, superior energy recovery and bio degradability. Hemp is an important fibre used for manufacture a variety of automobile parts, rope, yarn, household application etc. Therefore, researchers are investigating new zones for utilization of hemp fiber as in reinforcement polymer matrix composite (PMC). Kevlar fibre is used for hybridization purpose. NaOH treatment is used for improve the adhesion strength between the matrix and hemp fibre. The natural filler (palm and coconut shell powder 75–150 μ) materials are being added to increase the mechanical interlocking property and also the bonding strength between matrix and fibre. In this research, the hybrid natural fibre composite was developed by Hemp/Kevlar/filler. Four types of specimens were developed in various different combinations (i.e. 0, 5, 7.5, and 10%) of filler. The size of the filler material and fibre was measured using scanning electron microscope. The trimming (machining) of the composite is very challenging to attempt using conventional machining processes. Therefore, non-traditional machining process i.e. abrasive water jet cutting was attempted. For trimming (machining) of polymer composites, Abrasive Water Jet Machining (AWJM) is widely employed in manufacturing industries. In the current

S. P. Jani (✉)
Department of Mechanical Engineering, Marrilaxman Reddy Institute of Technology and Management, Hyderabad 500043, India
e-mail: spjani10@gmail.com

A. Senthil Kumar
Department of Mechanical Engineering, Sethu Institute of Technology, Virudhunagar, India

M. Adam Khan · M. Uthayakumar
School of Automotive and Mechanical Engineering, Kalasalingam Academy of Research and Education, Krishnankoil, Tamil Nadu, India

K. Gupta (ed.), *Surface Engineering of Modern Materials*, Engineering Materials,
https://doi.org/10.1007/978-3-030-43232-4_6

research, kerf tapper, surface roughness (Ra) and the material removal rate (MRR) were examined under the influence of input factors such as Jet Pressure, nozzle Speed and Stand of Distance (SOD). Taguchi L_9 orthogonal array based experimental study conducted. From the analysis, the nozzle speed was found the most significant factor. But, the jet pressure was always influenced by kerf wall inclination. The SEM image has been shown fibre pull out, filler distribution in a matrix and helps to understand the surface morphology of the fractured surface during trimming (machining).

Keywords Natural fibre · Composite · Machining · Abrasive · Wear · Roughness

1 Introduction

The future demands and market for natural fibre based composites will be very high due to their superior properties to claim their usage in making the engineered parts and components for automotive, defense, and space research [1]. While manufacturing products from polymer matrix composite material, it undergoes extensive machining operations. Cutting and trimming of polymer matrix composite material using conventional machining method is particularly hard and leads to high initial cost [2]. The mechanical properties are heterogeneous and invariable throughout the structure. Abrasive water jet cutting (AWJC) can be a prominent substitute of conventional processes to machine polymer matrix composite machining [3].

Especially polymer matrix composite (PMCs) materials play vital role in some special merits such as excellent fatigue tolerance, minimal cost, high modulus-to-weight ratio, good impairment acceptance, high quality and high strength-to-weight ratio. Moreover, polymer matrix composite (PMCs) materials these have some particular restrictions such as low working temperatures, high thermal and moisture co-efficient and low elastic property in transverse direction [1, 2]. High tool tear, delamination problems, and high machining temperature etc. are the major problems occurred in conventional machining of these composites. Better machinability in general is achieved by minimizing the delamination during high production rates and minimizing tool damages like wear and tear. It is often very difficult in cutting and trimming of composites by using traditional machining technique because of increase in production cost due to high consumption of energy and resources [4].

As far as AWJM of composites is concerned, the type of abrasives, traverse rate, standoff distance and hydraulic jet pressure, are more important process parameters as compared to other process parameters such as size of abrasive grain, mass flow rate of abrasive particle, and impact angle to achieve good quality of surface finish. But in the machining of PMCs mainly laminated composites, delamination is most important composite defect. While AWJM of composites, abrasive water jet (AWJM) creates shock wave impact on surface of the material because of which crack tips are created in the work piece material at preliminary cutting stage. Now the high pressurized AWJM penetrates into the crack tips which tend to water hammering effect [5].

Schwartzentrber et al., expected the surface finish (Ra) by expanding model considering the contact of abrasive on the prepared composite, from the results it is concluded that the abrasive flow rate has major contribution on the surface finish of the FRP composite [6]. Miron et al. studied cutting performance of PMCs. In their work, only surface roughness is considered because quality of product not reflected to other parameters like kerf tapper and material removal rate (MRR) [7]. Azmir et al. studied AWJM of Kevler composite laminates. During machining, four different input process parameters such as nozzle speed, abrasive particle flow rate, hydraulic pressure, and SOD were considered. Optimization of these four different process parameters with consideration of various performance characteristics was carried out [8]. Ahmed et al. did experimental work on the influence of nozzle angle and impact of velocity on the surface roughness, delamination, and material removal rate. They concluded that the nozzle angle is given more impact in output parameters [9]. Narayanan et al. designed a mathematical model to determine the surface finish in AWJM machining including the size of abrasive particle and nozzle speed [10].

2 Materials and Method

In this present work, the objective is to study the machinability of AWJC while machining polymer matrix composite. The polymer matrix with various wt% (0, 5, 7.5, and 10%) of natural filler composite was prepared by compression molding method. The machinability studies were done in AWJM with various different input parameters of pump pressure, nozzle speed and standoff distance (SOD). Measurement, testing, characterization were done using image analyzer, Scanning Electron Microscopy (SEM), and surface roughness tester.

2.1 Development of Composite

The Kevlar (syntactic) fibre and hemp (natural) fibre are the fibre reinforcement; the naturally available palm shell and coconut shell in the form of powder as filler material; and epoxy as a matrix material. The Kevlar fibre is otherwise called aramid fibre. The fibres are designated based on the property. In this research, Kevlar 149 is selected as one of the fibre reinforcements under syntactic type. The properties of the Kevlar fibre are in Table 1. Its merits are less density compare to other materials, high tensile strength at low cost and high suddenly impact resistance. Thus, these fibres are highly recommended for defence and aerospace industries.

Hemp is one of the best reinforcements for polymer composite under the natural fibre category. Hemp was derived from the Cannabis tree family which is available and collected from the rural areas of West Bengal. The raw fibres are chemically treated with 5% of NaOH and keep at room temperature for 6 h to the fibre. After that treated fibres are washing in running water. After treatment these fibres are strained

Table 1 Properties of Aramid fibre

Sl. no	Properties	Value
1	Size of the fibre	60 μ
2	Hardness of the fibre	85 RHN
3	Fibre density	1.47 (G/cm^3)
4	Modulus	179 Gpa
5	Strength	3450 Mpa
6	Elongation	2.5%

and showing to sunlight for 12–36 h to remove the vapour, and organic impurities from the surface of the natural fibre. This process will improve the surface quality, fibre properties and provides better bond with the matrix. The chemical composition and properties of hemp fibre is show in Tables 2 and 3. The SEM micrograph of the fibre and the EDS result of the sample show carbon and oxygen as dominating element were shown in Figs. 1 and 2.

Composite materials naturally have many good properties like strength, modules, hardness, and impact strength. But the delamination is one of the most found weaknesses of the polymer composite materials. To avoid this fault, some filler material is added in composite fabrication. This filler is used to increase the interlocking strength of the composite. In this present study, natural palm shell and natural coconut shell powder are used as filler material (proportions are same wt%).

Coconut and Palm shells are collected from the farm of south Tamilnadu (Kanyakumari). These shells are involved in pulverizing by using a hammer. After this process, shells are converted to small pieces. At the next stage, these small pieces are subjected to a crushing machine that is used to convert the small pieces to powder form. The sieve analyser is used to separate the required size. This sieve analysis

Table 2 Chemical combination of hemp fibre

Sl. no	Elements	wt%
1	Cellulose	68
2	Hemicellulose	15
3	Lignin	10
4	Waxes	0.8

Table 3 Properties of hemp fibre

Sl. no	Property	Value
1	Size of the fibre	60 μ
2	Fibre density	1.48 (g/cm^3)
3	Modulus	2.9 GPa
4	Strength	690 MPa
5	Elongation	1.6%

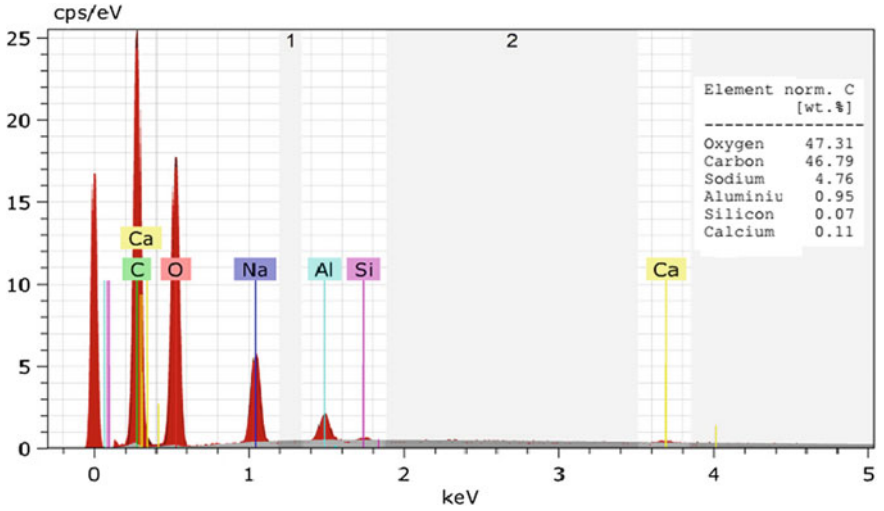

Fig. 1 EDS analysis of hemp fibre after 5% NaOH Treatment

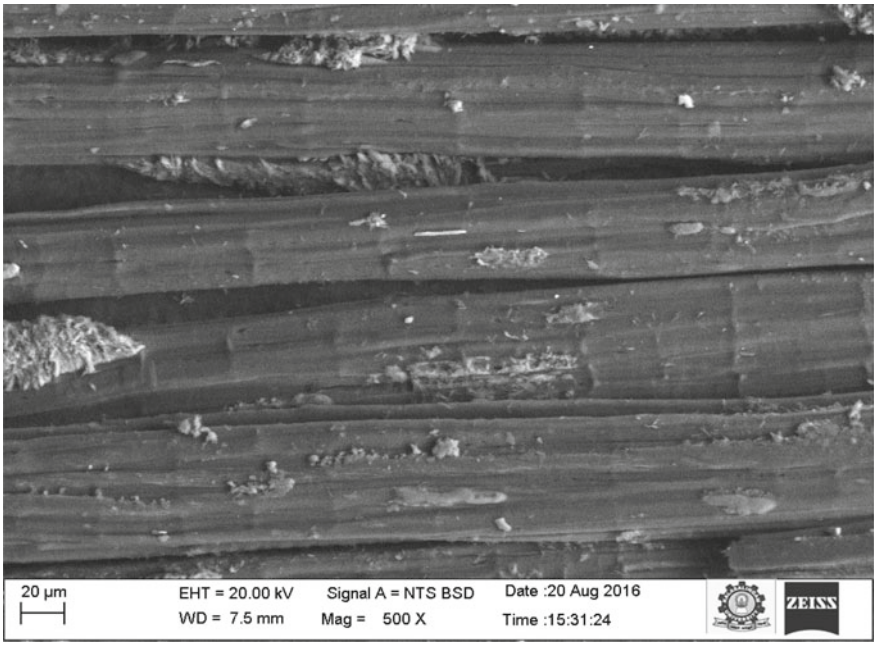

Fig. 2 SEM image of a hemp fibre

followed by the pulverizing and crushing process. This process is made by laboratory, after this process, the fillers rage is separated in 75–150 μ size. These fillers are subjected to the chemical treatment process, in this process, 5% of NaOH dissolved in a litre of distilled water and has undergone for 6 h at normal room temperature. After treatment, the fillers are sifted and exposed to sunlight (at least 12–24 h) to remove the vapour content. Afterward, these dried fillers are subjected to heat treatment process, in this process fillers are heated at 120 °C for 3 h in a muffle furnace. This heat treatment process is used to increase the mechanical strength of the fillers. The treated fillers materials SEM micrograph is shown in Fig. 3.

Due to the excellent properties of epoxy like good adhesion, mechanical strength, low vapour content, and little shrinkage etc.; it is used to make best matrix materials for composites. The epoxy matrix is purchased from local araldite market. The epoxy grade LY536 and the hardener grade HY951 are used as matrix to develop a composite. Figure 4 shows the chemical bonding of the matrix material. The araldite (epoxy) and hardener were mixed in the predefined ratio of 10:1 (as per manufacturing data). It is mixed by mechanical agitator. The araldite is cured in simple atmospheric and room temperature for 3–4 h.

The composites are mostly fabricated through compression moulding and hand layup method. In the proposed research, the hybrid composite was manufactured through compression moulding process. The arrangement of the composite layers in moulding is shown in Fig. 5. The lab prepared natural hemp fibre, Kevlar 149, palm and coconut shell powder as fillers are used to prepare composite with epoxy resin as a matrix. The samples are moulded near to the required size of the investigation. The moulding process was followed from cleaning the mould and brushed with wax as relaxing agent. The mica sheets are used as barrier between the mould and composite for easy removal. The size of the mould plate is 300 × 170 mm.

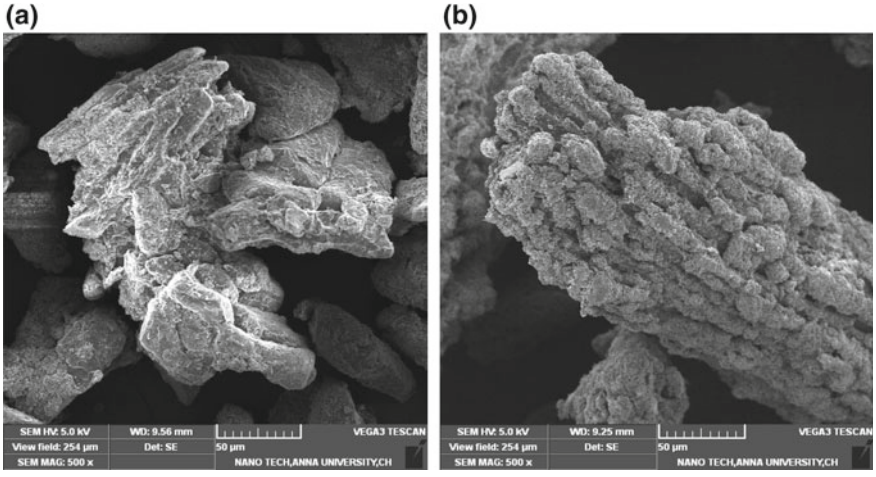

Fig. 3 SEM images of filler material **a** coconut shell powder and **b** palm shell powder

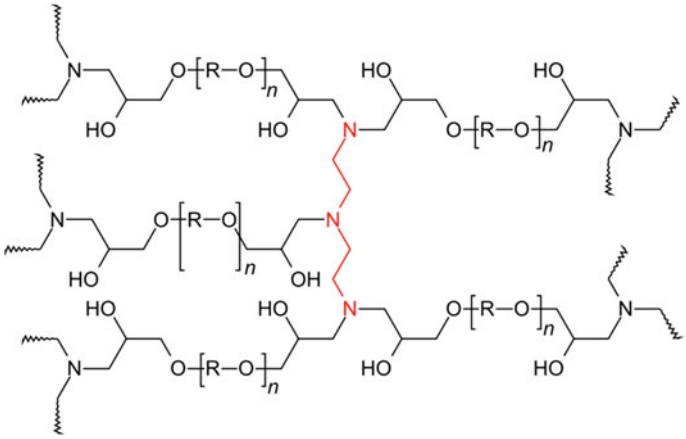

Fig. 4 Epoxy resin cross link

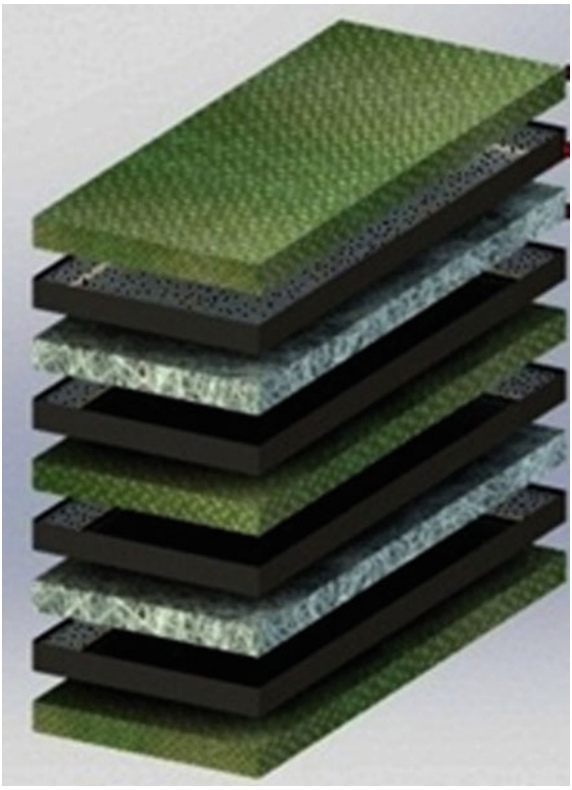

Fig. 5 Design of proposed layers in work

Table 4 Different Sample ID's with their components (wt%) ratio

Sample id	Components			
	Kevlar (wt%)	Hemp (wt%)	Filler (wt%)	Epoxy (wt%)
Without filler	6	24	0	70
With filler 5%	6	24	5	65
With filler 7.5%	6	24	7.5	62.5
With filler 10%	6	24	10	60

The combination of the specimens varied with reference to the proportion (wt%) of the filler material. Four different types of combinations are fabricated with and without filler. The proportions of the specimens are given in the Table 4. The hemp fibre orientation was maintained at 0°/90° parallel to Kevlar 149. The arrangement of the fibre filler and matrix was designed using modelling tool for understanding the composite structure. The matrix and bio fillers (palm and coconut shell filler) in a predefined ratio are used to blend with a mechanical agitator for 5–8 min with a purpose to avoid air bubbles/blow holes during curing. During fabrication the reinforcement, filler and the matrix are placed in the mould and subjected to 35–40 psi compression and maintain for 8 h for curing.

2.2 Abrasive Water Jet Cutting of Composites

The machining studies of the hybrid composites is performed on abrasive water jet machine (Model: DWJ1313/FB). Figure 6 shows the complete photograph of the AWJ machine. The range of variable machining parameters are- jet pressure 200–260 MPa, nozzle cross feed (traverse speed) 20–40 mm/min and stand-off distance 1–3 mm. The garnet with a particle size of 80 mesh is used for cutting process. The cutting was performed at an angle of 90° with a flow rate of 2–3 g/min.

Using the above parameters, the composites are machined to analyze the response. Machined samples with reference to the composition of filler are given in Fig. 7. Surface roughness, Material Subtraction Rate and Kerf taper were the three important machinability indicators. The kerf taper was calculated with the following empirical relation.

$$Kerf\ Taper = \frac{w_t - w_b}{2t} \tag{1}$$

where,

w_t top width,
w_b bottom width and
t Thickness of the sample

Fig. 6 Photo image of AWJM machine

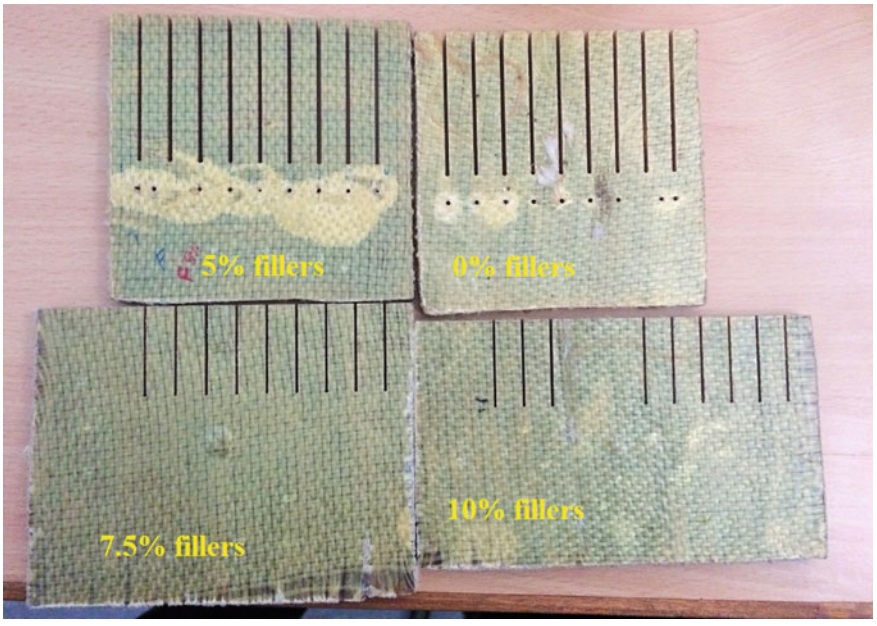

Fig. 7 Photos of natural fibre composite with and without fillers after AWJ cutting

The Material Subtraction Rate for abrasive water jet cutting is calculated based on the kerf taper, nozzle speed, and depth of penetration of the water jet nozzle. The amount of material removed during cutting depends on the behavior of the abrasive particles and its mechanical properties. The stimulation of abrasive behavior was supported by the jet pressure and its dimensional property. The removal of material can be calculated with the following mathematical equation.

$$MRR = h_t d_i v_f \tag{2}$$

where,

h_t the thickness of job to be penetrated
d_i nozzle orifice dimension [$d_i = (W_t + W_b)/2$],
v_f jet cross feed.

The electron microscope is used to study the surface morphology of the machined composite material. From the electron micrographs, the wear mechanism and the composite behavior are identified. As a result, the AWJ process was justified for cutting composite. The main objective of this work was to minimize the unit production cost of the machining process. Selection of machinability parameter plays a major role with different machine constraints to optimize the unit production cost. There are many machining parameters, such as water jet pressure, nozzle cross feed, standoff distance, abrasive flow-rate, particle dimension, impact angle and so on. Experiments are designed using Taguchi L9 orthogonal array (Table 5) with appropriate signal-to-noise ratio to evaluate the results.

There are three levels of S/N ratio based on the response character. They are as lower the best (LB), normal the best (NB) or higher the best (HB). For example, surface roughness is lower the best and material removal is higher the best. The S/N ratio of the Material Removal Rate (MRR), kerf taper and the surface roughness were calculated for each level of the machining parameters.

Advanced instruments with high resolution microscope are used to study the imaging analysis on the machined surface. These instruments are strong in image

Table 5 Experimental combinations of machining parameters

Exp. no.	Jet pressure	Nozzle speed	Stand-off distance
1	200	20	1
2	200	30	3
3	200	40	2
4	230	20	2
5	230	30	1
6	230	40	3
7	260	20	3
8	260	30	2
9	260	40	1

analysis and spectroscopic tester, highly interconnected with Windows™ platform. The magnification ranges from 3x to 1000000x with a vacuum chamber plate with a 3-axis motor-powered with ten numbers of ports optional for selection of detectors and accessories. The elemental analyze were carried on the surface and in the cross-sectional area of the exposed samples.

The chamber is equipped with a 3 dimensional motorized stage with ten numbers of ports optional for selection of detectors and accessories. A fast and versatile EDS system (Model: QUANTAX EDS; Make: Brukers) connected with SEM detector port was used to reveal their microstructural and compositional features. The elemental analyze were carried on the surface and in the cross sectional area of the exposed samples.

Appropriate selection of machining constraints to form objective function is difficult and it may lead to complexity. To overcome such situation statistical analysis on the experiments performed are preferred. An ANOVA—analysis of variance is one the best tool to detect the influence of machining factors based on the response of experiments performed. In this section, experiments are formed to Taguchi model (L9 orthogonal array) to predict the influence of each factor over kerf taper, Surface finish and Material Subtraction Rate. From the experimental analysis, the findings and response over defined machining conditions are predicted with reference to S/N ratio.

3 Results and Discussion

On machining the composite fabricated with addition of fillers in different proportion (from the in-house laboratory), the response on kerf wall inclination evaluated. Results on response is found with significant changes. Over kerf taper, the nozzle speed and pump pressure are predominantly influencing process parameters than standoff distance for the proposed experimental design. The contributions of the machining factors in kerf taper are plotted in Fig. 8.

The nozzle speed is an influence factor in case of kerf taper [11]. When the nozzle speed is low the kerf diverges and converges with high speed. Other hand Pump pressure is also giving equal contribution on kerf taper for all different combination of filler composite materials. On other hand, contribution of standoff distance in Kerf inclination minor compared to other two process parameter. The error percentage is due to the factors excluded from the experiments, uncontrollable factors and error associated with the experiment. Kerf wall inclination is a complex parameter, which involves several variables including the contour shape and it compounds to the error percentage. There are other factors excluded from the experiments are abrasive particle size, abrasive particle material type, abrasive particle flow rate, water orifice size, composition and hardness of work piece etc. The uncontrollable factors that cause variability or deviation under normal machining conditions also contribute to error percentage. In AWJM, the contour shape due to parameter variations was ignored,

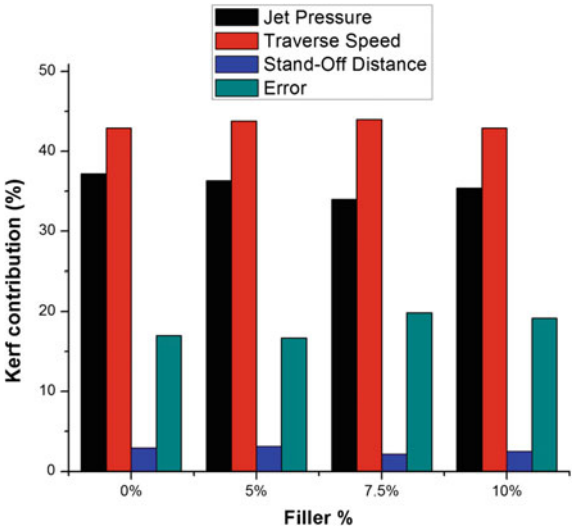

Fig. 8 Contribution of the process parameters on Kerf wall inclination of hybrid natural fibre composites with various filler percentage

which limits the achievable precision of abrasive water jet machining. The above variables contribute to the error percentage in kerf wall inclination.

The conclusion drawn from this analysis was that the speed of nozzle and pump pressure play vital role on the kerf taper during abrasive water jet machining. The effect of transverse speed and the jet pressure on the kerf inclination during abrasive water jet machining is presented subsequently.

Figures 9, 10 and 11, shows variation in kerf changes at different jet pressure for varying traverse speed of the nozzle. The observations are with minor changes for

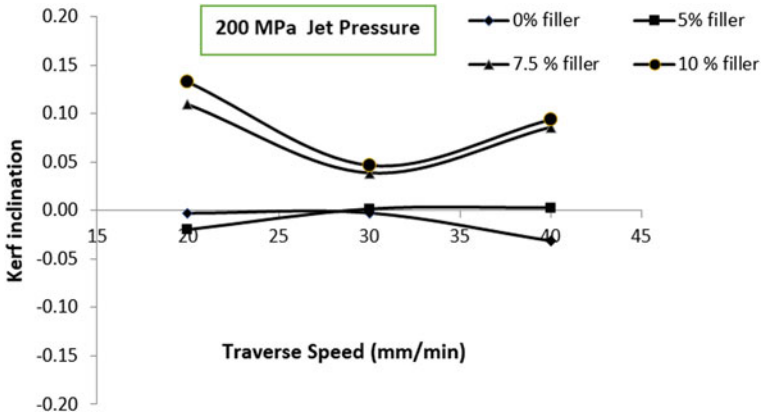

Fig. 9 Difference in kerf wall inclination while machining composite @ 200 MPa jet pressure

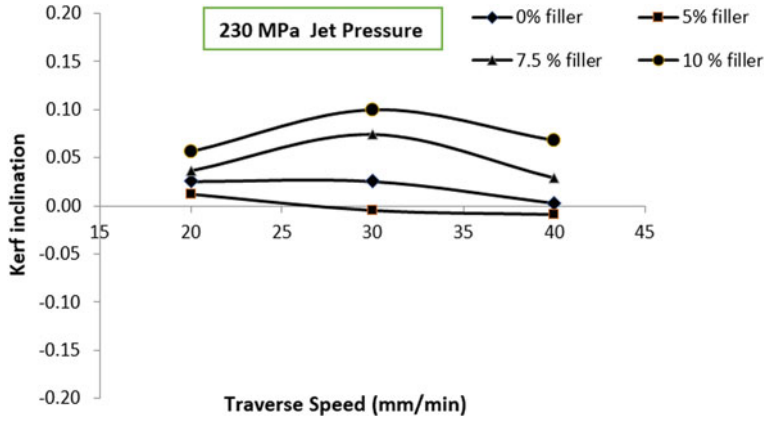

Fig. 10 Difference in kerf wall inclination while machining composite @ 230 MPa jet pressure

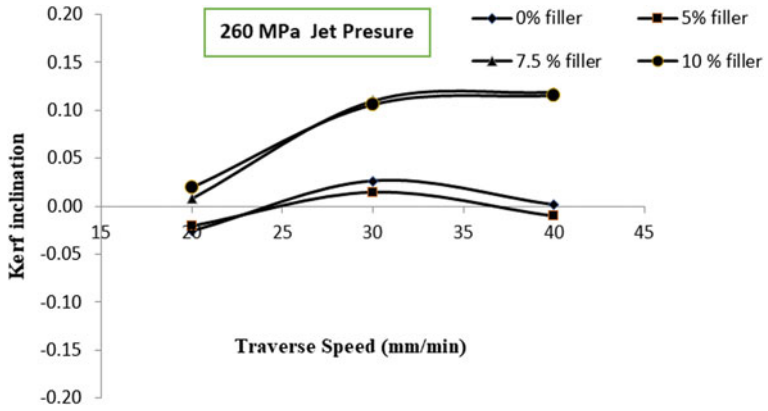

Fig. 11 Difference in kerf wall inclination while machining composite @ 260 MPa jet pressure

each process condition on cutting the hybrid composites in various combination of filler material. The inclination/taper on kerf wall are calculated based on the width of the cut at entry and exit point (with respect to the thickness) of the sample. While machining, the striking of hard particle over the surface of the composite, the material shear will be more and cause changed in kerf wall inclination. Based on the shape and size of the hard particle, the energy generated during machining will cause the work to plastically deform. The cutting efficiency of the abrasive jet has been activated with reference to the water jet pressure and the traverse speed. Figure 12 shows that the basic mechanism of AWJ cutting with different traverse speed. At higher jet pressure and with distraction in traverse speed will produce the coarse surface on machining and effect of dragging of jet. The abrasive direction and its shearing force is based on the efficiency of water jet and its traverse force. It will insignificantly

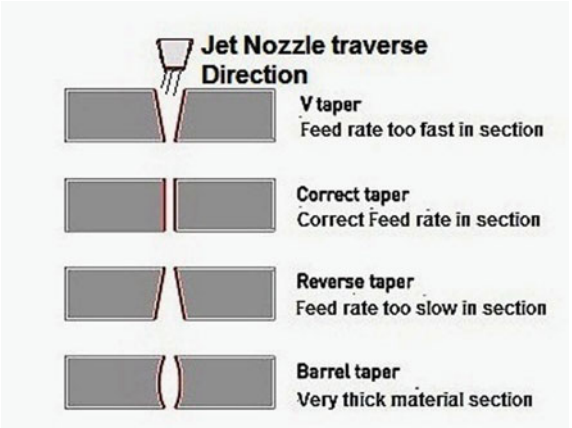

Fig. 12 Deflection in kerf with respect to difference in traverse speed

affect the kerf by the tail flow beyond the cut. From the Figs. 9, 10, 11, medium traverse speed of 30 mm/min originates as the optimistic parameter in 0 and 5% of filler composite to reduce variation in kerf wall inclination. The influence of filler material at 10% (wt%) has led to change the machining property of the composite. It is evidently proved that from the result (Figs. 8, 9 and 10) at optimum traverse speed kerf wall inclination is minimum (or near to zero). There were very significant changes in kerf wall inclination at varying traverse speed for 7.5% filler in materials design. It is added with 10% filler composition and kerf inclination was found in increasing trend at higher traverse speed. From the kerf analysis, traverse speed and jet pressure are the dominating parameters. The optimized traverse speed for kerf is 30 mm/min, when increasing the jet pressure, kerf wall inclination also increased.

3.1 Results on MRR with Respect to Input Process Parameters

This section details the process factors influence on MRR. Figure 13 clearly shows that the main dominating machining parameter in MRR is nozzle speed only.

The effect of water jet pressure for material removal rate is relatively very less compared to the nozzle speed. It is important to note that the cutting or machining of composite is tough as compared to other materials (as per the machinability index). Since, the machining process condition finds a predominant factor to produce high surface quality on machining composite. On other hand, contribution of standoff distance and jet pressure to affect material removal rate is minor compared to other process parameter. The material removal has increase trend in all the conditions for less filler wt% (i.e. 0 and 5%) as shown in Figs. 14, 15 and 16. This is completely due to the removal of matrix material and partial cutting of fibre during erosion by the

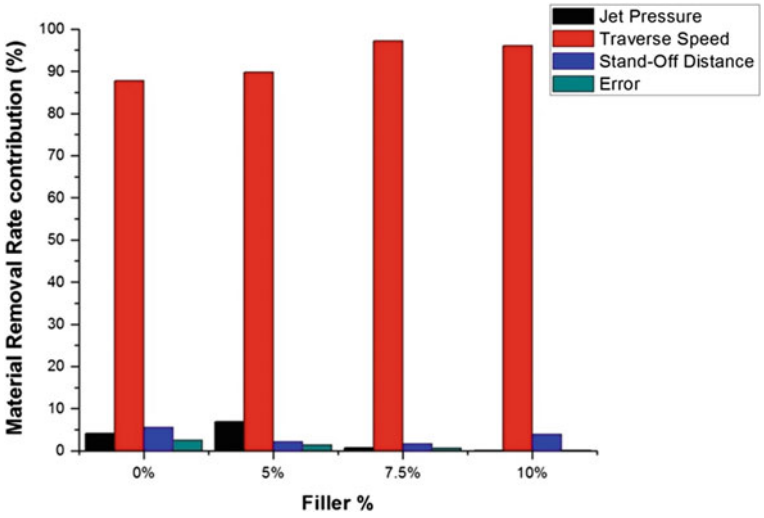

Fig. 13 Contribution of the process parameters on Material Removal Rate (MRR) of hybrid natural fibre composites with various filler percentage

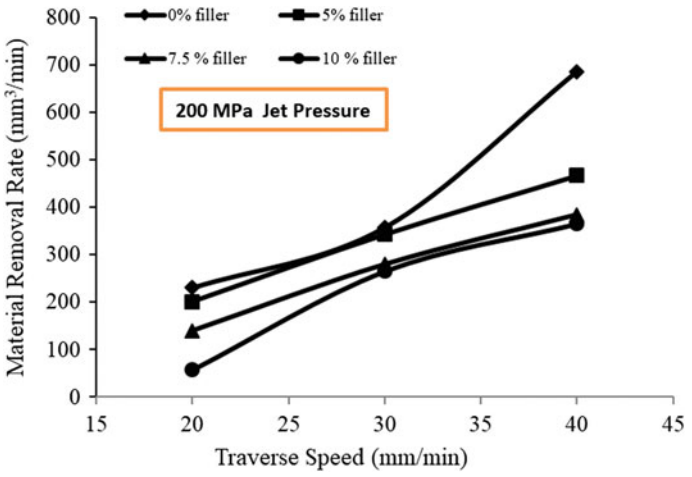

Fig. 14 Material removal rate on machining hybrid natural fibre composite @ 200 MPa jet pressure

hard-abrasive particle. The slow traverse speed leads to the removal of more material in more filler wt% combination and divergence are formed due to maximum contact area while machining. However at higher traverse speed and higher jet pressure, the maximum material are removed in less filler wt% combination and contact area are reduced during machining.

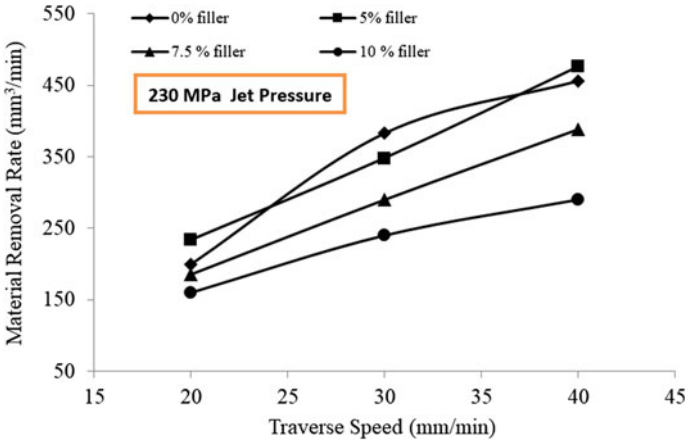

Fig. 15 Material removal rate on machining hybrid natural fibre composite @ 230 MPa jet pressure

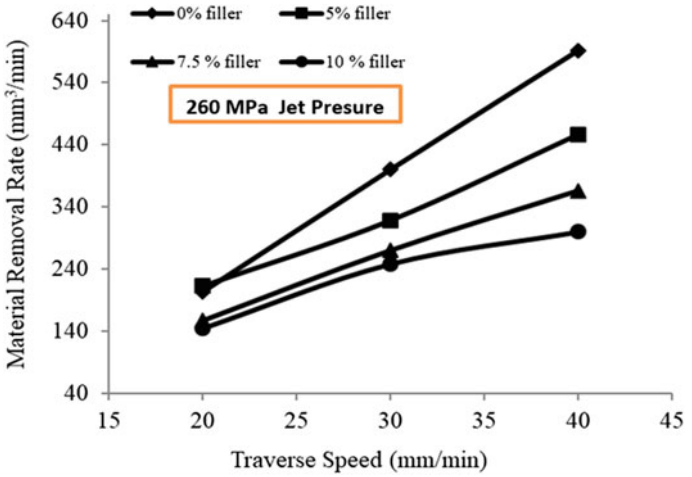

Fig. 16 Material removal rate on machining hybrid natural fibre composite @ 260 MPa jet pressure

The variation in MRR is in increasing trend with respect to the increase in the nozzle speed. The maximum amount of material found removed at a process combination of higher jet pressure and nozzle speed. This cutting mechanism is invariant with respect to the amount of fillers used in the composite. It is completely based on the mechanical properties of the matrix and the fibre volume/weight proportion. When the sharp abrasives strike the brittle composite, the failure occurs. The rate of failure varies with respect to the kerf and fibre orientation. The addition of fillers in the composite helps to increase the strength and tough to cut the composite.

3.2 Results on Input Process Parameters and Surface Quality

Surface roughness is the most important output parameter in AWJ cutting [12]. In AWJ cutting process, the surface profile depends on nozzle cross feed (traverse speed). The contribution of traverse speed is the predominant factor to decide the surface quality while machining with AWJ. Comparatively, the jet pressure contribution on surface finish is three-fold less than the nozzle movement. Distraction in jet flow makes the erodent to produce irregular surface finish with maximum hedges over the machined surface. Significant factor for erodent/abrasive distraction is invariant jet flow and higher the standoff distance. This is called coanda effect in jet flow. Thus the standoff distance contribution is very less compared to other input process parameters as show in Fig. 17.

To study the surface quality in detail, the samples were tested with surface meter to read out the roughness on machined area. Surface finish of the sample is measure with Mitutoyo Surface tester. Three readings at different places are taken for each sample and the average Roughness value (Ra) were plotted in Figs. 18, 19 and 20. The surface roughness is substantially having variation in view of different process conditions. In proposed research, the addition of fillers in different proportion has produced better surface quality than the plain composite material. The filler material has protected the surface from severe damage with high bonding strength. The delamination and fibre pullouts are reduced with filler reinforced composites. Therefore, the composite

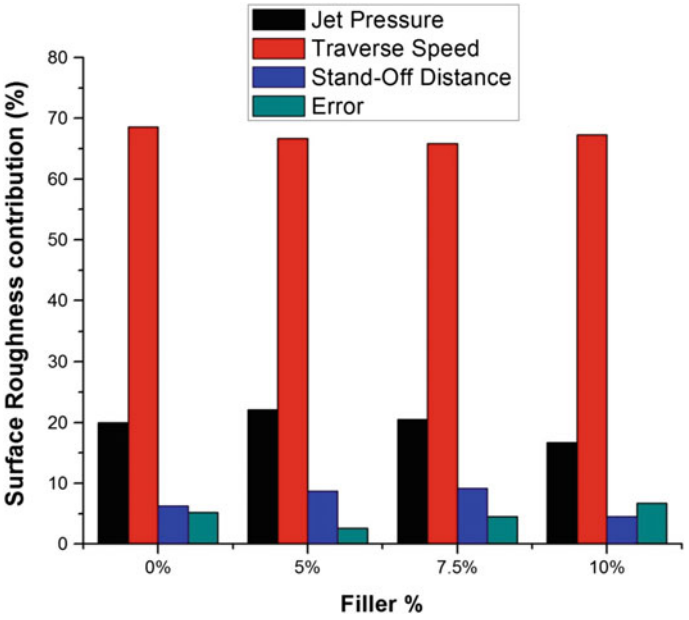

Fig. 17 Contribution of the process parameters on surface roughness (Ra)hybrid natural fibre composites with various filler percentage

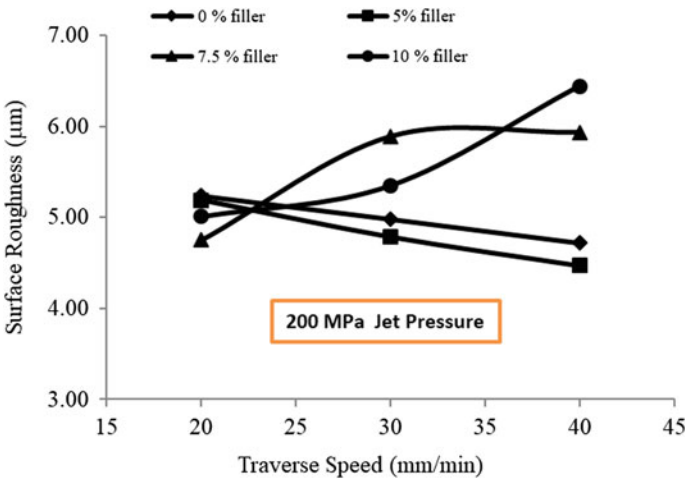

Fig. 18 Surface roughness (Ra) on machining hybrid natural fibre composite @ 200 MPa jet pressure

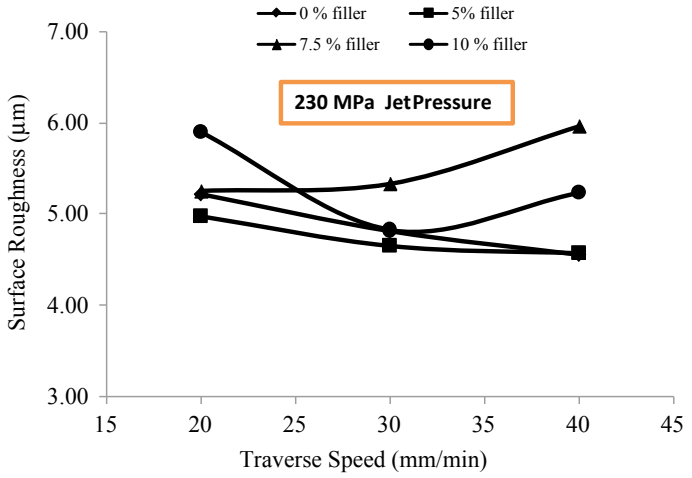

Fig. 19 Surface roughness (Ra) on machining hybrid natural fibre composite @ 230 MPa jet pressure

property can be enhanced with fillers and the machinability of the composite is also maintained with better surface quality.

The wear trend was in increasing mode and justifying the statements claimed in scanning electron microscopic result. The variations in roughness value are wide and it is due to the maximum fibre pullouts and blisters of clustered fibre over the surface. When there is not filler, composite is subjected to lapping effect by the high-pressure jet and fine erodent particle. Due to the micro filler particle reinforcement, matrix

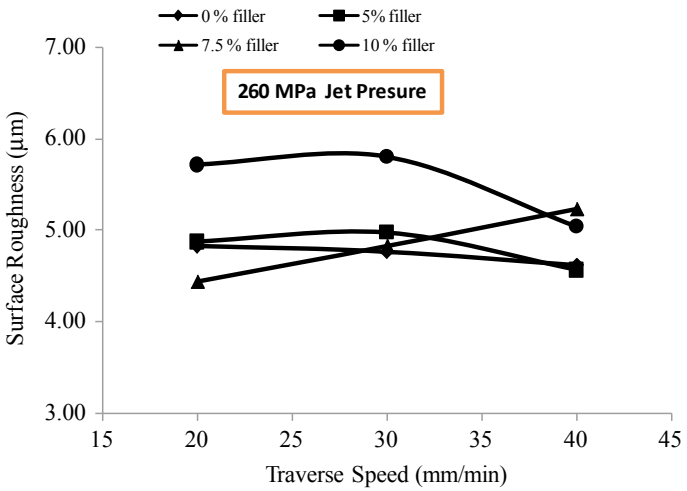

Fig. 20 Surface roughness (Ra) on machining hybrid natural fibre composite @ 260 MPa jet pressure

region are reduced and fibre are prone to face the buckling effect. This buckling effect is with hemp fibre alone forms coarse surface roughness. However, the fine Kevlar fibre and coarse fibre a pullout has led to these wide variations in surface roughness. Therefore, the addition of bio filler powder material has highly influenced the machinability of the natural fibre hybrid composite and it can withstand impact energy on applications.

3.3 Surface Morphology During AWJ Machining in Hybrid Fibre Filler Composite

The electron imaging observed from the SEM infers that the surface is highly damaged with severe fibre pullouts with maximum erosion. These observations are found on the composites without filler reinforcements as shown in Fig. 21. It is due to less bonding strength of the composite and brittle behavior causing fibre to damage on shear. The striking energy of the sharp erodent causes the composites to fail on AWJ cutting process. Figure 22 indicates that the weak matrix material has been subjected to flush off and fibres pullout without strength in bonding. This can be justified in MRR calculation, as the matrix has bulk removal in material and severe in surface damage causing kerf wall inclination. In filler reinforce composites, the major drawbacks on plain composite material are rectified. The main function of the filler material is to increase the bonding strength of the matrix in the composite. Figure 23 shows the enhanced surface quality of the filler reinforced composite material after AWJ cutting. It is clear to infer that the filler material has increased with the bonding

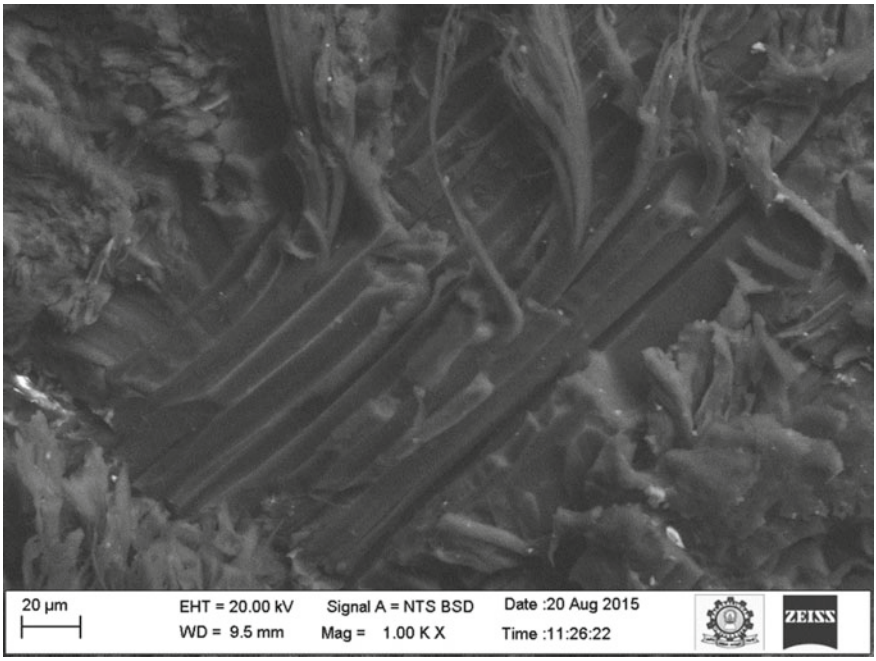

Fig. 21 The electron image of the plain composite (without fillers) observed with fibre pullouts and delamination after AWJ cutting

strength and brittle transition was reduced on increase of fillers. The sudden strike on matrix was controlled with the filler reinforcement. The most important quality observed with filler is that the composite has high packed structure and fibre pullouts are reduced.

AWJ machined surface of with and without filler hybrid natural fibre/epoxy composite subjected to microscopic analysis are given in Fig. 24. The water jet nozzle direction and abrasive erodent flow direction are pictorially represented for clear understanding. While machining the fibres are induced to sudden impingement of hard abrasive particles. Fibre oriented in the same direction of flow of erodent/hard abrasive will face buckling effect and tends to break as irregular. It is distinct to state the mechanism involved during hard abrasive particle machining involved in hybrid composite material. Since the composite was made of hemp and Kevlar fibre at different fibre dimensions; irregularity in machined surface are found. The hemp is of solid fibre and Kevlar is in cluster form.

Figure 25 represents that the hemp has been stroked out completely due to sudden impact and washed off from the matrix material. At the same, the Kevlar are strong and formed as a cluster are difficult to machine with the hard abrasive erodent which appears like micro hairs adhering to the matrix bond. When the impact force created during the water jet cutting process will be evenly distributed with the number of strands and thus the impact energy are reduced.

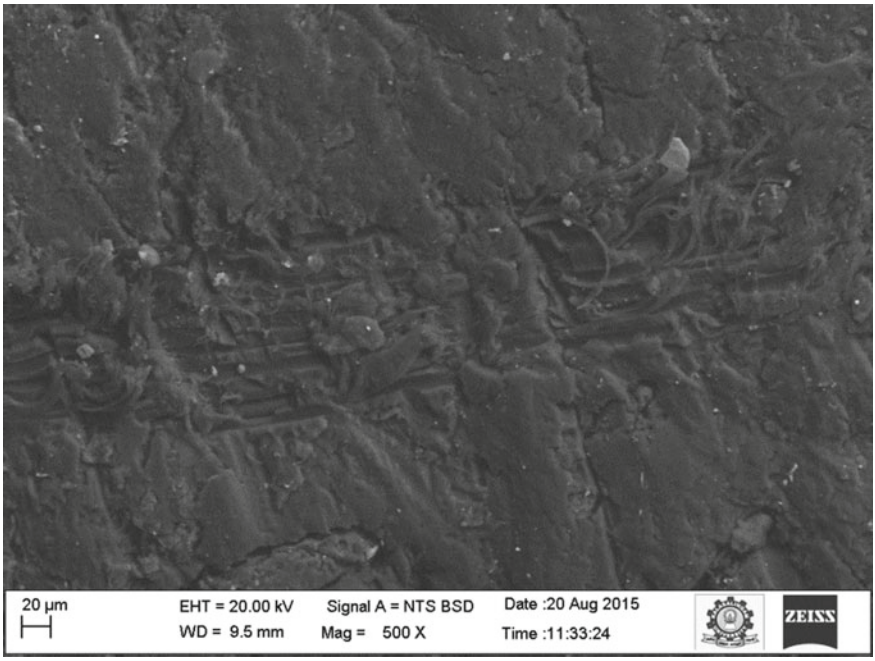

Fig. 22 The electron image of the hybrid fibre composite observed with shredded structure after AWJ cutting

Therefore, the solid fibre are easily machined/chiseled than the bulk Kevlar fibre. During this stage the erodent/abrasive particle will continuously impingement over the surface area and the mechanism leading to plough the fibre. Adjunct layer of the fibre covered with matrix will have maximum scoring due to the influence of strong abrasive particle led to the erosive wear. At higher magnification, the observation on microscopic image represents the pullouts and blisters of fibre (Fig. 26) involved during ploughing. Influence of filler has major contribution towards fibre pullouts and ploughing of hybrid natural fibre composite. At higher proportion of filler of material, the distribution and densification are uniform which was found difficult to machine. The same with optimum filler material the material has good machinability and good surface finish.

4 Conclusions

With four different weights with and without filler materials were used in Hemp–Kevlar natural fibre hybrid composite and these composites were machined by abrasive water jet cutting. From the experimental investigation and response on machining process performed, following conclusions are drawn:

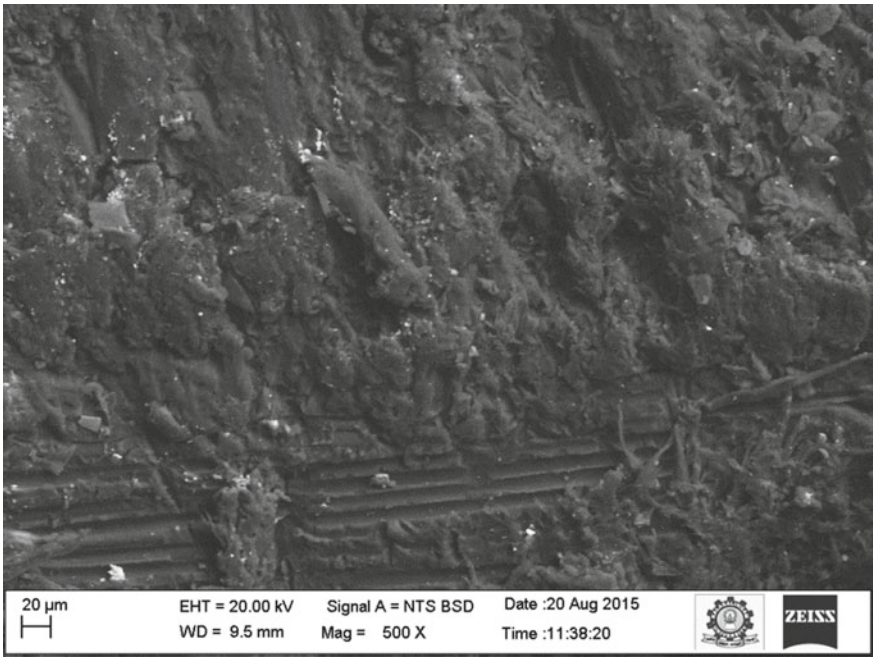

Fig. 23 The electron image of the hybrid composite with fillers reinforcement shows good bonding effect after AWJ cutting

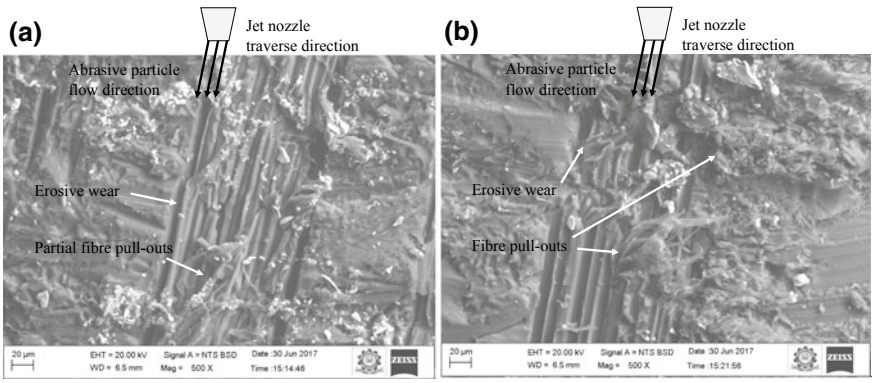

Fig. 24 Surface morphology of the AWJ machined hybrid fibre composite with 7.5% filler (**a**) and 10% filler (**b**) material design

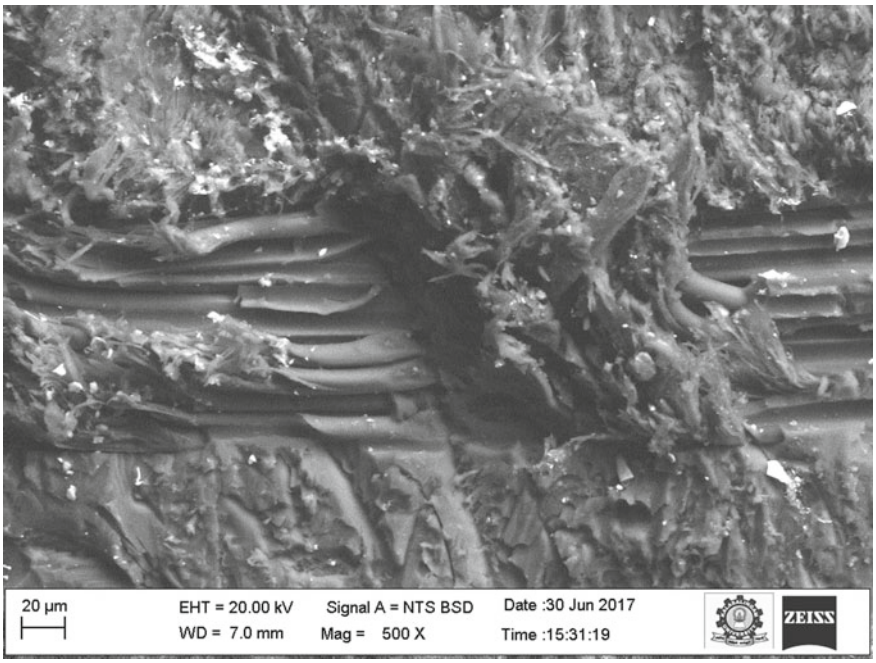

Fig. 25 Fibre ploughed by hard abrasive particle while machining with AWJ

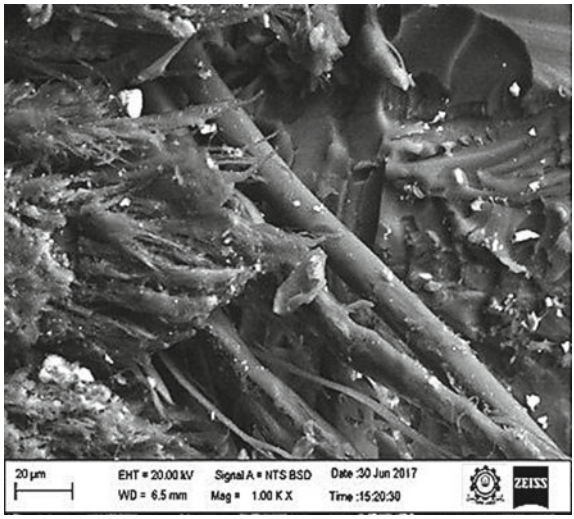

Fig. 26 Microscopic image at higher magnification representing wear mechanism

1. The predominant factors influencing the response on kerf, MRR and surface quality is nozzle traverse speed. Based on the movement of the nozzle, the abrasive behaves. Subsequently, the jet pressure holds is the succeeding factor followed by SoD. The optimum jet pressure for all output parameters is 230 MPa.
2. The optimum kerf is maintained at low traverse speed.
3. The Material Removal Rate (MRR) increases with decrease in filler percentage as the filler act as particle reinforcement, hindering the machining process.
4. The surface roughness (Ra) was minimized in all level of input parameters. The surface quality is maintained with fewer amounts of filler loading.

Therefore, the composite material developed in the combination of natural fibre and fillers have good mechanical property and better machinability with AWJ cutting process.

References

1. Gachter, R., Muller, H.: Plastics additives, 3rd edn. Hanser Publishers, New York (1990)
2. La-Mantia, F.P., Morreale, M.: Green composites: a brief review. Compos Part A **42**, 579–588 (2011)
3. Bhowmik, S.J., Ray, A.: Abrasive water jet machining of composite materials. In: Advanced manufacturing technologies, materials forming, machining and tribology. https://doi.org/10.1007/978-3-319-56099-1_4
4. Sheikh-Ahmad, J. Y.: Conventional machining of FRPs, machining of polymer composites. Springer Science+Business Media, pp. 143–231 (2009)
5. Shanmugam, D.K., Nguyen, T., Wang, J.: A study of delamination on graphite/epoxy composites in abrasive water jet machining. Compos. A Appl. Sci. Manuf. **396**, 923–929 (2008)
6. Schwartzentrber, J., Kspelt, J., Papini, M.: Prediction of surface roughness in AWJM trimming of fibre reinforce polymer composite. Int. J. Mach. Tools Manuf. **122**, 143–152 (2017)
7. Miron, A.V., Balc, N., Popan, A., Stefana, C., Bere, P.: Studies on water jet cutting of 2d parts made from carbon fibre composite materials. Acad. J. Manuf. Eng. **112**, 87–92 (2013)
8. Azmir, M., Ahsan, A., Rahmah, A., Noor, M., Aziz, A.: Optimization of abrasive water jet machining process parameters using orthogonal array with grey relational analysis. In: Regional conference on engineering mathematics, mechanics, manufacturing & architecture EM3ARC, pp. 21–30 (2007)
9. Ahmed, D.H., Naser, J., Deam, R.T.: Particles impact characteristics on cutting surface during the abrasive water jet machining: numerical study. J. Mater. Process. Technol. **23**, 116–130 (2016)
10. Narayanan, C., Balz, R., Weiss, D.A., Heiniger, K.C.: Modelling of abrasive particle energy in water jet machining. J. Mater. Process. Technol. **213**, 22–29 (2013)
11. Jagadish., Gupta, K., Rajakumaran, M.: Evaluation of machining performance of pineapple filler based reinforced polymer composites using abrasive water jet machining process. In: IOP Conference Series: Materials Science and Engineering **430**, 012046 (2018)
12. Phokane, T., Gupta, K., Gupta, M.K.: Investigations on surface roughness and tribology of miniature brass gears manufactured by abrasive water jet machining. In: Proceedings of the Institution of Mechanical Engineers, Part C: Journal of Mechanical Engineering Science **232**(22), 4193–4202 (2018)

Surface Engineering of Tungsten Carbide Tool Material by Nano and Microcrystalline Diamond Coatings

Kaleem Ahmad Najar, Shah Aarif Ul Islam, and N. A. Sheikh

Abstract Diamond is generally accepted as a material with individual properties such as superlative hardness, low coefficient of friction and very high thermal conductivity. Synthetic diamond can be achieved in the form of thin and thick films using experimental chemical vapor deposition (CVD) methods. Cemented tungsten carbide (WC–Co) is the commonly used tool material with high hardness (~18 GPa) and high elastic modulus (~550 GPa) and, also compatible to the growth of synthetic diamond films. Presently, synthetic diamond coatings have been widely used on carbide cutting tools from long time to prevent the abrasive wear occurred on conventional tools. Based upon the size of the grains, synthetic diamond coatings are basically classified into nanocrystalline diamond (NCD) and microcrystalline diamond (MCD). In the work reported in the present chapter, smooth and adhesive thin NCD and MCD coatings were deposited on chemically treated tungsten carbide substrates using pre-determined process parameters in the hot filament chemical vapor deposition (HFCVD) method. Tungsten carbide with 6% Co is the mostly accepted grade of base material used for the successful growth of synthetic diamond films on its surface and, also to minimize the thermal residual stresses existing during the deposition and cooling down process between the interfaces of coating and substrate. Mostly, these thermal residual stresses are produced due to difference in thermal expansion coefficients between the coating and substrate. During deposition process, the process parameters such as methane concentration ($\%CH_4/H_2$) and chamber pressure were controlled automatically using pre-programmed recipe for the growth of NCD and MCD films. The structural characteristics and quality of the synthetic diamond films were confirmed using X-ray diffraction and Raman spectroscopy techniques, respectively. The surface morphology was studied using a high resolution scanning electron microscope (HRSEM) and atomic force microscope (AFM). Moreover, the hardness measurement of coatings were done using

K. A. Najar (✉) · N. A. Sheikh
Department of Mechanical Engineering, National Institute of Technology Srinagar, Jammu & Kashmir, India
e-mail: najar.kaleem@gmail.com

S. A. U. Islam
Department of Physics, National Institute of Technology Srinagar, Jammu & Kashmir, India

K. Gupta (ed.), *Surface Engineering of Modern Materials*, Engineering Materials,
https://doi.org/10.1007/978-3-030-43232-4_7

a Berkovich nanoindenter. After that, a comparative evaluation between these two types of coatings was done.

Keywords Nanocrystalline · Surface morphology · Cutting tool · Tungsten carbide · Diamond

1 Introduction

Artificial diamond coatings are known to have exceptional tribological and mechanical properties (like better resistance to wear and tear, extraordinary hardness and low values of coefficient of friction) when subjected to sliding against several ceramic counter objects. Commonly, these synthetic diamond films are obtained through many CVD techniques using initial process parameters [1, 2].

Fundamentally, on the basis of grain size diamond films fabricated through CVD process has been classified as microcrystalline diamond (MCD) and nanocrystalline diamond (NCD). Coatings of NCD generally display nano-crystallinity comparable to ~3 μm thick coatings. The values of surface roughness and averaged grain size of NCD coating usually increase when there is an increase in the coating thickness [3]. NCD films are especially suitable for Tribological applications and are generally acquired by minimizing grain-size into nanometer-dimensions, but the internal thermal residual stresses within a coating can be increased with the decrease in grain size [4].

Owing to the higher amounts of sp^2-carbon content present in NCD films, these films have shown less adhesion quality on ceramic substrates in comparison to crystallized MCD films and this shows that the adhesive force will be more if the percentage graphitic-carbon phase is small near the substrate-coating interface [5]. The crystallinity and mechanical properties of NCD films will be highly affected owing to grain boundaries being large in number, which comprise of high amounts of graphitic-carbon [6]. In synthetic diamond growth, a well columnar grain pattern is witnessed every time that is a very significant factor to reveal morphology of the coated films [7]. The adhesive quality of diamond coatings is also significantly influenced by the film microstructure. Thus, the surface roughness (impurity), surface morphology and microstructure of a coating are the important factors for improving adhesive bond between substrate and diamond film [8, 9]. Many quantitative and qualitative experimental techniques can be used to investigate adhesion features of these coatings, such as dynamic scratch adhesion test and indentation test [10, 11]. The line-width of Raman peaks is directly correlated with both, growth rate of the film and inverse of the grain size, measured by X-ray method. Thus, the grain size of the coating is correspondingly directly related to the reciprocal of growth rate of the film [12].

In diamond films, there is development of two types of residual stresses; one is internal stress and the other is thermal stress (caused because of the coating and substrate having different thermal expansion coefficients). Thus, residual thermal

stresses are mostly affecting the adhesion strength of diamond films on the substrate [13]. The size of grains in coatings of diamond can well be increased from nanometer range to micrometer range by increasing the thickness of the coating and this will also lead to the increase in internal residual stress. Also, increasing the coating thickness improves the coating-resistance, de-lamination and capacity to bear load [14]. In general, the substrate-coating adhesive force can be improved by increasing the contact area [15]. For a large area diamond coated flat substrate the generated thermal strain can be calculated from Eq. (1), neglecting strain at the edges. Also, under plane stain conditions the resulting thermal stresses can be calculated from Eq. (2) [16].

$$\in_{\text{th}} = \sum_{T_S}^{T_R} [\alpha_S - \alpha_D] \Delta T \tag{1}$$

$$\partial_{\text{th}} = \frac{E_D \times \in_{\text{th}}}{(1 - V_D)} \tag{2}$$

In Eq. (1), α_D and α_S are the coefficients of thermal expansion of the coating and substrate, respectively, T_R, the room temperature and T_S, the growth temperature of coating. Also, E_D is the modulus of elasticity and V_D the Poisson ratio of the coating.

This chapter presents the studies on both MCD and NCD coatings that were deposited experimentally on chemically etched WC–Co substrates after maintaining the optimum process parameters. The surface characteristics, like crystalline quality and microstructure of these synthetic coatings were analyzed employing XRD, SEM and Raman techniques. Hardness property of each diamond coating was evaluated individually using Berkovich nanoindenter. Hence, the description of chemicals, materials, instruments and characterization techniques which are being utilized presently and also the technical details employed to perform the experiments involved, are explicitly discussed in the subsequent sections.

2 Materials and Methods

2.1 Chemical Etching Process

Ceratizit-CTF12A, with 6% Co, a cemented tungsten carbide (a candidate material for cutting tool) was chosen as a substrate with dimensions (10 mm × 10 mm × 3 mm) and ultrasonicated in ethyl alcohol to dislodge any impurities if present on the substrate surface. Since, on the surface of WC–6% Co substrate the presence of cobalt opposes the diamond film growth, as it encourages the graphitic-carbon formation, which in turn reduces the adhesive quality of the diamond coatings. Thus, prior to the deposition of high quality films of diamond on carbide substrates, chemical etching

Table 1 Pre-treatment of substrate surface procedure for growing MCD & NCD coatings [26]

S. no.	Procedural details	Chemicals	Remarks
1	Use soap solution to clean substrate	Detergent powder	Ultrasonic agitation
2	Rinse substrate in distilled H_2O	–	Dry using hot air blow
3	Degrease substrate	Acetone	Ultrasonic agitation
4	Rinse substrate in distilled H_2O	–	Dry using hot air blow
5	10 min chemical etching, after treatment with Murakami's reagent	Potassium Hydroxide, Potassium Ferricyanide	Ultrasonic agitation
6	Rinse substrate in distilled H_2O	–	Dry using hot air blow
7	10 s cobalt etching utilizing Caro's acid	Hydrogen Peroxide, Sulfuric Acid	Highly reactive solution
8	Rinse substrate in distilled H_2O	–	Dry using hot air blow
9	2 min ultrasonication	Ethanol	Ultrasonic agitation
10	10 min diamond seeding	Dispersed diamond seeds in (DMSO)	Ultrasonic agitation
11	Rinsing followed by 2 min cleaning	Isopropanol	Ultrasonic agitation
12	Dry using hot air blow	–	Load samples to chamber

is a very significant step. The whole steps of procedure for pre-treatment of surface for WC–6% Co substrate are listed in Table 1.

However, Fig. 1a, b show the XRD patterns of Co-cemented tungsten carbide sample before and after chemical etching process, respectively. The appearance of distinct (WC & Co) peaks explicitly depicts the removal of cobalt from the surface of tungsten carbide substrate by etching process, as seen in Fig. 1b. Surface cobalt was removed by Caro's acid and tungsten etching was done by Murakami reagent to form cavities on the surface due to which the strength of adhesion increases [17]. Figure 2a, b, c show surface morphologies of the cemented tungsten carbide (WC–6% Co) before treatment, and after treatment from Murakami Reagent and Caro's acid, respectively [18].

2.2 Hot Filament Chemical Vapor Deposition Process

The (HFCVD) hot filament chemical vapor deposition is a widely used deposition process to achieve various types of synthetic diamond coatings on carbides and ceramics for their industrial applications. Most of the tribological and mechanical

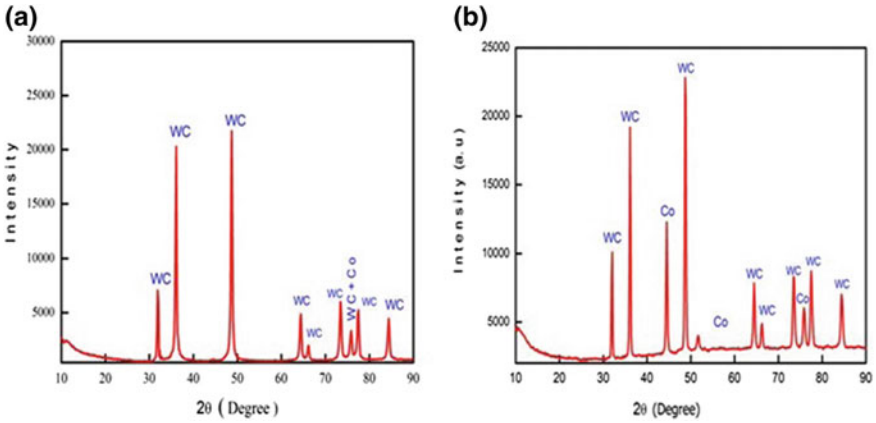

Fig. 1 XRD patterns of WC–Co substrate **a** prior to etching and **b** after etching [17]

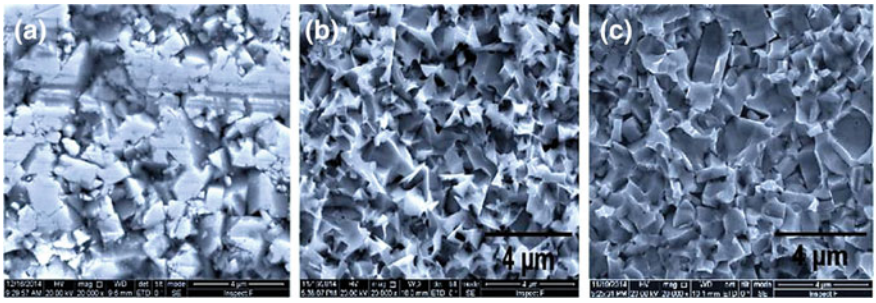

Fig. 2 Surface morphology of WC–Co sample **a** before treatment, and after treatment from **b** Murakami Reagent and **c** Caro's acid [18]

properties of these coatings are primarily affected by their crystallinity and grain size. Both these, grain size and crystalline quality of the diamond films are very important factors that are mostly controlled by methane percentage (%CH_4/H_2) ratio and pressure of the deposition chamber. For the growth of crystalline diamond the concentration of methane can be varied from 1 to 5% and the pressure of the chamber can be varied from 5 to 55 Torr, using initial pre-programmed recipe. Other parameters that influence the crystallinity and the rate of growth are, temperature of the substrate (700–900 °C) optimized, temperature of filament (1800–2200 °C) optimized and substrate to filament separation (1–4 cm) optimized.

In this work, HFCVD system (sp^3 Diamond Technologies, Model 650 series) was used to deposit synthetic films of diamond, as shown in Fig. 3. During deposition process, pressure of the chamber and concentration of methane were automatically controlled by mass flow controllers and throttle valve, respectively. In every experiment, a tungsten wire array (0.12 mm) were selected as hot filaments for the initiation of precursor gases (H_2 and CH_4) and the substrate-filament separation was

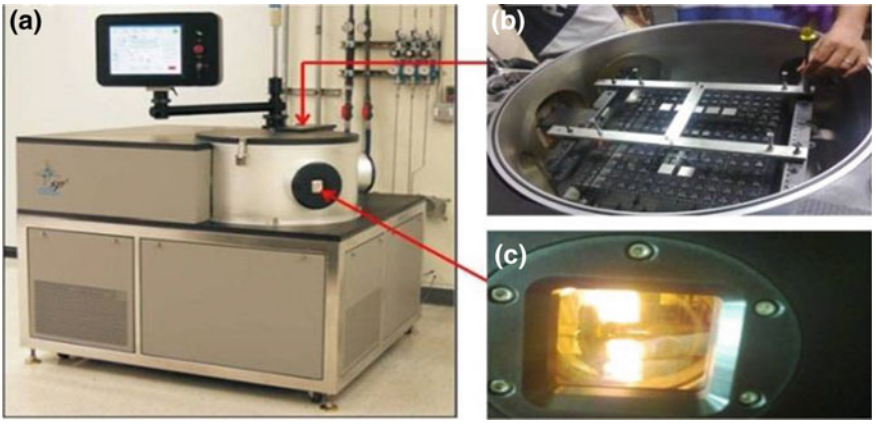

Fig. 3 **a** HFCVD instrumental setup, **b** Interior of deposition chamber and **c** quartz window view of the WC–Co substrates while diamond growth [18]

Table 2 Optimized growth/deposition parameters for NCD and MCD films [18]

Coating Type	Chamber Pressure (Torr)	CH_4/H_2 (%)	Filament temperature (°C)	Substrate temperature (°C)	Deposition Time (hrs.)	Coating Thickness (μm)
MCD	36	2	−2200	−850	3	−3
NCD	12	4	−2200	−850	3	−3

maintained at 1.5 cm. Hence, the growth parameters adopted in this experimental work for the optimized deposition of NCD and MCD coatings are stated in Table 2 [18]. After the deposition process, the toxic exhaust gases produced in the HFCVD chamber were diluted with nitrogen gas, which was used before and after the growth process to flush the chamber. The temperature of CVD chamber was retained at ~50 °C by means of a circulating water chiller and was made of aluminum with cooling channels.

3 Surface Characterizations Techniques

The microstructure and morphology of the surface of synthetic diamond coatings were observed by High Resolution Scanning Electron Microscope (HRSEM, Quanta 3D, FEI). The crystalline quality of the coatings was analyzed by the grazing incidence X-ray diffraction (XRD, GIXRD, PANalytical), having source wavelength $\lambda = 0.154$ nm and grazing angle of 3°. Structural characterization and stress state analysis was studied by Raman spectroscopy microscope (Alpha 300, WITec) having a laser wavelength of 488 nm.

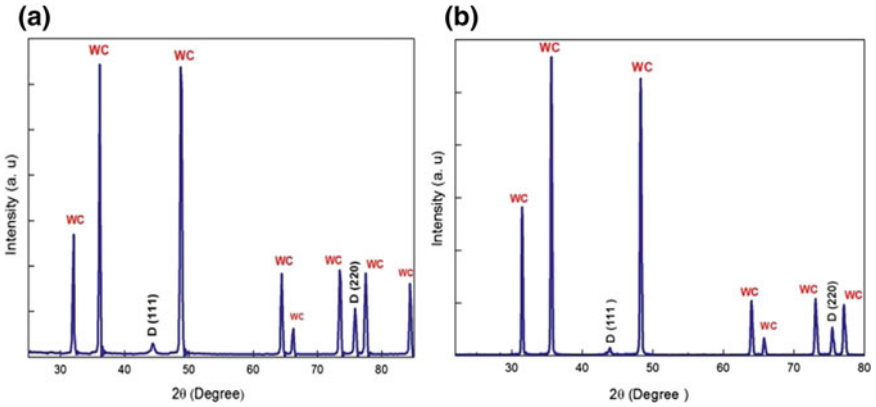

Fig. 4 XRD patterns of **a** MCD and **b** NCD coatings [17]

Generally, XRD technique is employed to reveal phase purity, phase type and the crystallographic structure of 2-D thin diamond films or 3-D bulk samples. Analysis of the XRD and Raman patterns revealed oriented crystalline and columnar growth along with high phase purity for both NCD and MCD coatings.

3.1 XRD Patterns of MCD and NCD Coatings

The X-ray diffraction patterns of NCD and MCD coatings are represented in Fig. 4a, b, respectively. Distinct and strong peaks of cubic diamond coating were observed at the diffraction angles of approximately 44° and 75.5° conforming to (111) crystal and (220) crystal planes, correspondingly for both these coatings, along with (WC) substrate peaks. These peaks reveal the high crystallinity of each diamond coating. It is clearly confirmed that the grain size of MCD coating is found more than NCD coating and also the grain size of carbide material is found more than each diamond coatings, due to the differences in their peak highest [17, 19].

3.2 Raman Spectroscopy of MCD and NCD Coatings

The crystallinity and chemical nature of diamond coatings were studied by using Raman spectroscopy technique. Thus, for the confirmation of diamond nature, a fundamental stress free Raman peak is shown by the diamond coating near about 1332 cm^{-1} [20]. Figure 5a, b show the Raman spectra of MCD and NCD diamond coatings, respectively. Here there is a shift towards higher side of the first order fundamental Raman peak which is focussed at 1333 cm^{-1}, indicates the residual

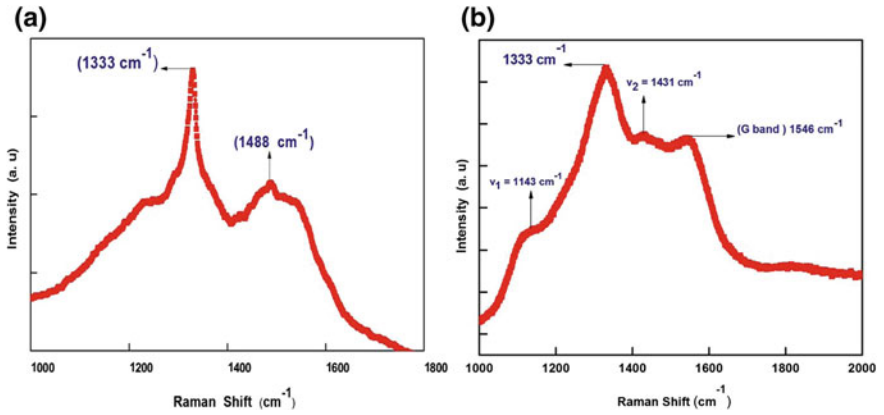

Fig. 5 **a** MCD coating and **b** NCD coating, Raman spectra [21] with kind permission from Elsevier

compressive stress being present in both these coatings. Owing to the different thermal expansion coefficients of coating and substrate, compressive residual stresses are produced [21], which can be estimated easily from the equation $\sigma = -0.348$ (ν_m–ν_0) GPa for the un-split Raman peak, ν_m, where $\nu_m = 1333$ cm^{-1} and $\nu_0 = 1332$ cm^{-1}. Hence, each deposited diamond film accommodates the compressive stresses of 0.348 GPa [22]. The other two peaks observed at $\nu_1 = 1143$ cm^{-1} and $\nu_3 = 1431$ cm^{-1}, represent the in-plane (C–H) characteristics and vibrational modes of (C=C) stretching, correspondingly. The presence of transployacetylene (TPA) chain along grain boundaries of the NCD coatings is the main source of these modes [23]. Also, the quality factor (*Q*) was calculated for the deposited diamond films by using the following formula [24].

$$Q = \{\frac{I_d}{I_{d+I_{gIc}}}\} \times 100\% \tag{3}$$

where, I_d in Eq. (3) stands for intensity of the sharp diamond peak and I_{gIc} stands for intensity of the graphitic-carbon broad peak. From Eq. (3), for NCD coating; $Q = \left\{\frac{1333\,\text{cm}^{-1}}{1333\,\text{cm}^{-1}+1546\,\text{cm}^{-1}}\right\} \times 100\% = 46\%$.

3.3 *Topography of the Surface of MCD and NCD Coatings*

The microstructure, grain size and morphology of the diamond film surfaces were studied by HRSEM technique. Figure 6a, b, c show the HRSEM micrographs of NCD coating at different magnifications. The grain size on its surface is found to lie in the 0.2–0.6 μm range of morphology. In this aspect, the average grain size is calculated from the histogram of SEM micrograph as ~0.35 μm, represented in Fig. 6d. When

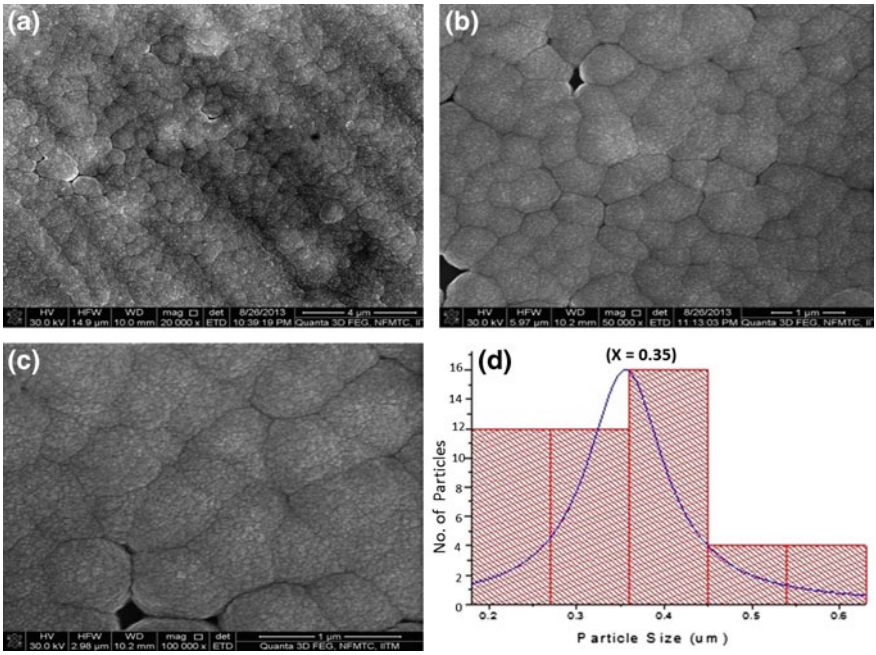

Fig. 6 **a**, **b**, **c** SEM micrographs of NCD coating at different magnifications, **d** Histogram of the SEM image [25]

the concentration of methane is increased from 2 to 4%, the development of secondary nucleation takes place that slows down the existing rate of growth of the grains, which results in a grain type having cauliflower like structure that is generally observed on NCD surface. Nano-features with normal grain growth were observed all over the surface and these are the important characteristics of thin nanocrystalline diamond coatings. Generally, on the surface of MCD film the grains with columnar structure and morphology of faceted form were observed. Similarly, Fig. 7a, b, c display the SEM micrographs of MCD coating at different magnifications, along with the grain size range lying in between 0.3 and 0.8 μm. The average grain size calculated from the histogram of its SEM image comes out to be ~0.57 μm, shown in Fig. 7d [3, 25]. Figure 8a, b display the typical cross-sectional morphologies of the NCD coatings and MCD coatings correspondingly, along with the coating and substrate thicknesses. The composition of both the surface coatings was verified by the energy dispersive analysis of X-rays spectroscopy (EDAX) technique, as shown in Fig. 9 [26].

Moreover, the AFM technique was employed in tapping mode for the surface imaging which reveals all the descriptions of phase and height imaging. Compared to HRSEM imaging, the AFM height imaging.

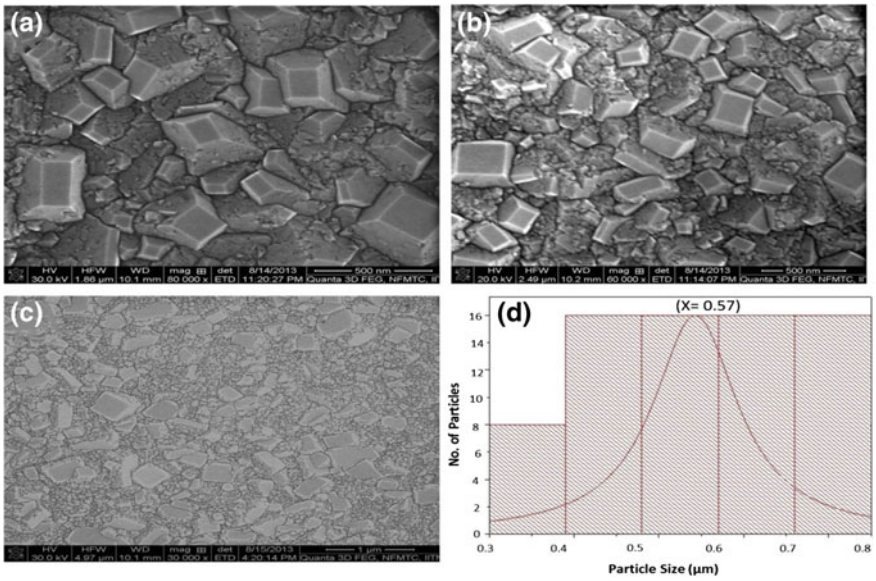

Fig. 7 **a**, **b**, **c** SEM micrographs of MCD coating at distinct magnifications, **d** Histogram of the SEM image [25]

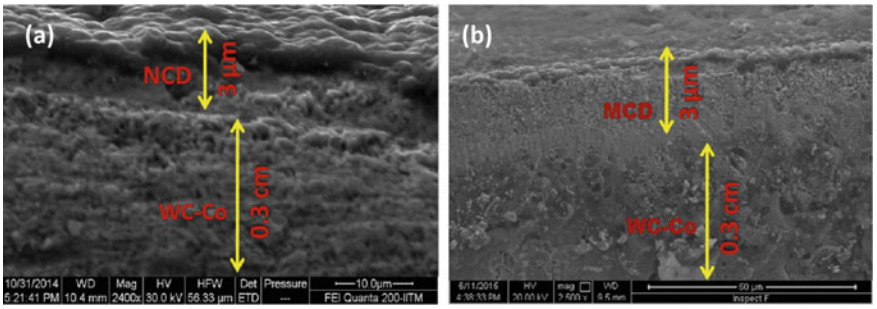

Fig. 8 Cross-sectional morphologies of **a** WC–Co/NCD and **b** WC–Co/MCD coating-substrate systems [26]

Provides much detailed and better topographical contrast. Here, the NCD and MCD coatings show different AFM phase images, as represented in Fig. 10a, b, correspondingly. During this AFM technique, similar areas of the MCD coatings and NCD coatings were scanned as in SEM technique and presented here. Therefore, Fig. 10a displays the 2D-AFM phase image of NCD coating at a scanning area of $2 \times 2\ \mu m^2$. Small grain sizes with cauliflower type of smooth structures were visualized on the NCD surface and thus possess good tribological properties. Also, details of the height of these features are denoted by a color scale on the AFM height image and listed here. Similarly, for MCD coating, same area was scanned by AFM

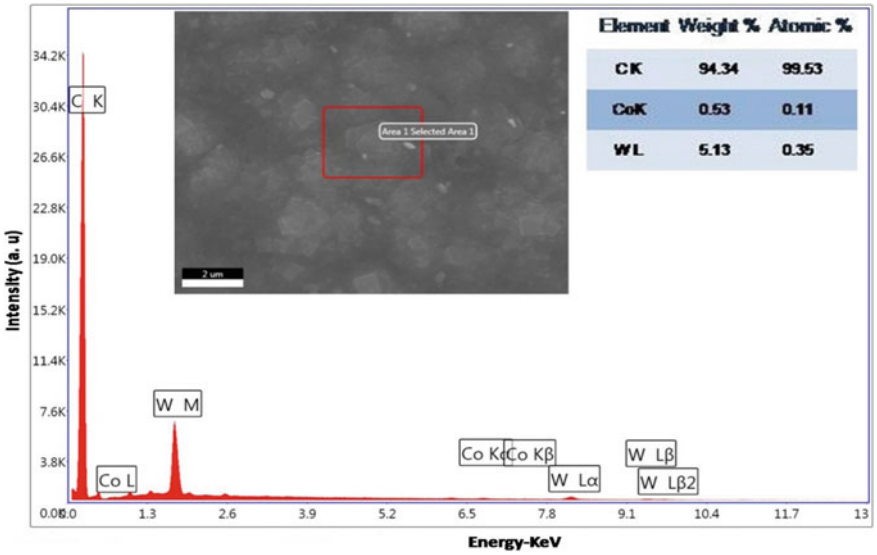

Fig. 9 Energy dispersive spectroscopy analysis (EDS) of NCD and MCD coating surfaces [26]

and represented here. Figure 10b displays the AFM phase image of MCD coating at scanning area of $2 \times 2\ \mu m^2$. Large grain sizes with faceted type of smooth structures were noticed on the surface of MCD, but the sharp features noticed on the MCD surface were unfavorable for them to be used in tribological applications [18].

3.4 Nano-Indentation and Hardness Measurement

Before Nano-indentation testing, the MCD and NCD coatings were polished by using a Tribometer and sliding for 2 h against Si_3N_4 pin. For these polished MCD and NCD coatings, Fig. 11a, b shows their load-displacement curves, respectively [26]. Thus, on each individual coating, four indentation tests were performed using Berkovich Nano-indenter. The average indentation depths for NCD coating and MCD coating were found to be ~79.75 nm and ~74.75 nm respectively and their excellent average hardness values were in the range of ~37–40 GPa and ~47–50 GPa, respectively. Also, the elastic modulus values of NCD coating and MCD coating were found to be ~1000 GPa and ~1100 GPa correspondingly, as calculated from the mathematical method by Oliver and Pharr [27].

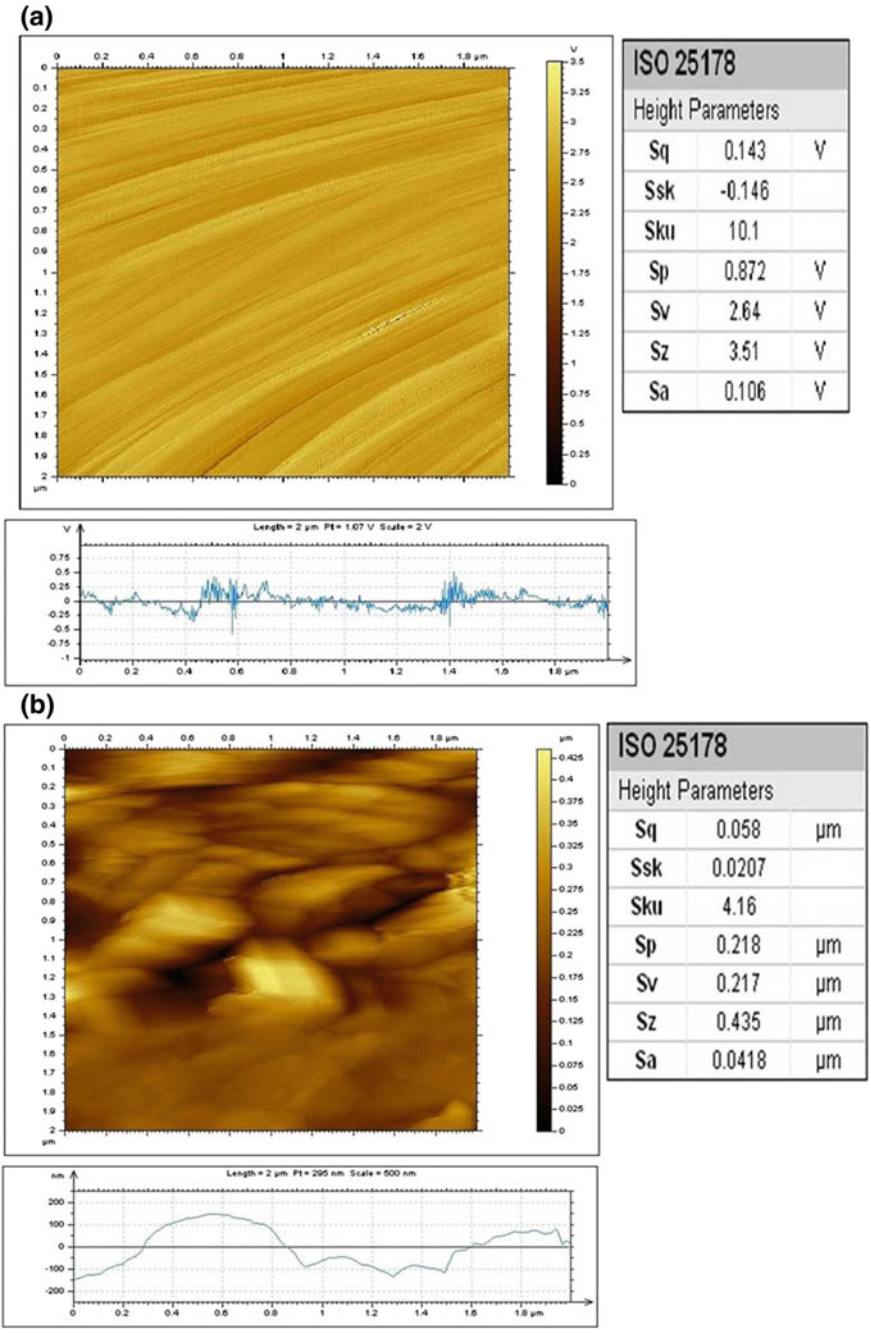

Fig. 10 AFM phase image ($2 \times 2\ \mu m^2$) with height details, **a** NCD coating, **b** MCD coating [18]

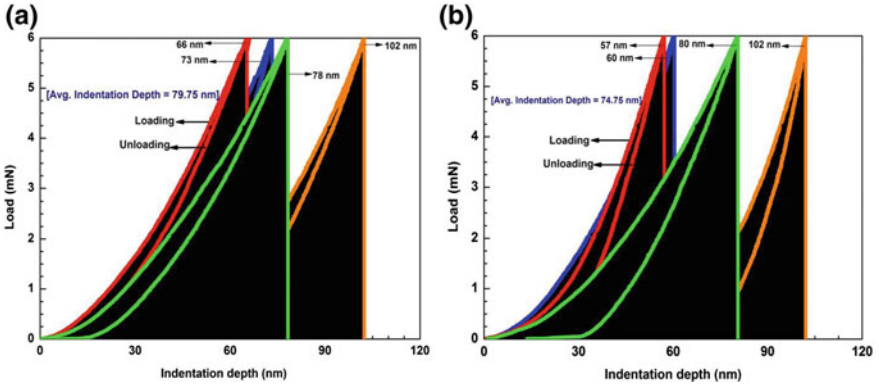

Fig. 11 Load-displacement curves equivalent to 4-indentations on **a** NCD and **b** MCD coatings [27] with kind permission from Cambridge University Press

4 Summary

I. The fabrication of crystalline and adhesive NCD and MCD coatings basically depends on the major controlling parameters (CH_4/H_2 ratio and pressure) in HFCVD chamber during initial pre-programmed recipe. Thus, synthetic diamond coatings deposited for 3 h. Enhancement of nucleation of NCD films was achieved at high methane concentration and low chamber pressure. Whereas, with low methane concentration and high chamber pressure enhanced the nucleation of MCD films. The increase in percentage of CH_4/H_2 ratio and decrease in chamber pressure, decreased the crystalline quality and grain size of the diamond coating.

II. Using HRSEM technique, the columnar structures of grains and faceted form of surface morphology were observed on the surface of MCD coating, whereas a cauliflower type of grain structure is generally seen on the surface of NCD coating.

III. Raman spectroscopy based study of synthetic diamond coatings confirmed the presence of trans-polyacetylene (TPA), and graphitic-carbon phases at the grain boundaries of the NCD coatings. The crystallinity of each diamond coating was confirmed using XRD method.

IV. The optimum diamond coating on the carbide substrate can be achieved by securing the optimum coating-thickness, grain-size of coating, and surface roughness of substrate before deposition. Moreover, increasing the thickness of diamond coating increases only load-bearing capacity of carbide material.

V. Hence, depositing smooth synthetic diamond coatings on carbide tools with optimum thickness, low friction coefficient, high hardness and good interfacial integrity will certainly be beneficial in many applications.

References

1. Erdemir, A., Fenske, G., Krauss, A., Gruen, D., McCauley, T., Csencsits, R.: Tribological properties of nanocrystalline diamond films. Surf. Coat. Technol. **120**, 565–572 (1999)
2. Sharma, N., Kumar, N., Dhara, S., Dash, S., Bahuguna, A., Kamruddin, M., et al.: Tribological properties of Ultrananocrystalline diamond film-effect of sliding counter bodies. Tribol. Int. **53**, 167–178 (2012)
3. Williams, O.A., Daenen, M., D'Haen, J., Haenen, K., Maes, J., Moshchalkov, V.V., Nesládek, M., Gruen, D.M.: Comparison of the growth and properties of ultrananocrystalline diamond and nanocrystalline diamond. Diam. Relat. Mater. **15**, 654–658 (2006)
4. Schwarzbach, D., Haubner, R., Lux, B.: Internal stresses in CVD diamond layers. Diam. Relat. Mater. **3**, 757–764 (1994)
5. Dumpala, R., Chandran, M., Kumar, N., Dash, S., Ramamoorthy, B., Ramachandra Rao, M.S.: Growth and characterization of integrated nano- and microcrystalline dual layer composite diamond coatings on WC–Co substrates. Int. J. Refract. Metals Hard Mater. **37**, 127–133 (2013)
6. Wiora, M., Brühne, K., Flöter, A., Gluche, P., Willey, T.M., Kucheyev, S.O., Van Buuren, A.W., Hamza, A.V., Biener, J., Fecht, H.J.: Grain size dependent mechanical properties of nanocrystalline diamond films grown by hot-filament CVD. Diam. Relat. Mater. **18**, 927–930 (2009)
7. Trava-Airoldi, V.J., Corat, E.J., Peña, A.F.V., Leite, N.F., Baranauskas, V., Salvadori, M.C.: Columnar CVD diamond growth structure on irregular surface substrates. Diam. Relat. Mater. **4**, 1255–1259 (1995)
8. Dauskardt, R.H., Lane, M., Ma, Q., Krishna, N.: Adhesion and debonding of multi-layer thin film structures. Eng. Fract. Mech. **61**, 141–162 (1998)
9. Salgueiredo, E., Almeida, F.A., Amaral, M., Neto, M.A., Oliveira, F.J., Silva, R.F.: A multilayer approach for enhancing the erosive wear resistance of CVD diamond coatings. Wear **297**, 1064–1073 (2013)
10. Bull, S.J., Berasetegui, E.G.: An overview of the potential of quantitative coating adhesion measurement by scratch testing. Tribol. Int. **39**, 99–114 (2006)
11. Buijnsters, J.G., Shankar, P., van Enckevort, W.J.P., Schermer, J.J., terMeulen, J.J.: Adhesion analysis of polycrystalline diamond films on molybdenum by means of scratch, indentation and sand abrasion testing. Thin Solid Films **474**, 186–196 (2005)
12. Ascarelli, P., Cappelli, E., Mattei, G., Pinzari, F., Martelli, S.: Relation between the HFCVD diamond growth rate, the line-width of Raman spectrum and the particle size. Diam. Relat. Mater. **4**, 464–468 (1995)
13. Woehrl, N., Hirte, T., Posth, O., Buck, V.: Investigation of the coefficient of thermal expansion in nanocrystalline diamond films. Diam. Relat. Mater. **18**, 224–228 (2009)
14. Qin, F., Chou, Y.K., Nolen, D., Thompson, R.G.: Coating thickness effects on diamond coated cutting tools. Surf. Coat. Technol. **204**, 1056–1060 (2009)
15. Saijo, K., Yagi, M., Shibuki, K., Takatsu, S.: Improvements in adhesive strength and cutting performance of diamond-coated tools. Surf. Coat. Technol. **47**, 646–653 (1991)
16. Sheikh-Ahmad, J., Chipalkati, P.: Effect of cutting edge geometry on thermal stresses and failure of diamond coated tools. Proc. Manufact. **30**, 1–12 (2015)
17. Najar, K.A., Sheikh, N.A., Dina, S., Shah, M.A.: Effect of CVD-diamond coatings on the tribological performance of cemented tungsten carbide substrates. J. Tribol. **9**, 1–17 (2016)
18. Najar, K.A., Sheikh, N.A., Shah, M.A.: Enhancement in tribological and mechanical properties of cemented tungsten carbide substrates using CVD-diamond coatings. Tribol. Ind. Faculty Eng. **39**(1), 20–30 (2017)
19. Dumpala, R., Kumar, N., Kumaran, C.R., Dash, S., Ramamoorthy, B., Ramachandra Rao, M.S.: Adhesion characteristics of nano- and micro-crystalline diamond coatings: Raman stress mapping of the scratch tracks. Diamond Relat. Mater. **44**, 71–77 (2014)
20. Prawer, S., Nemanich, R.J.: Raman spectroscopy of diamond and doped diamond. Philos. Trans. R. Soc. Lond. A **362,** 2537–2565 (2004)

21. Gunnars, J., Alahelisten, A.: Thermal stresses in diamond coatings and their influence on coating wear and failure. Surface Coat. Technol. **80**, 303–312 (1996)
22. Chandran, M., Kumaran, C.R., Gowthama, S., Shanmugam, P., Natarajan, R., Bhattacharya, S.S., Ramachandra Rao, M.S.: Chemical vapor deposition of diamond coatings on tungsten carbide (WC–Co) riveting inserts. Int. J. Refract. Metals Hard Mater. **37**, 117–120 (2013)
23. Kuzmany, H., Pfeiffer, R., Salk, N., Günther, B.: The mystery of the 1140 cm^{-1} Raman line in nanocrystalline diamond films. Carbon **42**, 911–917 (2004)
24. Ali, N., Neto, V.F., Mei, S., Cabral, G., Kousar, Y., Titus, E., Ogwu, A.A., Misra, D.S., Gracio, J.: Optimisation of the new time-modulated CVD process using the Taguchi method. Thin Solid Films **469–470**, 154–160 (2004)
25. Najar, K.A., Shah, M.A., Sheikh, N.A.: Integrity of CVD-Diamond coatings on cemented tungsten carbide substrate: mathematical analysis carried out for calculating the force of De-lamination and load bearing capacity of coating-substrate system. Elixir Nanotechnol. **90**, 37463–37467 (2016)
26. Najar, K.A., Sheikh, N.A., Butt, M.M., Shah, M. A.: Mathematical analysis carried out on the study of compatibility, De-lamination and load-bearing capacity of synthetic diamond coatings deposited on tungsten carbide composites. J. Nanotechnol. Mater. Sci. (OMMEGA Publishers), **6**(1), 10–16 (2019)
27. Oliver, W.C., Pharr, G.M.: Improved technique for determining hardness and elastic modulus using load and displacement sensing indentation experiments. J. Mater. Res. **7**, 1564–1583 (1992)

Index

K. Gupta (ed.), *Surface Engineering of Modern Materials*, Engineering Materials,
https://doi.org/10.1007/978-3-030-43232-4